

# **Final Report on the Design of the Mu2e Pion Production Target**

CJ Densham, JRJ Bennett, G Burton, TR Davenne, P Loveridge, J ODell

***STFC Rutherford Appleton Laboratory***

Harwell Science and Innovation Campus

Didcot, OX11 0QX, UK

18 January 2017

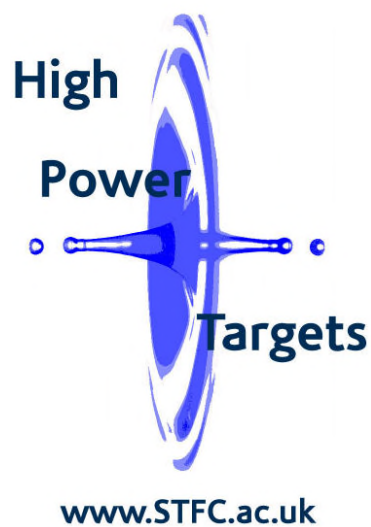


## Table of Contents

1	Introduction .....	3
2	Proposed Target Design.....	4
2.1.	Choice of Target Cooling Technology .....	4
2.2.	Tungsten as a Target Material .....	5
2.3.	Target layout overview.....	7
2.4.	Integrated target and hubs .....	8
2.5.	Spokes .....	13
2.6.	Spoke tensioners.....	21
2.7.	Mounting ring.....	29
2.8.	Catch Tray .....	33
2.9.	Mounting to the HRS .....	38
3	Failure Mechanisms Analysis for a Radiation Cooled Target.....	39
3.1.	Overview .....	39
3.2.	Cyclic Thermal Stresses .....	41
3.3.	Creep .....	44
3.4.	High Temperature Chemistry.....	51
3.5.	Target Material Loss by Evaporation.....	55
3.6.	Radiation Damage Effects.....	57
4	Technical Risk Mitigation Strategies .....	64
4.1.	Coatings.....	64
4.2.	Fins .....	66
4.3.	Target Geometry .....	71
4.4.	Forced Convection Cooling .....	73
4.5.	Beam Power .....	84
5	References .....	87

# 1 Introduction

This is the final report describing the work carried out by the UK STFC's Rutherford Appleton Laboratory under the 3<sup>rd</sup> contract with Fermilab on the Mu2e project, entitled 'Mu2e Production Target Development', to bring the target design to the CD-3 level.

Under previous contracts the High Power Targets Group at STFC-RAL has carried out and reported on a target feasibility study, conceptual design, design progression and testing activities [1] [2] [3] [4] [5] [6]. The present report is intended as an updated summary of these activities that can be used as a reference point as the project moves forward into a detail design and prototyping phase.

The report describes the preliminary design of the radiation cooled tungsten target and spoke support system, including a rationale for the concept and a description of risks. Due to the high thermal and radiation load, targets are expected to have a limited lifetime, with 1 year being the specified minimum lifetime required to limit the impact on the operation of the facility. An analysis of failure mechanisms for a radiation cooled target is used to inform the research program, and a Failure Mode and Effect Analysis is included for the specific design. The main body of the report describes the target design, thermal and mechanical analysis, prototyping and testing that has been carried out to date to optimise the proposed design, to verify the required manufacturing methods and to assess and mitigate the risks identified. The tungsten target rod is proposed to be supported by tungsten spokes tensioned by cantilever springs mounted from a titanium alloy outer ring. An outline concept is presented for a simple and easily dismountable spring system to support the target from the solenoid Heat and Radiation Shield (HRS) bore. A suggestion is made for an integral catcher tray to collect debris from a failed target. Various off-line high temperature experiments are described which were carried out to replicate as far as practicable the Mu2e operating conditions and to inform the detailed design. However, the test program was not able to address all issues of concern. The remaining issues are proposed to be studied in a future prototyping and test program as far as is practicable and within the available budget, but for example the radiation damage effects will only be evident after operation. A number of potential mitigating strategies are described to reduce operating temperatures and stresses.

## 2 Proposed Target Design

### 2.1. Choice of Target Cooling Technology

The Mu2e target has been designed with a goal to maximise the generation and capture of low-energy negative momentum pions produced by interaction with an 8 GeV, 7.7 kW primary proton beam. Heat generated by the proton beam/target interactions must be transferred away from the target via some cooling mechanism. In the baseline “radiation-cooled” target concept there is no active coolant and the target is allowed to heat up until it reaches an elevated equilibrium temperature where it is able to emit the deposited power by thermal radiation. The target is housed inside a water-cooled stainless steel vacuum vessel inside the bore of the Heat and Radiation Shield that ultimately absorbs the c. 600 W emitted by the hot tungsten target.

The radiation cooling technology option was chosen in favour of candidate liquid water or helium gas cooling schemes primarily in an effort to reduce project costs. A summary of these potential target cooling options is included in Table 1, where the “traffic-light” colour scheme represents the degree of technical difficulty perceived. That is, green being least technically difficult and red being most technically difficult.

The potential advantages of a radiation-cooled target include:

- i) No coolant plant is required. This altogether eliminates the costs associated with plant design, procurement, installation and maintenance.
- ii) No plant room is needed. This means the civil construction costs of that room may be eliminated.
- iii) Remote handling operations are simplified since there are no coolant pipe joints to disconnect or reconnect when replacing a target.
- iv) Eliminates the risk of potentially problematic coolant leaks.
- v) Simplifies the target design and minimises excess material for optimum pion production.

These potential benefits come at the cost of additional risk:

- i) Degraded material properties at elevated temperature may adversely affect the target lifetime under, for example, fatigue and/or creep.
- ii) Oxidation / chemical attack of hot tungsten surfaces by residual gasses in the target environment.
- iii) No local containment of the target means that any oxidation and evaporation of the target material will result in highly activated products being continuously deposited on all surfaces inside the secondary beamline, and in addition failed targets may disperse further contamination. This may pose a significant radiological hazard whenever it is necessary to open the beamline for maintenance/repair of components including replacing the target.
- iv) Progressive creep deformation of the target under self-weight / structural preload.
- v) Cannot monitor temperature rise or activation of coolant as a target condition monitoring diagnostic.
- vi) No relevant experience of high temperature target operation. Tungsten targets are generally operated with an active coolant at relatively low temperature. The

radiation damage mechanisms at elevated temperature may differ from those at low temperature.

- vii) Not upgradeable to higher beam power. Without an active coolant the target would overheat if the beam power was to be significantly raised (see section 4.5 of this report).

These additional technical risks have been addressed via the target test and development programme described in sections 3 and 4 of this report.

**Table 1, Summary of target cooling technology options**

	Radiation Cooled	Water Cooled	Helium Cooled
Material	Hot Tungsten	Cold Tantalum clad Tungsten or gold	Cold Tungsten
Physics Performance	No pion absorbing containment shell	c. 5% pion loss	c. 1% pion loss
Chemistry	High temperature /poor vacuum	Some chemistry (W/H <sub>2</sub> O)	No Chemistry
Operating Temperature	High	Low	Low
Ease of Remote Handling	No service connections	Water connections	Helium Connections
Plant Issues	No plant	Known technology	Complexity, cost
Diagnostics	Rely on muon yield and beam absorber diagnostics?	$\Delta T$ , activity	$\Delta T$ , activity
Contamination	No local containment shell	Water activation Issues with leaks	Low activation Low leak concerns
Experience/Data	Little radiation damage data on high temperature W	Data on Ta clad W	Data on pure W
Upgradeability	No	Yes	Yes

## 2.2. Tungsten as a Target Material

Tungsten has a high density and high atomic number, making it an excellent choice for efficient particle production. The use of tungsten as an accelerator target material is not new. Indeed it has been the spallation neutron target material of choice for many years including at the ISIS facility at RAL where tungsten targets are deployed at both the 1<sup>st</sup> and 2<sup>nd</sup> target stations (Figure 1). This means that there is a wealth of experience in operating tungsten targets up to high integrated dose levels, noting that these targets generally utilise some form of forced convection cooling and operate at relatively low temperature.



Figure 1, a tungsten ISIS target

Tungsten is the preferred material choice for the high temperature parts of the Mu2e target structure, namely the target rod, end connections (“hubs”), and tie rods (“spokes”). Tungsten has the highest melting temperature (3400°C), lowest vapour pressure and lowest thermal expansion coefficient of all the refractory metals. In the temperature range of interest for the Mu2e target tungsten retains a superior tensile strength compared to other candidate target materials, see for example Figure 2.

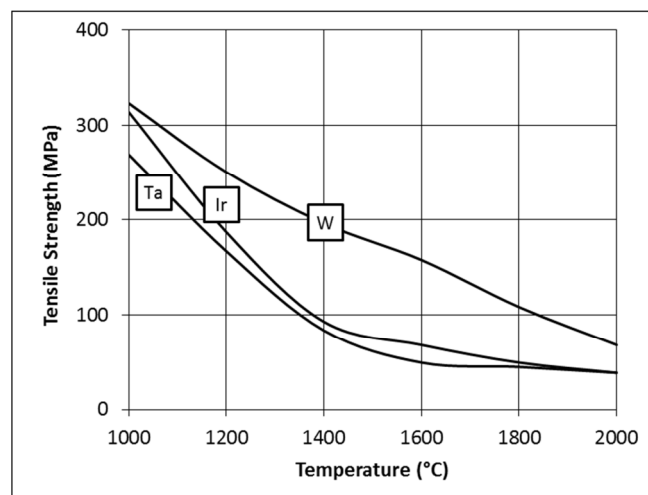
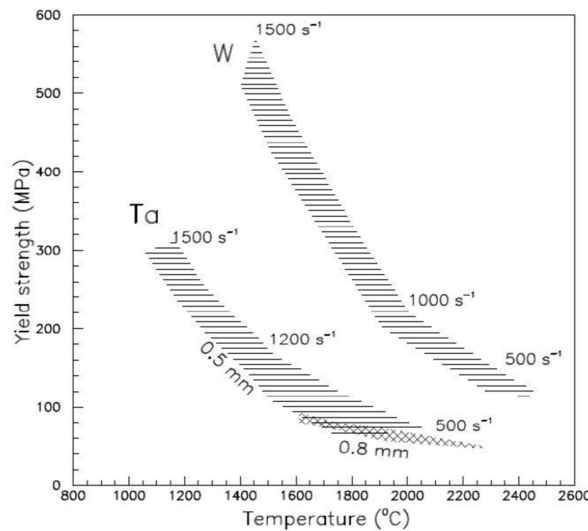


Figure 2, A comparative study on the elevated temperature tensile strength of some candidate target materials  
(Reproduced from BL Mordlake and CA Brookes, Platinum Metals Review, Vol. 4, pp. 94-99, 1960)

In a recent complementary programme at RAL [7] aiming to identify candidate high temperature target materials tungsten was shown to exhibit an excellent lifetime under repeated cyclic thermal loading at elevated temperature. See for example Figure 3.



**Figure 3, Lifetime thermal cycling results for tungsten and tantalum reproduced from studies by Bennett and Skoro**

### 2.3. Target layout overview

The physics requirements for the Mu2e facility specify a target similar in size and shape to a pencil, formed from a high atomic number material, mounted rigidly in the proton beam with minimal mounting material in close proximity to it. From these requirements, the concept of using a “bicycle wheel” arrangement was born. This arrangement allows the mounting components (“spokes”) of the target to work in tension, maximising their strength to mass ratio, resulting in a rigid, low mass support for the target.

Since this conceptual arrangement was approved, the target layout has been under continual development, incorporating knowledge gained from Finite Element Analysis work, prototyping and the test programme outlined in section 4 of this report. The design represented in Figure 4 is now at a preliminary stage, and forms the recommendation from RAL to Fermilab as a baseline target design to progress through detailing and prototyping.

The target is mounted by spring loaded “spokes” via an integrated hub. The spokes are tensioned by cantilever springs, which are mounted via a bracket to a “target ring”, and set the tension in the spokes as well as providing positional adjustment for the target. The target ring provides mounting features for the spoke tensioners, the interface features to the HRS, and the interface features to the End Of Arm Tooling (EOAT). The target ring provides the mounting for a debris catcher, and is protected from some of the radiated heat load from the target by a thin heat shield.

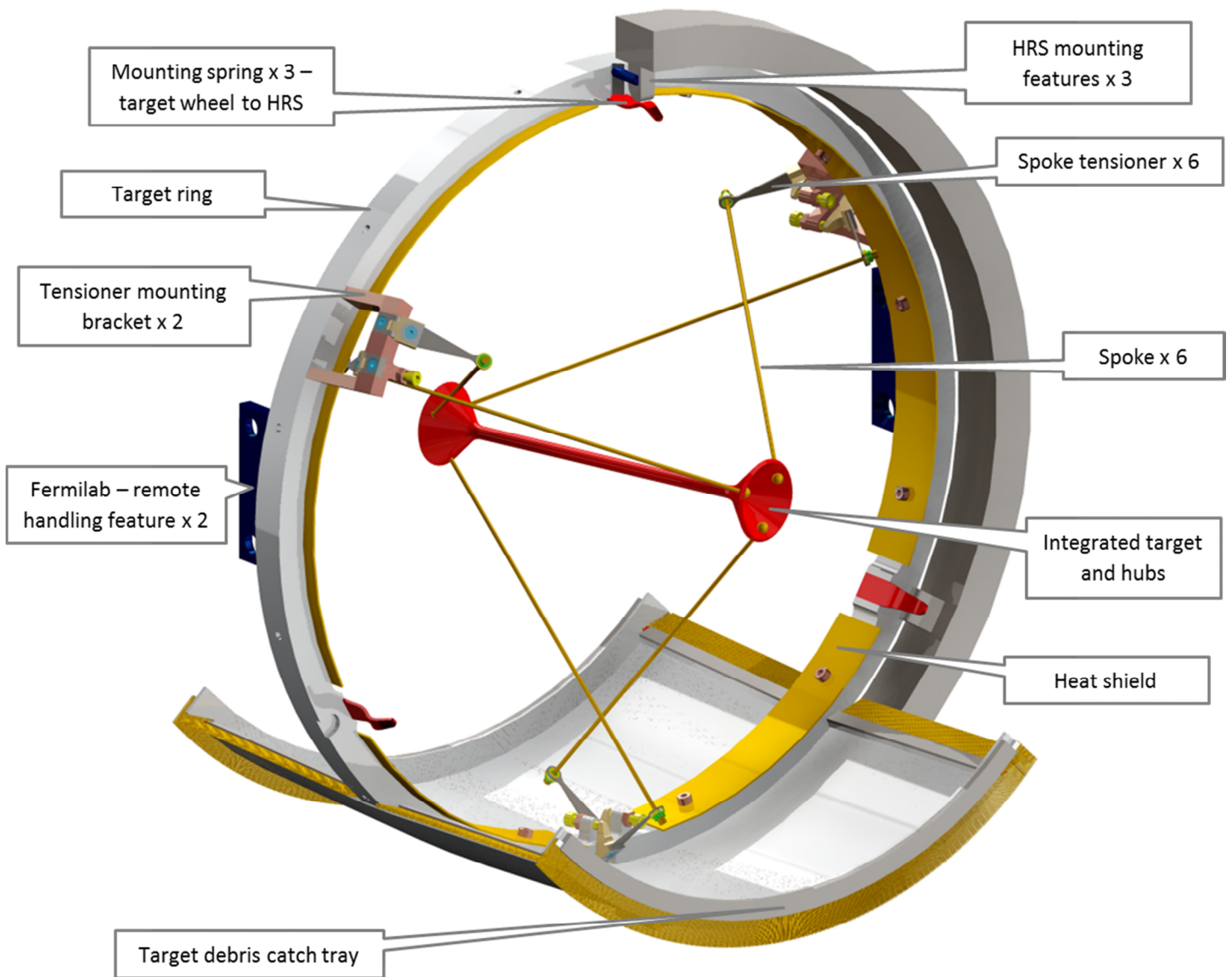
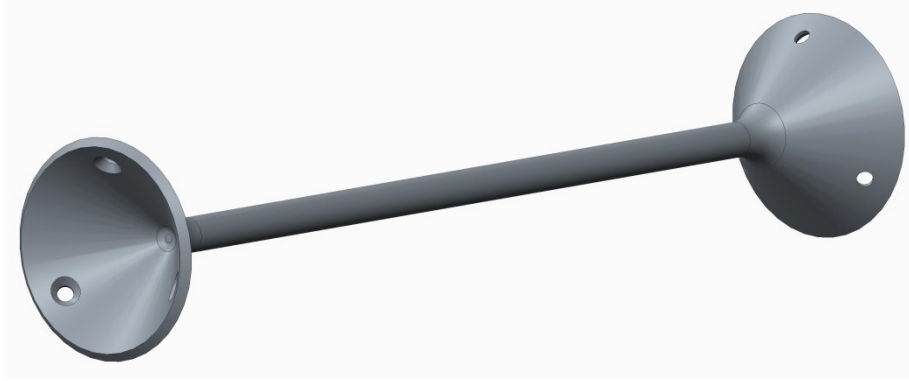


Figure 4, Mu2e target module - RAL preliminary design proposal

## 2.4. Integrated target and hubs

### 2.4.1 Overview

The tungsten target geometry is shown in Figure 5. It features a pencil-sized Tungsten rod with integrated cone-shaped hubs at either end. While early concepts presented the target and hubs as separate parts, here we propose a target with integrated hubs, machined from a single piece of material. Manufacturing the target and hubs in one piece make it more robust and less prone to the effects of high temperature oxidation. Sharp edges on features near the beam interaction have been replaced with bevels in order to reduce stress concentrations.



**Figure 5, Tungsten target with integrated hubs**

The primary function of the hub is to provide a mechanical interface between the target and the spokes that mount it in place. The hub also has a secondary role of providing some isolation of the spoke from the highest operating temperatures of the target.

The need to limit the maximum temperature of the support spokes has been weighed against the need to minimise the mass of material in the bore for low pion absorption. A peak spoke temperature of 1000°C is seen as a good compromise between lowering spoke temperature in order to mitigate the potential effects of creep elongation in the spokes, and reducing hub mass to improve physics performance. At this temperature we can see the following advantages:

- i) Operating the spokes below the re-crystallisation temperature of Tungsten reduces the rate of creep to a level where it is expected to be negligible.
- ii) The high temperature Oxidation rate of the spoke is temperature dependent, and therefore any reduction in spoke working temperature is an advantage.

#### ***2.4.2 Hub thickness***

The thickness of the hub is driven by the uncertainties surrounding the oxidation rate of the tungsten due to possible poor quality of vacuum. For this reason, a 2mm thickness for the hub is proposed here. The thickness is not driven by the stress in the hub at initial operating conditions, which is below 10MPa based on a pre-load of 20N on each spoke as shown in Figure 6.

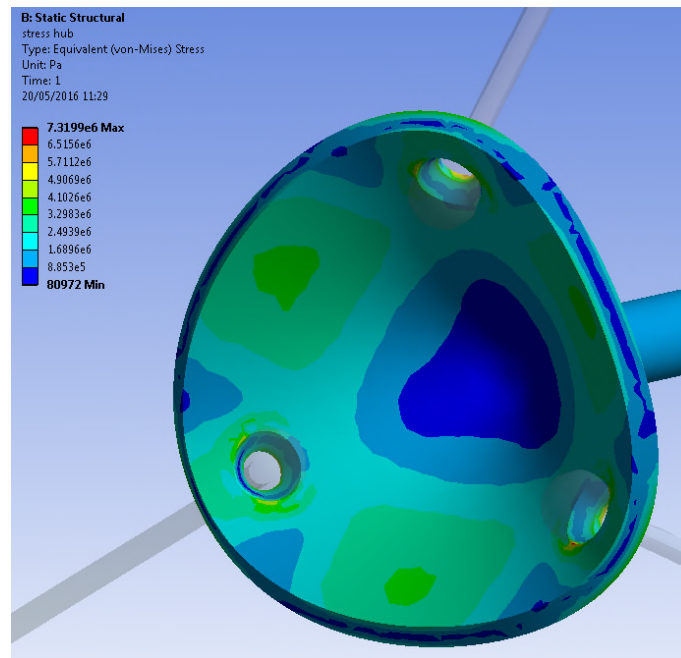


Figure 6, Von-Mises stress in 2mm hub with 20N pre-load in each spring - initial operating conditions

### 2.4.3 Hub length

The length of the hub is driven by the desire to reduce the temperature at the spoke attachment point to below 1000°C. The proximity of the spoke end features to the target/proton beam is also a factor here, and some optimisation with physics input is required. In order to reduce the temperature of the hub to below 1000°C at the spoke attachment location, and with the hub thickness outlined in the previous paragraph, then length of the hub required is approximately 25mm. This is illustrated along with other major dimensions in Figure 7.

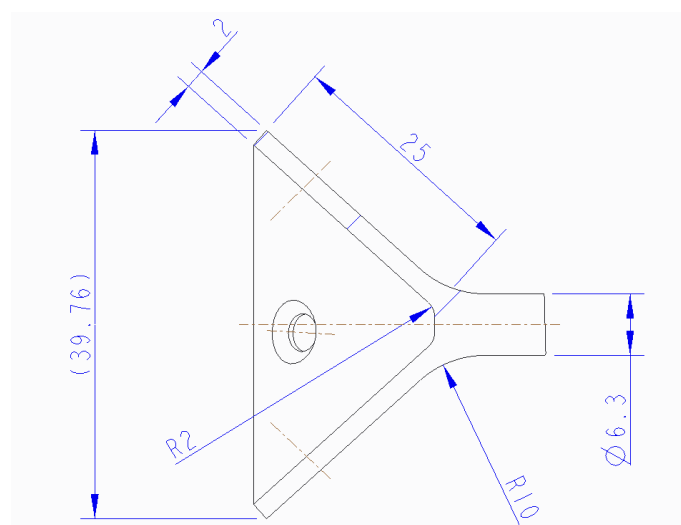


Figure 7, hub dimensions (mm)

### 2.4.4 Heat distribution in the hub

Figure 8 shows the heat profile in the hub at the hot end of the target (upstream relative to the incoming proton beam) based on the geometry shown in Figure 7. The temperature at the end of the target rod is about 1200°C, reducing to about 1000°C at the spoke attachment location. The rate of heat conduction from the target rod into the hub is limited by the cross sectional area of the hub. As the hub flares out, the heat path has a larger cross section, and conducts heat more easily resulting in a reduction in the temperature gradient as we move away from the target rod end. At the same time the rate of thermal radiative heat transfer from the hub reduces according to the fourth power of the absolute temperature (in Kelvin). These effects are partly offset by the increase in the hub surface area with increasing diameter of the cone, which allows more heat to be radiated.

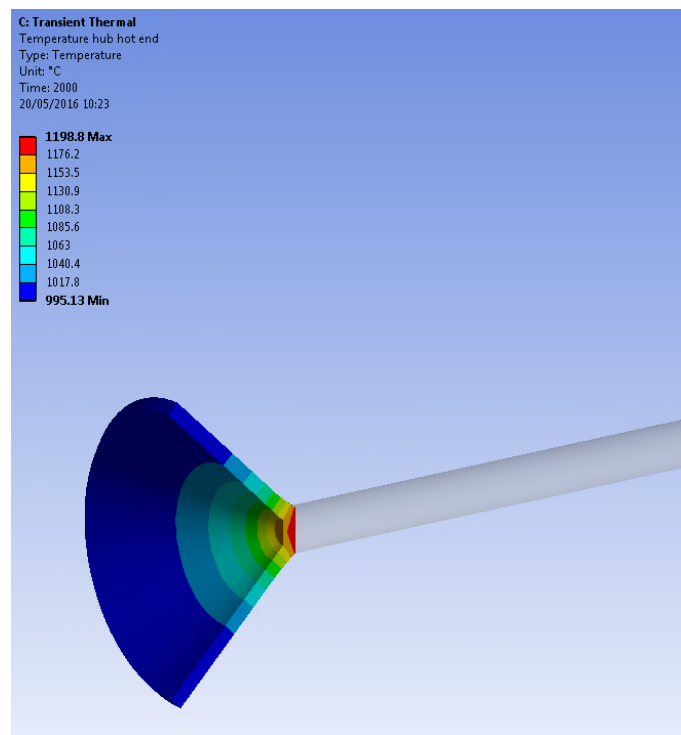


Figure 8, heat distribution in hub (hot end)

### 2.4.5 Hub geometry at spoke interface

Each hub has three spoke mounting holes, which are countersunk to provide a socket for the ball end of the spoke. The hole in the hub is large enough to allow the barrel end of the spoke to pass through it during assembly of the target wheel as shown in Figure 9, but with minimal clearance such that the ball cannot pass through the hub.

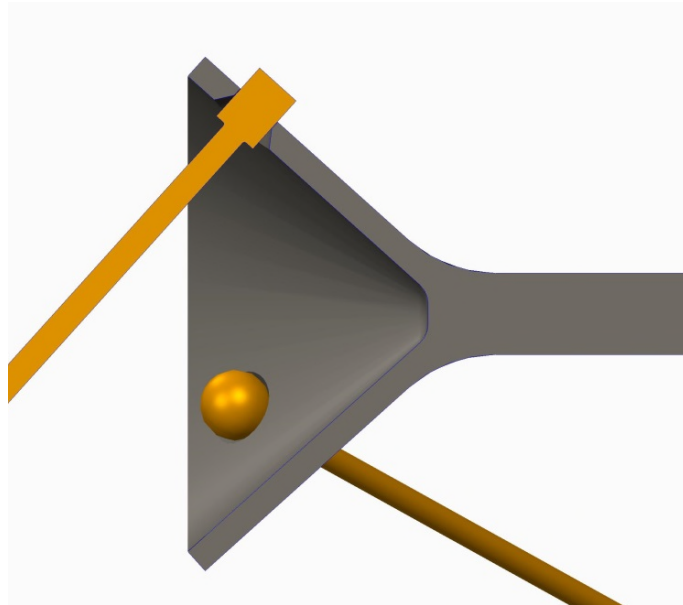


Figure 9, spoke barrel passing through hub

The ball location in the hub is shown in Figure 10. The larger the end features of the spoke are, the more resilient the interface is against loss of tungsten material due to oxidation. However, this should be weighed against the physics consideration relating to the size of the spoke end features.

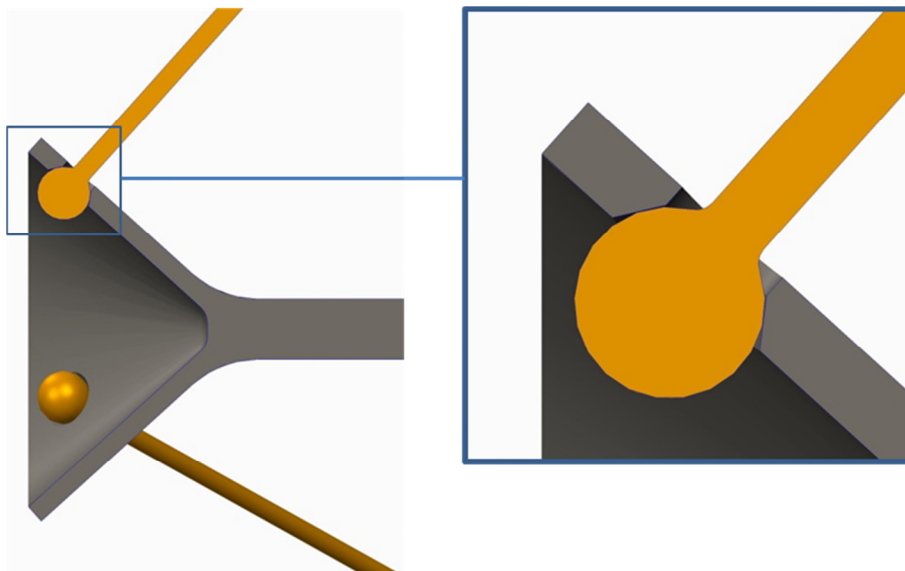


Figure 10, Hub interface to spoke

## 2.5. Spokes

### 2.5.1 Overview

The target spoke baseline is a 2mm tungsten rod, with a barrel feature at the “cold” end and a ball feature at the “hot” end. On assembly the spoke passes through the target hub barrel end first until the ball feature locates in a socket in the hub as shown in Figure 10. The barrel at the cold end of the spoke passes through a cantilever spring, and is tensioned via a spherical washer arrangement (Figure 11).

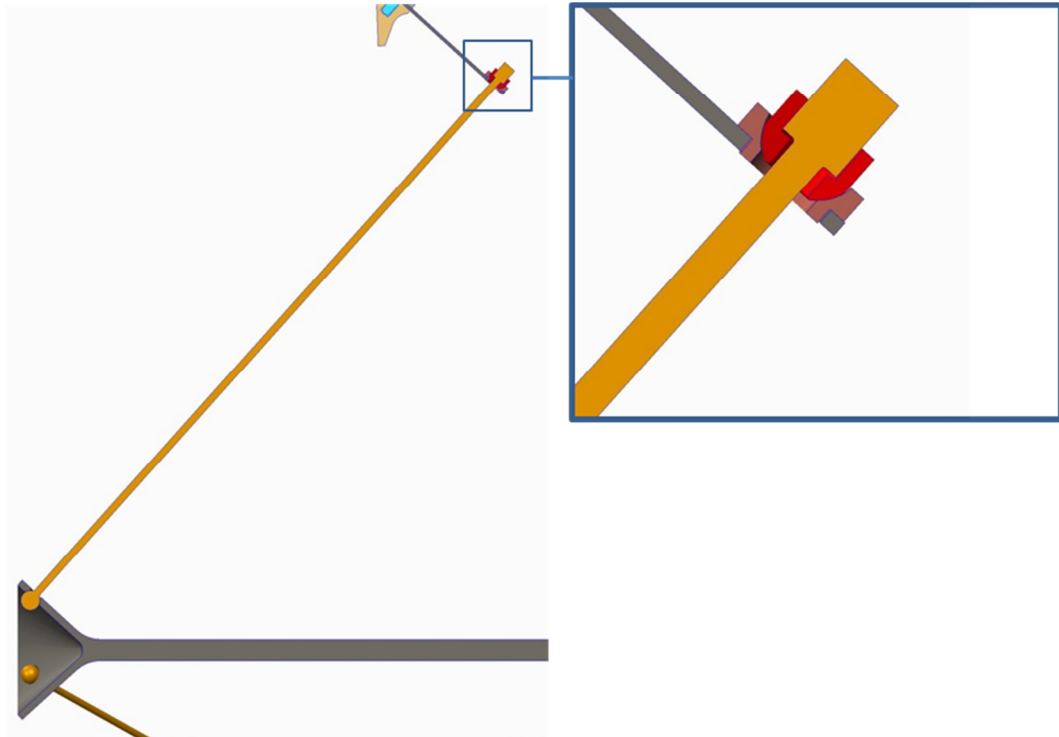


Figure 11, Barrel end of spoke

The proposed geometry of the spoke is shown in Figure 12, and was arrived at based on considerations for strength, manufacturability, physical robustness, impact on physics, thermal performance and sensitivity to the potential effects of oxidation.

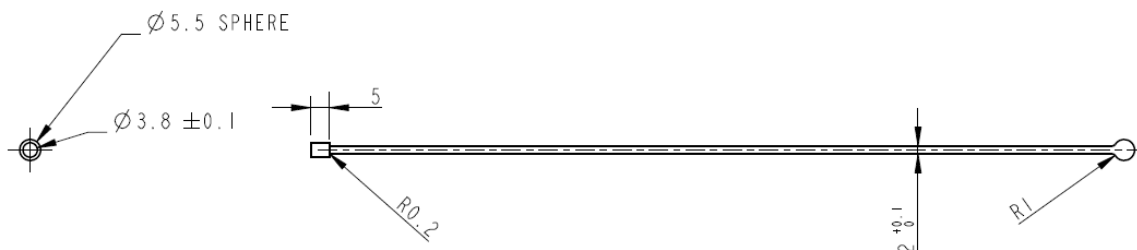


Figure 12, Spoke geometry

### 2.5.2 Spoke diameter

The drivers of the spoke diameter are summarised in Table 2 and described below.

Table 2, drivers of spoke diameter

Drivers towards a smaller spoke diameter:	Drivers towards a larger spoke diameter:
Minimal mounting material for optimum particle production efficiency	Reduced tensile / bending stress
Reduced thermal elongation of spoke	Improved resilience to oxidation

The physics requirements of the experiment drove the selection of a mounting arrangement with spokes in tension to minimise material. Pions produced in the target may be re-absorbed by surrounding material, and it is therefore important to optimise all the mounting components for mass reduction. It has been estimated that the difference between 1mm and 2mm diameter tungsten spokes is equivalent to a ~3% loss in relative stopped muons [8].

The spokes are designed to be long and thin enough that they provide an effective thermal conduction barrier between the target and support ring. Thermal elongation of the support spokes has been discussed previously [3] [9]. In summary the smaller the cross section of the spoke, the less heat it conducts away from the hot target, and the steeper the drop-off in temperature along the spoke as heat is radiated into the surrounding environment (Figure 13).

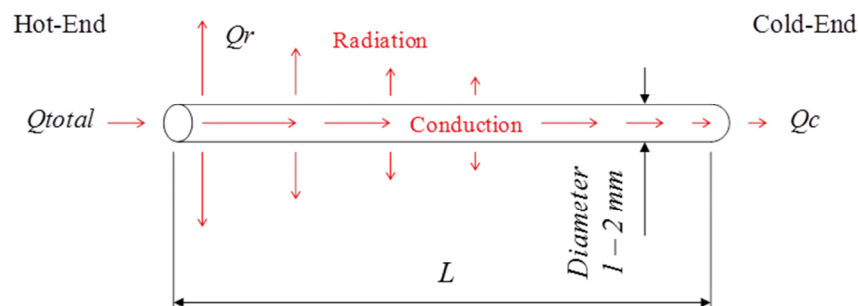


Figure 13, Heat transfer along a support spoke

A small spoke diameter is therefore attractive as it reduces thermal elongation, helping to keep the target stable in position during operation. A calculation of the temperature distribution along a typical target spoke is included in Figure 14, and the results are summarised in Table 3. The calculation represents a worst case for temperature and thermal elongation in the sense that no heat is assumed to be conducted out of the cold end of the spoke, i.e.  $Q_c=0$  in Figure 13. In reality some heat may be transferred from the spoke into the support ring via the sprung mounts, further reducing the temperature in the spoke. This effect is best quantified as part of the envisaged target prototype heating tests which may follow in the near future.

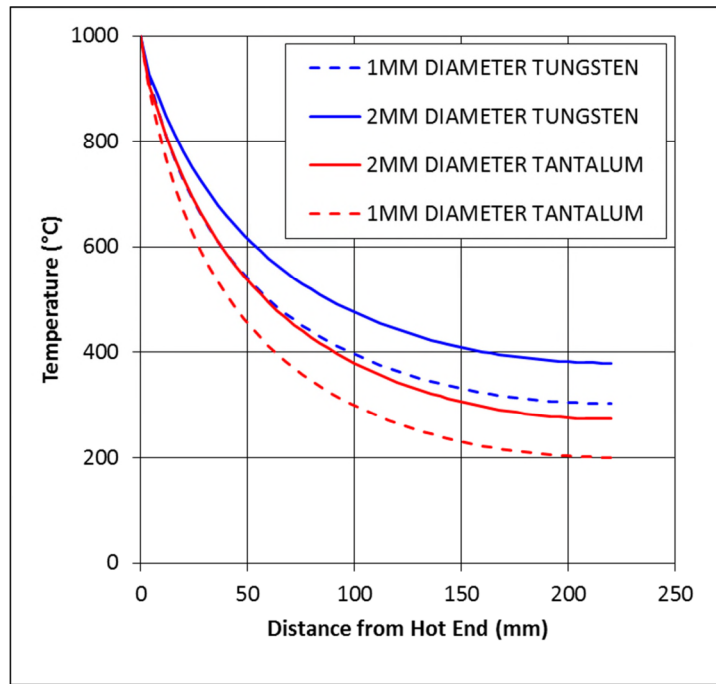


Figure 14, Temperature distribution along a spoke assuming no heat is conducted into the support ring

Table 3, Results summary relating to Figure 14 above

Diameter (mm)	1	2	1	2
Length (mm)	220	220	220	220
Material	W	W	Ta	Ta
T hot (°C)	1000	1000	1000	1000
T cold (°C)	303	379	201	274
$\Delta L$ (mm)	0.39	0.46	0.48	0.59

The spokes will be subject to both tensile and bending stresses during operation. A larger diameter spoke will be more robust against these effects. For example, increasing the spoke diameter by a factor of two decreases the tensile stress in the spoke applied by the tensioning spring by a factor of four. It also reduces the maximum bending stress in the spoke due to any applied bending moment by a factor of eight. Recall the tensile and bending stress in a solid cylinder of radius  $R$  subject to an applied tensile force  $F$  or bending moment  $M$ :

$$\sigma_{tension} = \frac{F}{A} = \frac{F}{\pi R^2}$$

$$\sigma_{bending} = \frac{My}{I} = \frac{4M}{\pi R^3}$$

Therefore a small increase in diameter can provide a large benefit in terms of physical robustness. The potential impact of creep in the target spokes is discussed in a previous report [5]. We expect that any reduction in the applied spoke tensile stress will be beneficial in this regard.

Increasing the spoke diameter reduces the sensitivity of the spoke to the potential effects of oxidation in a non-perfect vacuum (see section 3.4 of this report). For example, erosion of 100microns of material from the spoke surface on a 1mm diameter spoke would result in a reduction in cross-section area to 56% of its original value. For a 2mm diameter spoke the equivalent area reduction is only19%.

### 2.5.3 *Spoke prototyping*

We propose to manufacture the spokes out of Tungsten due to its excellent physical properties at high temperatures (see for example section 2.2 of this report). Tantalum has also been considered as an alternative to tungsten. It is inferior in terms of its strength and melting temperature, but it has the advantage of remaining ductile even at low temperature, and is viewed as a possible alternative to Tungsten should the prototyping of the target with Tungsten spokes raise any issues.

A number of successful spoke manufacturing trials have been performed [5]. After some initial manufacturing process trials proved successful, a full spoke was attempted in tungsten having a geometry chosen to represent the most difficult likely case for manufacture. This approach allows future design development of the spoke without concerns about whether the modifications make the spoke infeasible to manufacture. A spoke of 1mm in diameter, with a ball feature on one end and a barrel feature on the other was successfully manufactured by a wire Electro-discharge machining (EDM) turning process, and is shown in Figure 15.

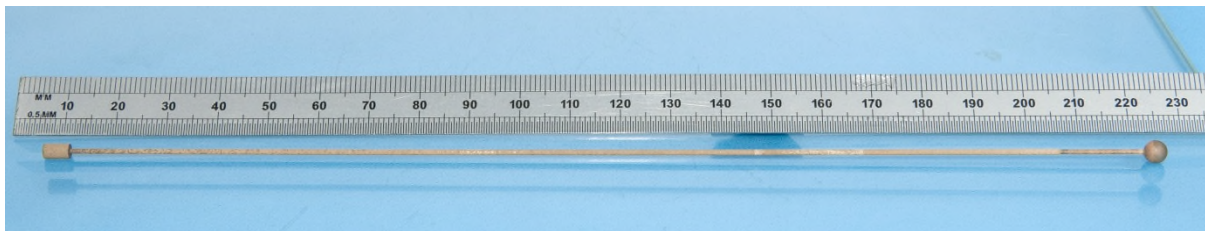


**Figure 15 - 1mm spoke from first full manufacturing trial**

Further manufacturing trials for more likely candidate spokes included a 2mm version of the tungsten spoke (Figure 16), and a 2mm tantalum alternative (Figure 17). They also included the manufacture of a 2mm Tungsten spoke of length 300mm (Figure 18) as a demonstrator of the achievable spoke length using the existing method and in-house facilities.



Figure 16 - 2mm diameter 220mm long tungsten spoke



Figure 17 - 2mm diameter 220mm long tantalum spoke

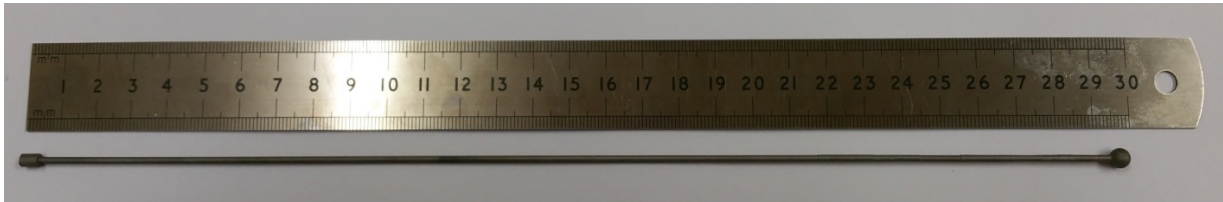


Figure 18 - The longest spoke thought to be achievable using the existing method and equipment is 300mm long

#### 2.5.3.1. *Surface treatment*

It was observed that post machining the spokes had a rough yellow/orange surface scale believed to originate from the brass EDM wire. This led to some erroneous surface geometry, and the spoke diameters tended to measure approximately 0.1mm oversize. A post-machining surface treatment is needed to remove the build-up of this brassy scale. Due to the brittle nature of the tungsten base material it was considered too risky to mechanically abrade/polish the spokes. Instead, a stress-free process of etching was developed.

A successful chemical etch procedure was derived through a programme of testing [5]. The proposal is for surface treatment of EDM machined spokes by immersion in 1:1 mix of 50% nitric acid and 50% Hydrochloric acid – a solution known as concentrated Aqua Regia. The effects of this surface treatment on a tungsten spoke are shown in Figure 19 for etching times of 1 and 30 minutes. No further weight loss was observed after 30 minutes etch time. From observation of the etching process on the tungsten spokes it is clear that the scale can be non-uniform in its thickness, distorting the appearance of the spoke geometry. After etching, it can be seen in Figure 19 that the geometry of the ball end is much improved.

Closer dimensional analysis of the post-etch spoke geometries revealed that the finish dimensions generally lie undersize. With this understanding it is believed that the process can be refined by compensating for the offset, such that the range is around the nominal value. Taking this into account we believe it may be feasible to achieve dimensional accuracy of something like nominal  $\pm 0.05$  mm.

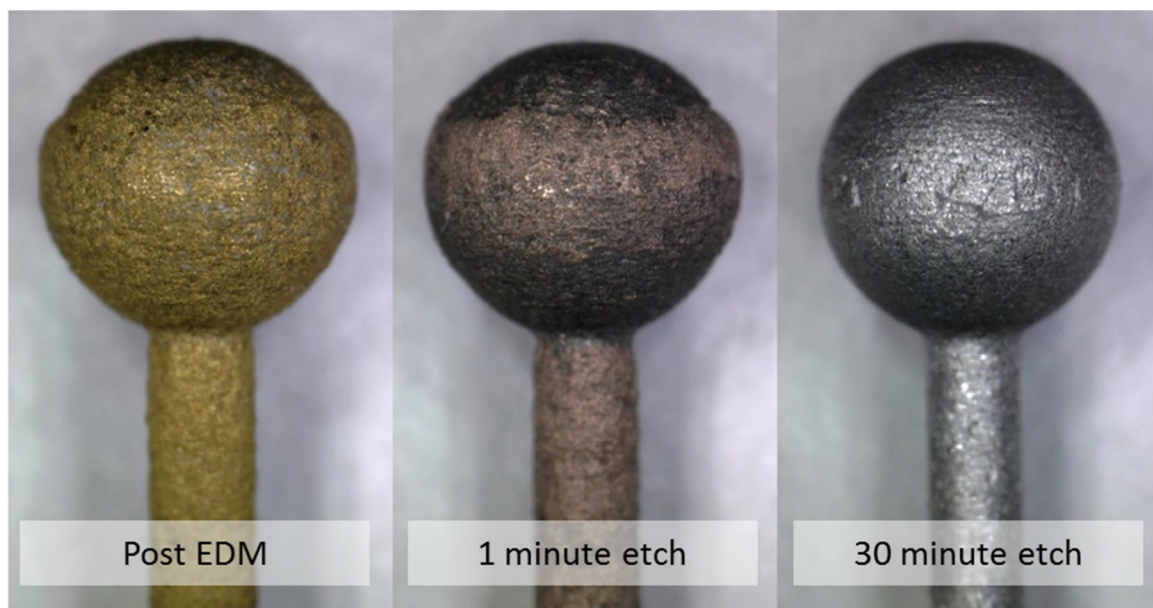


Figure 19, Etching trials for tungsten spoke

Prototype spokes were also produced in tantalum but these were somewhat more problematic. The post EDM etch of the prototype tantalum spokes was successful in as much as it removed the majority of the scale, revealing the smoother form of the tantalum beneath. However, a loose, black, sooty layer formed on the tantalum surface and did not disappear even after an extended period of time in the acid solution. Indeed, the tantalum spoke continues to lose mass indefinitely in the acid solution, indicating some ongoing reaction with the base material. In addition, some difficulties were encountered in achieving the underlying tantalum profile. If tantalum were to be chosen as the preferred option for the spoke there would be some further development work required to improve both the machining parameters and the post EDM surface treatment. The component form can almost certainly be improved by further adapting the EDM machining parameters, and from preliminary tests of removing the sooty layer on the Tantalum, it appears that a combination of etching and mechanical polishing could create a successful spoke. Note that since tantalum is a very ductile material there is less perceived risk in abrading/polishing post EDM.

Since in service the tungsten spokes are likely to be exposed to temperatures of up to 1000°C at the hot end, it was important to expose the test spoke to these kinds of conditions before performing tests on its strength. It was also thought that heating the spoke to 1000°C might remove the layer of scale on the surface since it appears to be made up of brass, which melts at 900 - 940°C. A 1mm diameter tungsten spoke was heated in a vacuum furnace to just above 1000°C Figure 20. As predicted, the brass scale was removed from the spoke, however, a dark coloured residue remained.

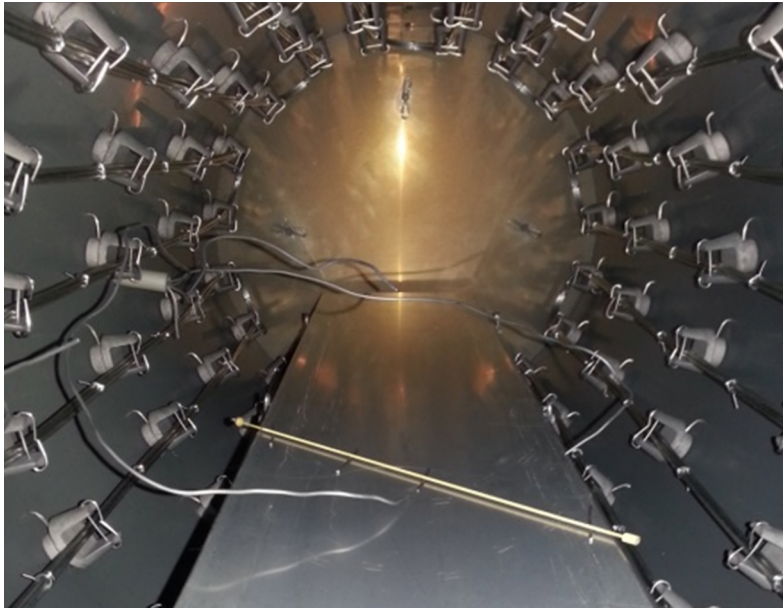


Figure 20, A 1mm diameter tungsten spoke placed inside the vacuum furnace prior to heating

A tensile testing rig was devised in order to pull test the 1mm spoke to failure. This rig was designed such that the spoke is constrained in a similar way to that in which it will be mounted in service (Figure 21). A photograph of the test setup is shown in Figure 22.

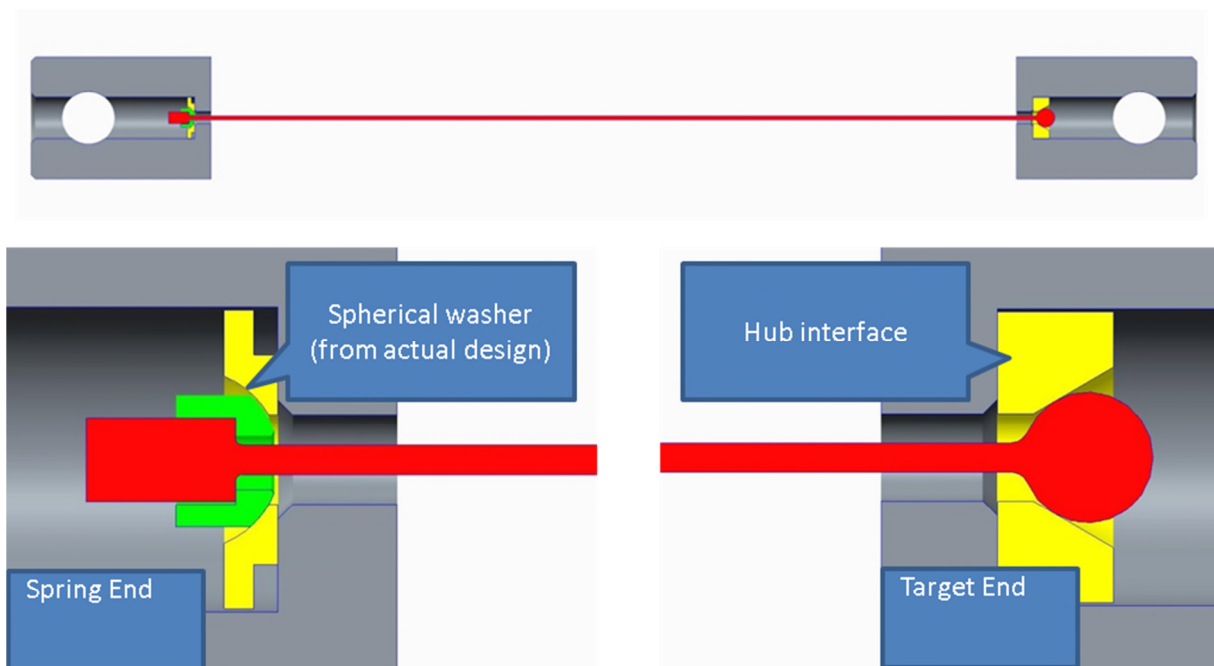
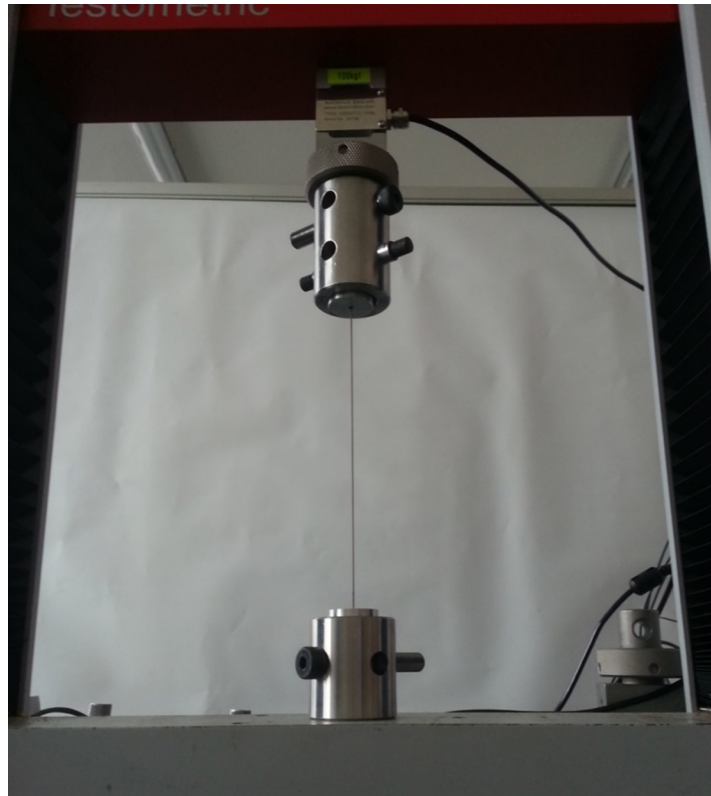


Figure 21, Spoke tensile test rig



**Figure 22, The spoke tensile test setup**

The tensile test was primarily intended to measure the UTS of the Tungsten spoke. Extensometers were not available for the test, and the stress/strain ratio is therefore that measured from the displacement of the cross-head, which does not take the strain in the machine elements into account, and should therefore be discounted. However, the shape of the stress/strain curve (Figure 23) does give an indication of the linear ramp and abrupt failure expected for a brittle material.

The spoke broke at a load of 392N, which corresponds to a tensile stress of 565MPa, approximately 40 times the expected working stress of the spoke. The failure occurred at the transition from the long 1mm diameter section to the larger end feature (Figure 24).

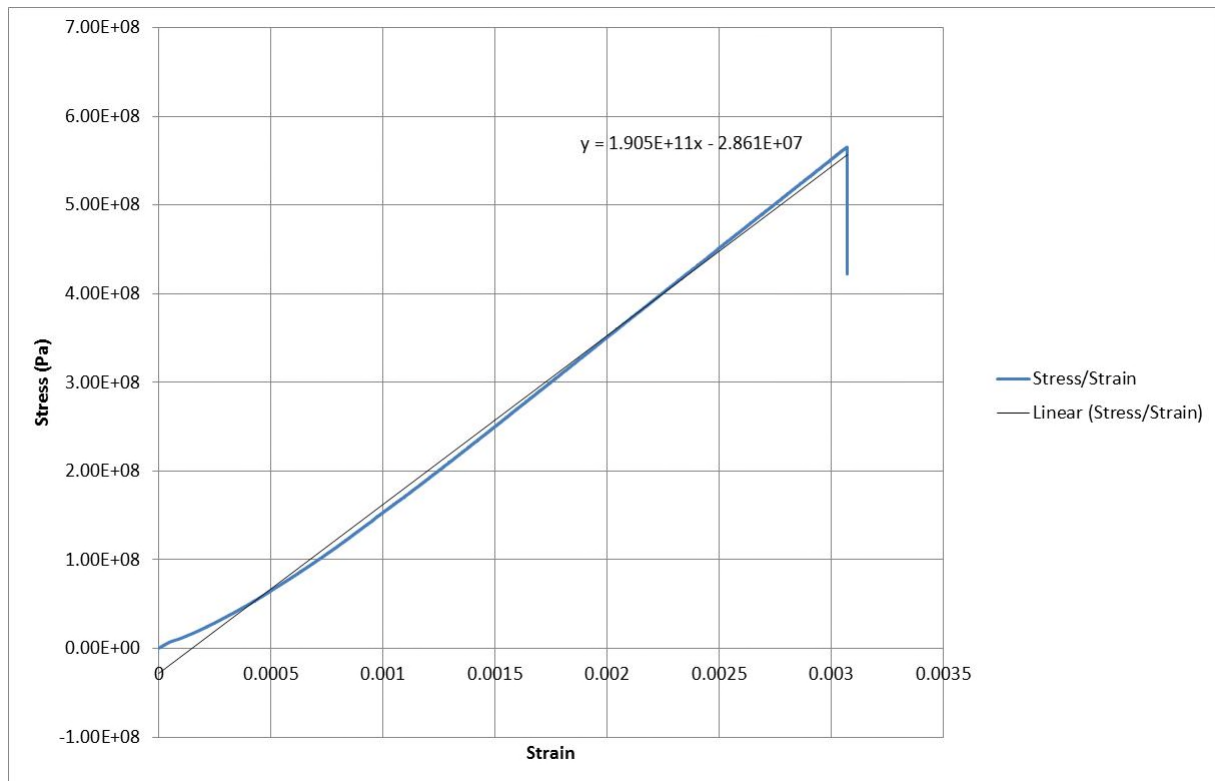


Figure 23, Stress/strain curve for the tensile test



Figure 24, The spoke failure

## 2.6. Spoke tensioners

In the “bicycle wheel” target support structure spoke tensioners are used to set the tension in the spokes as well as to provide positional adjustment for the target. Since the spoke tensioning design that was described in the previous report [5] there has been some optimisation work done on various aspects of the tensioner. This started with an analysis of the strengths and weaknesses of the cantilever design pictured in Figure 25.



**Figure 25, Early prototype of cantilever spring-type spoke tensioner**

The advantages of the cantilever spring-type tensioner are:

- i) Entirely independent of sliding mechanisms and spring will continue to tension spoke even after any or all parts of the mechanism has seized up
- ii) Simple system with very little to go wrong
- iii) Relatively small envelope – low Pion interaction
- iv) Spring easy to fine tune by modification to the geometry.
- v) Spring rate and elastic limit easy to predict from FEA

This mechanism also has some disadvantages which can be described as follows:

- i) Relative angle between cantilever spring and spoke changes as spring load changes, making it reliant on spherical washer during adjustment and alignment to avoid bending the spoke
- ii) Spring compression range is limited by spring length, meaning spring length may need to be increased, which could have negative impact on pion interaction

Further development work on the cantilever spring-type tensioner initially focussed on the spring itself. The aim of this work was to address the issue of spring range, without a significant increase in material mass. The bending moment on a cantilever increases toward the root, and since the initial concept spring had a constant cross section the bending stress was concentrated at the root of the blade. This stress at the root of the blade becomes the limiting factor on the blade range, with yielding seen here during early blade testing. After some optimisation, the geometry of the spring was developed from parallel to tapered as shown in Figure 26.

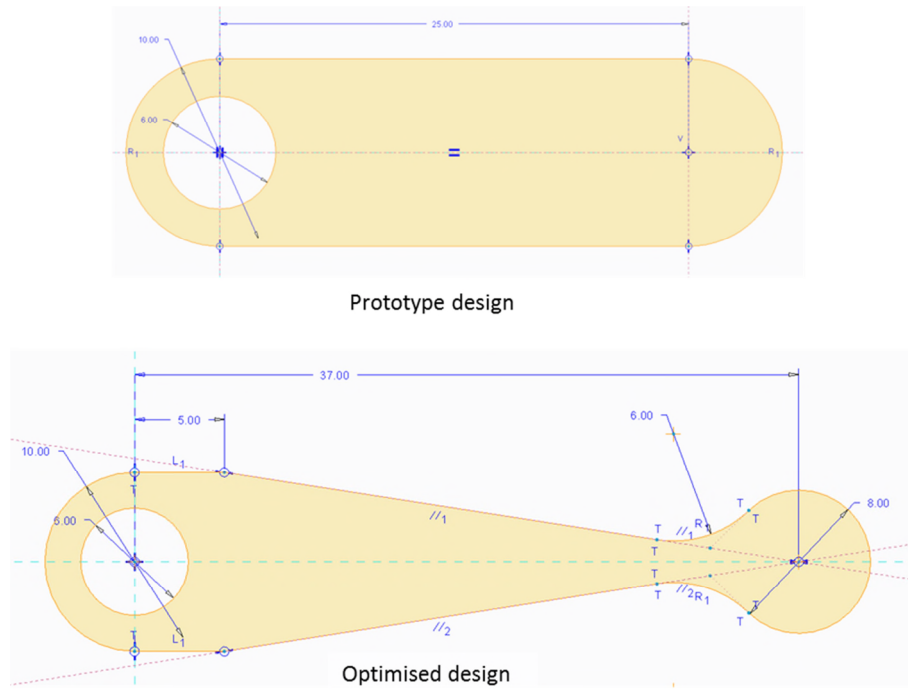


Figure 26, comparison between original prototype spring and optimised spring geometry

The three main changes made to the blade were as follows:

- i) Spring tapered in order to distribute stress more evenly, increasing total deflection for a given load/length
- ii) Spring lengthened to increase deflection whilst reducing change of relative angle between the spring and the spoke
- iii) Spring thickness increased in order to maintain a similar spring rate for the elongated spring

The stress distributions of the initial prototype and the optimised design are shown in Figure 27. The 2<sup>nd</sup> iteration cantilever spring-type spoke tensioner is shown in Figure 28.

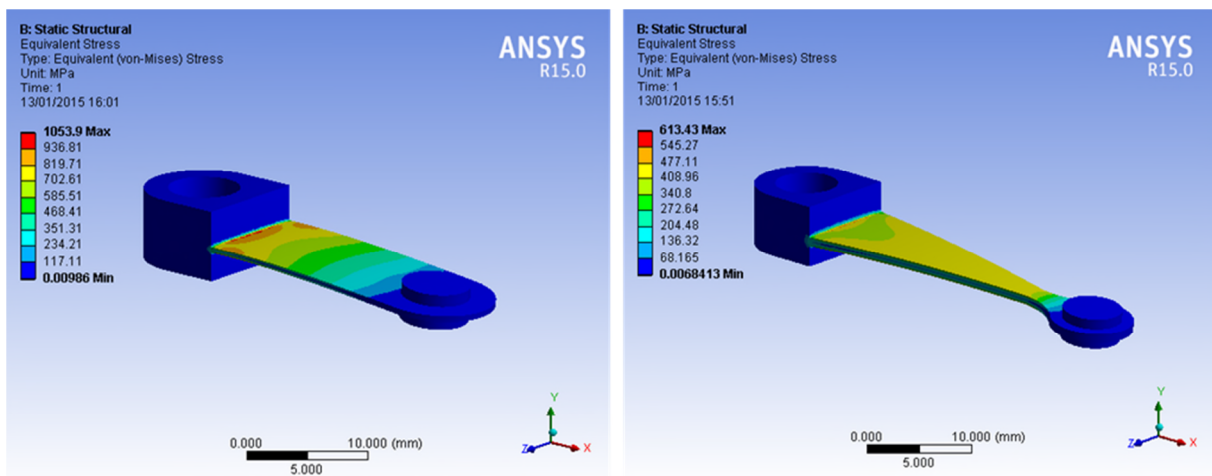


Figure 27, Stress distribution comparison between initial prototype cantilever spring (left) and optimised version (right)

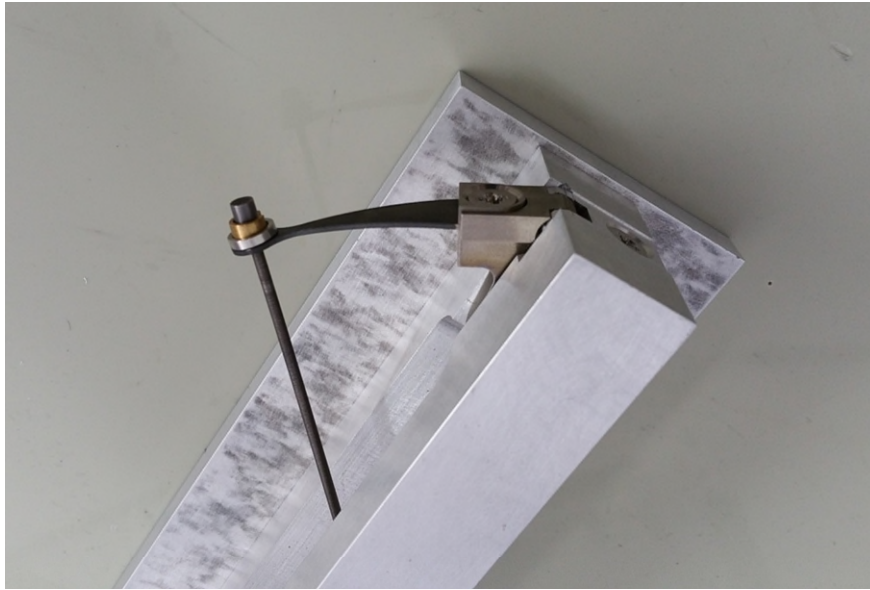


Figure 28, 2nd iteration cantilever spring-type spoke tensioner

The characteristics for the proposed spring are as follows:

- Spring material – Inconel 718
- Yield strength = 1.2GPa
- Spring thickness = 0.9mm
- Spring rate =  $\sim 7\text{N/mm}$
- Deflection in spring under 1.8kg load =  $\sim 2.5\text{mm}$
- Stress in spring at 2.5mm deflection =  $\sim 450\text{MPa}$
- Estimated spring range =  $\sim 6\text{mm}$

Inconel 718 has very high strength, which it maintains at elevated temperatures as can be seen in Figure 30, making it an excellent candidate for the spoke tensioning springs. In addition to this, ISIS spallation source have experience of Inconel 718 performing successfully as beam widows under extreme irradiation. A batch of 10 inconel springs were successfully produced by laser cutting from stock sheet. The springs were subjected to a precipitation hardening heat treatment in air post machining to improve their tensile strength. Post heat treatment the springs appeared black, presumably due to oxidation occurring during the heat treatment cycle. For the next stage of prototyping we plan to precipitation harden the springs in an inert atmosphere to eliminate the build up of any oxide scale.



Figure 29, 2nd iteration inconel 718 cantilever springs, as machined (left) and precipitation hardened in air (right)

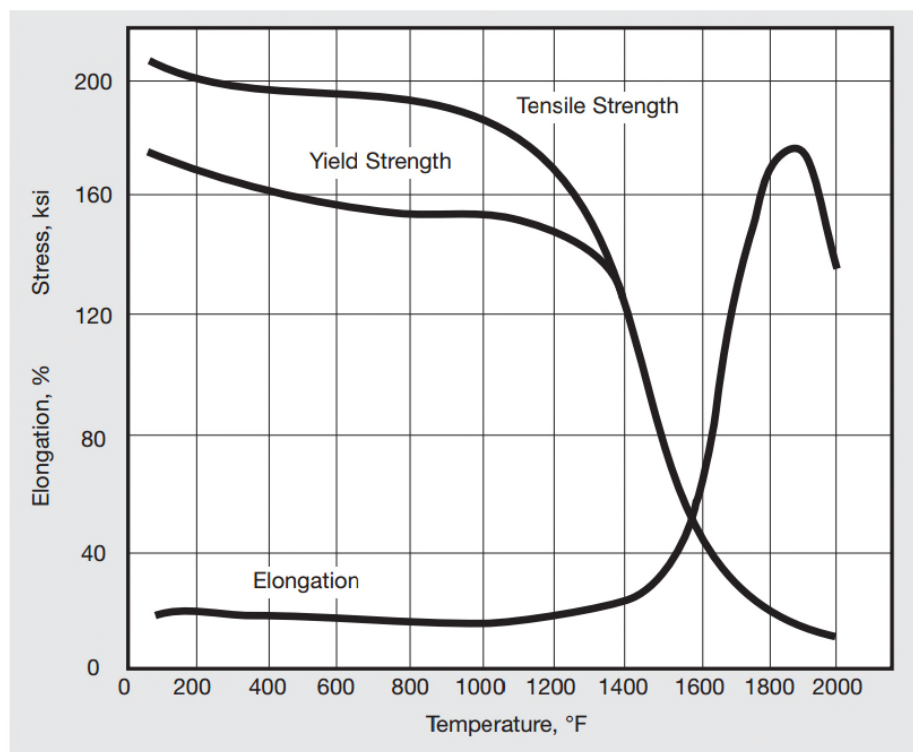


Figure 30 - High-temperature properties of 1/2-in diameter hot-rolled, annealed (1800°F/1 hr) and aged (1325°F/8 hr, F.C. to 1150°F, hold at 1150°F for total aging time of 18 hours) bar.

A compression spring-type tensioner was also considered, with a design produced and a prototype built. This design is shown in Figure 31. Design considerations for the compression spring version include the removal of sliding location features that could seize up during operation, and a thumb screw and push plate to allow the spoke to be tensioned without the risk of applying a torque to the spoke. Some advantages and observations are outlined below:

- i) Adjustment mechanism works as intended, and is reasonably easy to use.
- ii) Spring properties can be easily altered without impacting on the envelope of the tensioner
- iii) Change in relative angle between spoke and mount is minimal, making it less reliant on spherical washer

There are also some disadvantages to this approach:

- i) Adjustment is less well isolated from the spoke than in the cantilever design.
- ii) Mechanism is bulkier than it's cantilever style counterpart
- iii) Spoke bending is not eliminated due to lack of lateral stiffness in the compression spring causing it to flex
- iv) Spoke location is poor due to lack of lateral stiffness in spring. A more laterally stiff spring, or some extra support is required
- v) Limited bore size of mount over the inserted length of the spoke makes maintaining clearance between spoke and bore sensitive to the relative angle between mount and spoke. Since the individual spokes make different angles with the bore of the solenoid, several unique tensioning mechanism mount variations or adapters are required

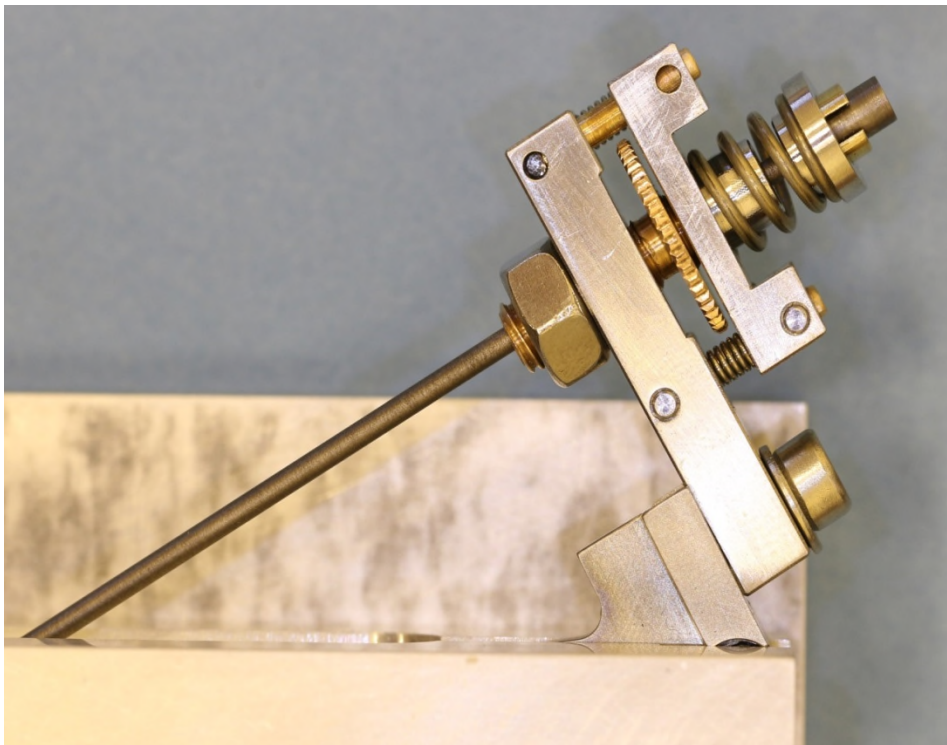


**Figure 31, Early prototype of compression spring-type spoke tensioner**

Following this 1<sup>st</sup> iteration the compression spring concept was developed further with a view to addressing some of the concerns that the initial prototype raised. This developed version which is shown in Figure 32 has three main updates from the previous version:

- i) The addition of a support tube to stop the compression spring deflecting laterally, making the spoke better constrained.

- ii) The addition of a deflection scale on the side of the support tube.
- iii) Rounding off of the interface between the spring and the spoke to allow it to rotate in the support tube bore without seizing up.



**Figure 32, 2<sup>nd</sup> iteration of prototype compression spring-type spoke tensioner**

Whilst this development improves the repeatability and stability of the spoke attachment at the ring interface, the modified design is more bulky, and it raises the risk of the mechanism seizing up so that the tension on the spoke cannot be guaranteed.

A question regarding possible additional forces placed on the spoke by the adjustment mechanism arises from the fact that the relative angle between the spoke and the cantilever spring change as the spoke is tensioned and the spring bends during initial setup. It has been suggested that this could result in a bending moment placed on the spoke. This effect is difficult to quantify since the majority of the differential rotation is absorbed by a spherical washer arrangement at the spoke/spring interface and the size of the effect depends heavily on the friction between the two spherical surfaces. A jig was devised as shown in Figure 33 with the purpose of simulating the target mounting ring, and the target/spoke interface. The jig is adjustable, allowing the spoke length/angle to be adjusted. The spoke tensioning mechanism is mounted to the jig, and the spoke itself is mounted between the Target/spoke interface and the cantilever spring part of the spoke tensioner.

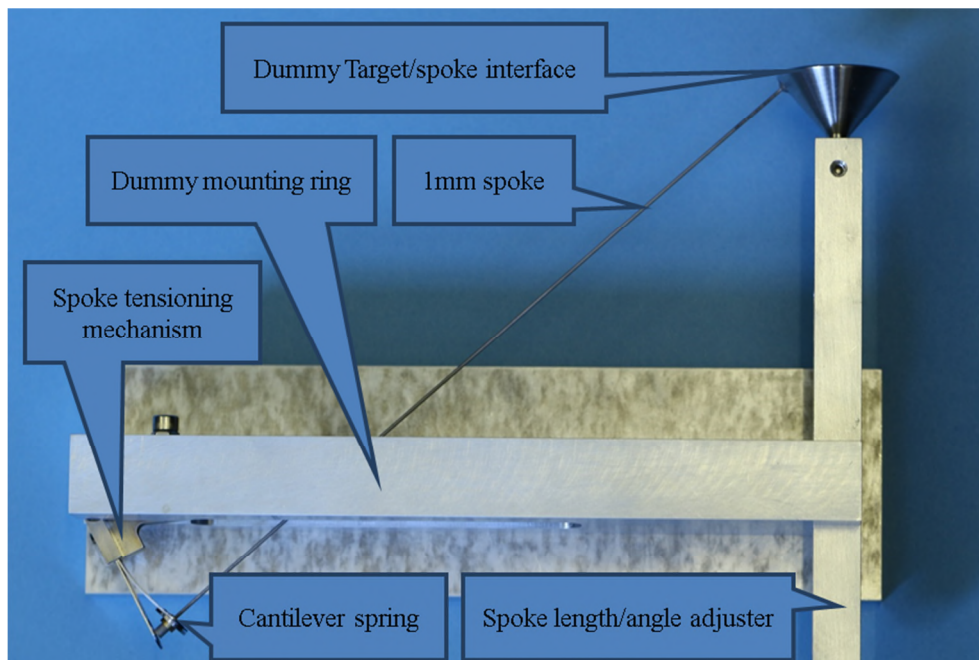


**Figure 33, Spoke tensioning jig**

A tungsten spoke was set up in the jig as shown in Figure 34 and repeatedly adjusted through a spring deflection range from 0mm to 6.8mm, resulting in a range of linear force on the spoke of 0 – 50N, which is approximately five times greater than the force expected on the spoke during its working life. The spoke survived the numerous tensioning and angle change operations performed on it, and on removal from the jig after testing, it showed no signs of damage.

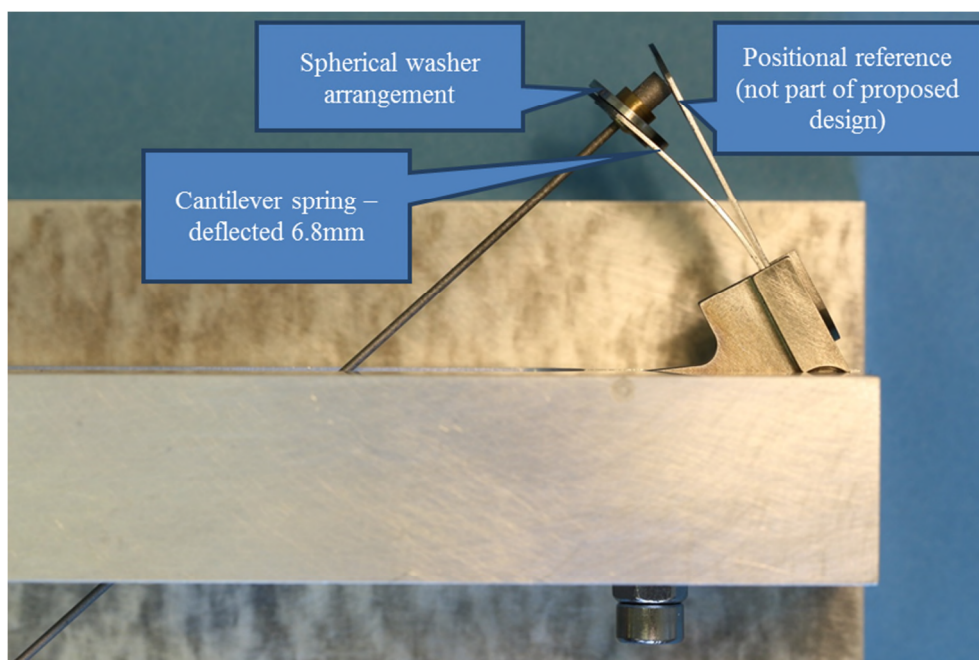


**Figure 34, Spoke under test**

Following the development of both the cantilever and compression spring concepts through two iterations of prototyping we prefer and recommend the cantilever style design for implementation going forward. For direct comparison, both versions are shown in Figure 35.

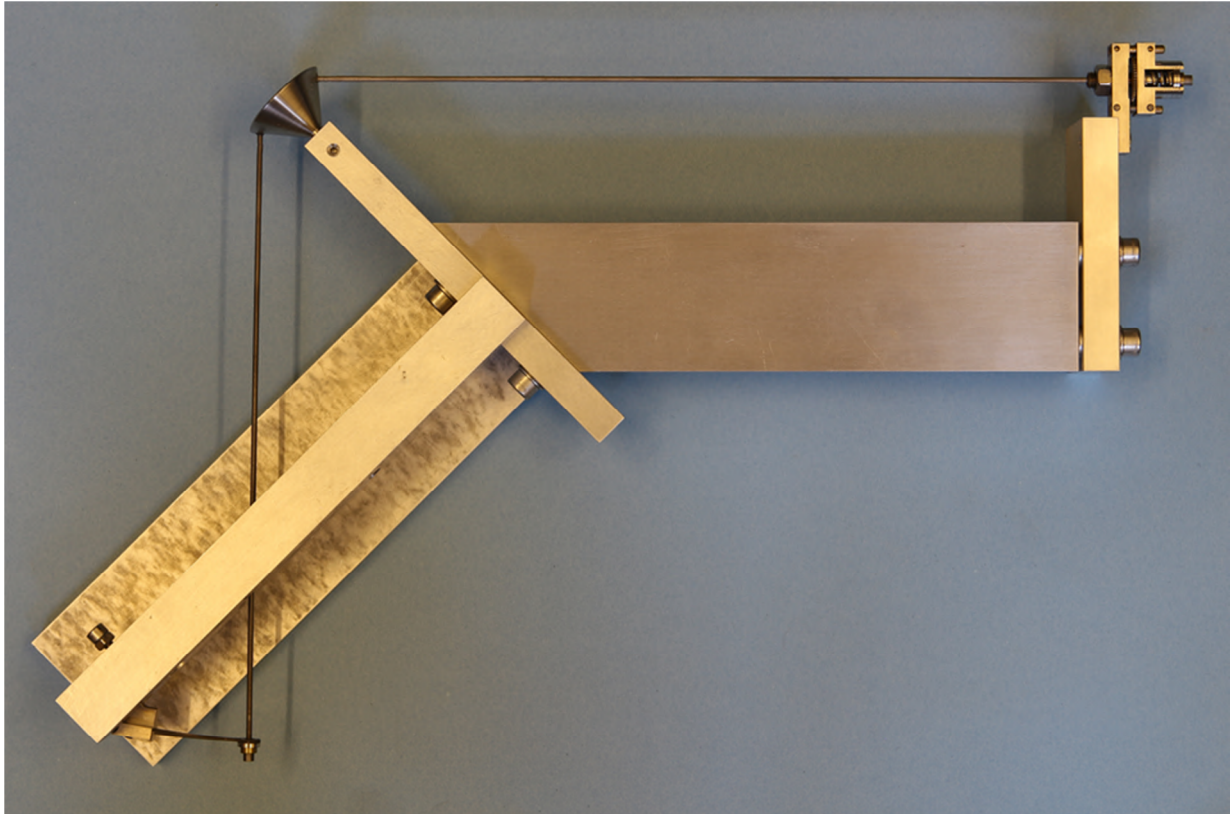


Figure 35, 2<sup>nd</sup> iteration cantelever spring type tensioner (bottom-left) and 2<sup>nd</sup> iteration compression spring-type tensioner (top-right) mounted on the test jig

## 2.7. Mounting ring

### 2.7.1 Mount ring overview

The target mounting ring is designed to be stiff and robust, making it a good base on which to build a modular target. The main roles of the mounting ring are as follows:

- i) To provide mounting locations for the spoke tensioners.
- ii) To provide mounting locations for features that interface to a remote handling tool.
- iii) To provide an interface for mounting the target structure to the bore of the target vacuum vessel.
- iv) To provide a mounting location for a catch-tray to catch target debris in the event of a target failure.

The components mounted from the ring are labelled in Figure 36

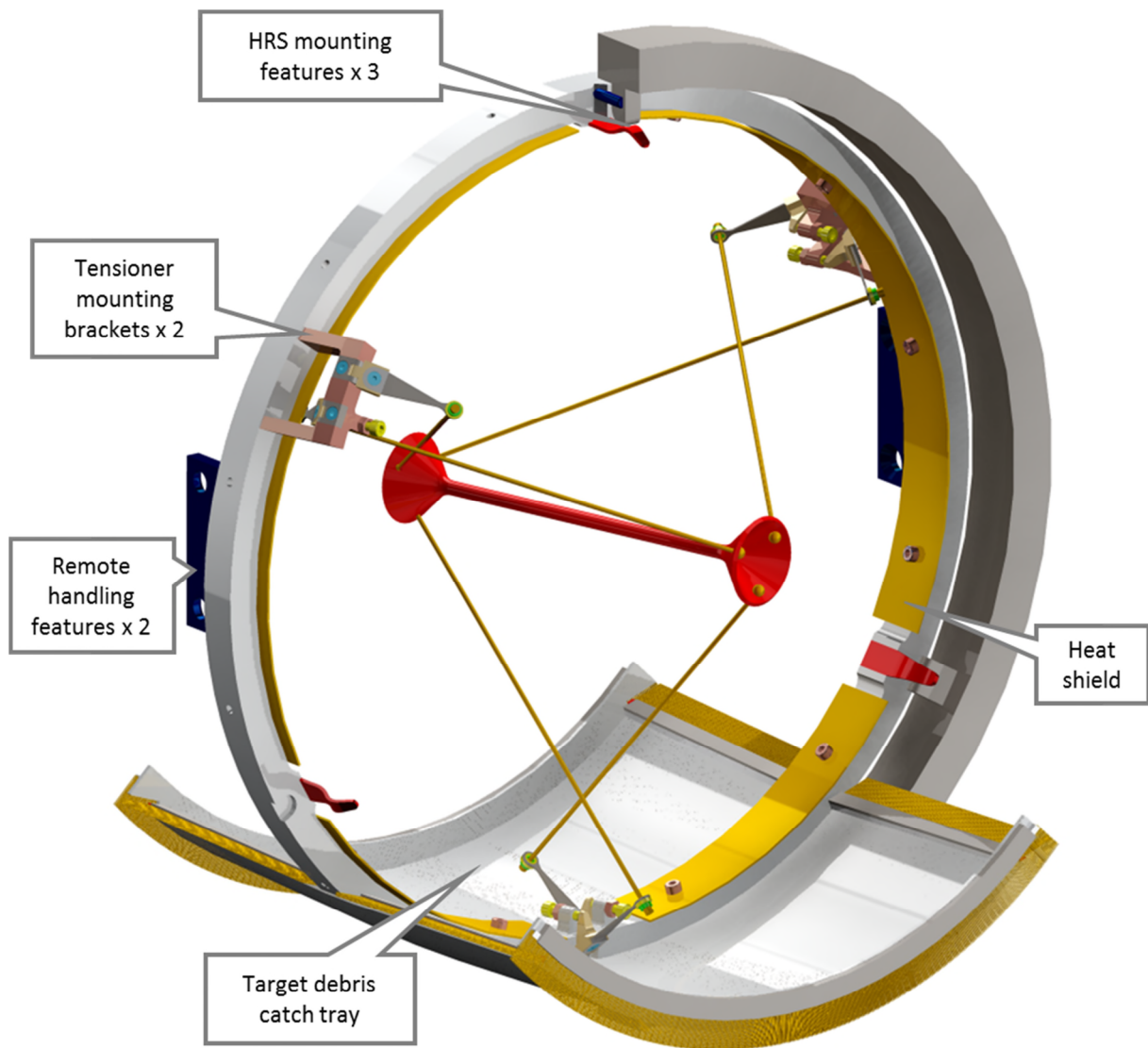


**Figure 36, Components mounted from the "mounting ring"**

The thermal loads and associated temperature rise in the target support ring have been discussed in a previous report [5]. It is estimated that the operating temperature in the support ring can be kept below 250°C regardless of any thermal conduction link via the HRS mounts to the vacuum vessel bore. With this in mind it is proposed to manufacture the ring from titanium which has a relatively small coefficient of thermal expansion and a suitable upper use temperature. In addition titanium has a relatively low density, allowing a low mass structure for ease of handling. In an early concept of the design aluminium was also considered as a material for the support ring, however this is thought to be too risky since it would rely on a good thermal connection to the HRS bore to keep the support ring temperature and associated thermal expansion in check.

We propose to investigate a thin sheet-metal heat shield designed to intercept the direct radiation heating path between the hot tungsten target and the support ring. This could potentially reduce the rate of radiative heat transfer to the support ring during beam operations. The effectiveness of such a heat shield is best investigated as part of the proposed follow-on prototype target heating tests.

### 2.7.2 Spoke tensioner mounting

In our early design concepts the spoke tensioners were mounted directly to the target wheel [3] [5]. Since the target is at an angle relative to the bore of the solenoid and the target ring, mounting directly from the ring in this way requires that either the spokes are of different lengths, that there are several different adjuster designs, or that the adjusters are mounted to the ring via brackets. It is desirable for ease and cost of manufacture to use equal length spokes and a single design for the adjuster. This leaves only the mounting to the ring via brackets option. Figure 37 shows how the target is mounted at an angle within the ring, highlighting the need for such a bracket. Figure 38 shows how such brackets could be used in order to allow equal length spokes. It can also be noted that as well as the spokes being equal lengths, the angles between the spoke and the target are equal in every instance.

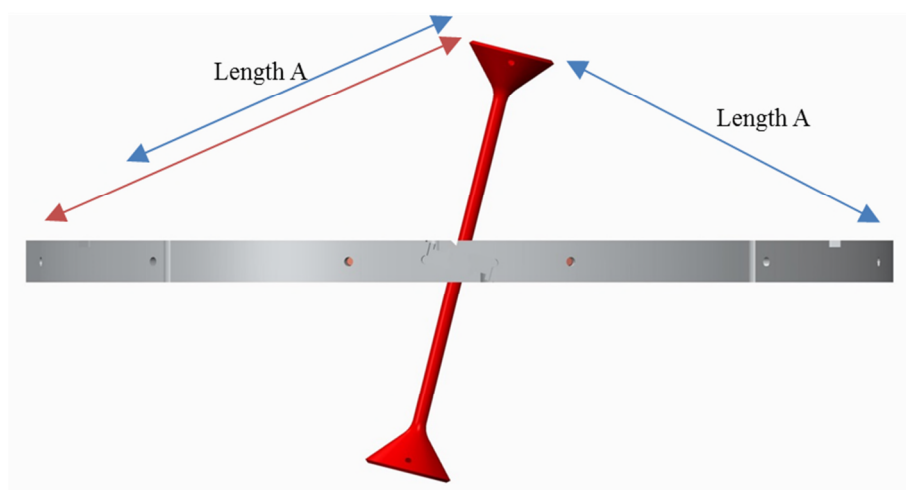


Figure 37, impact of target angle on equal spoke length design

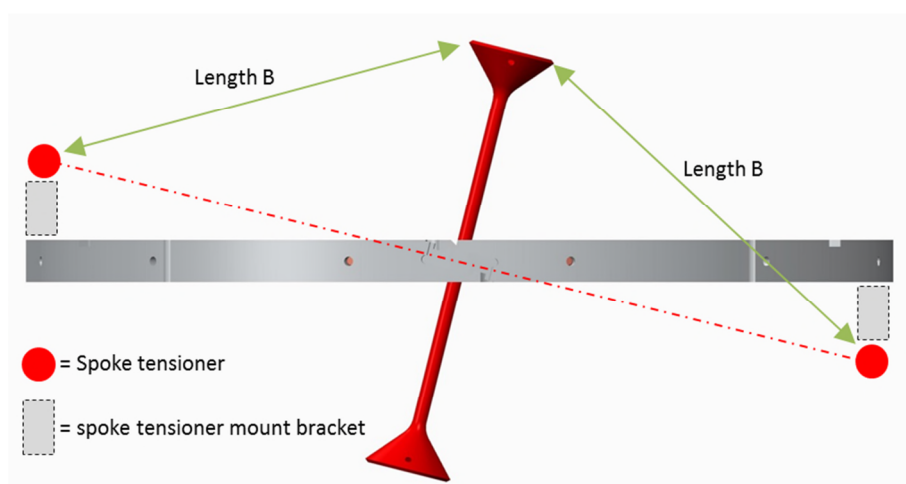


Figure 38, outline concept of adding spoke tensioner mounting brackets.

In our design the spoke tensioners have been grouped in pairs in order to allow the tensioners to be mounted with minimal material. There are 2 spokes at the 6 o'clock position, from

which the next 2 pairs of spokes are equally spaced around the ring ( $120^\circ$  apart). Figure 39 shows that there are 2 identical tensioner mounting brackets positioned at 10 o'clock and 2 o'clock position. It is believed that this spoke layout offers the simplest and lowest mass bracket configuration. Figure 40 shows how the tensioner mounting bracket can be used on the front of the wheel, and also flipped and used in reverse on the back side of the wheel. At the 6 o'clock position, no bracket is required, and the tensioners are mounted directly to the ring.

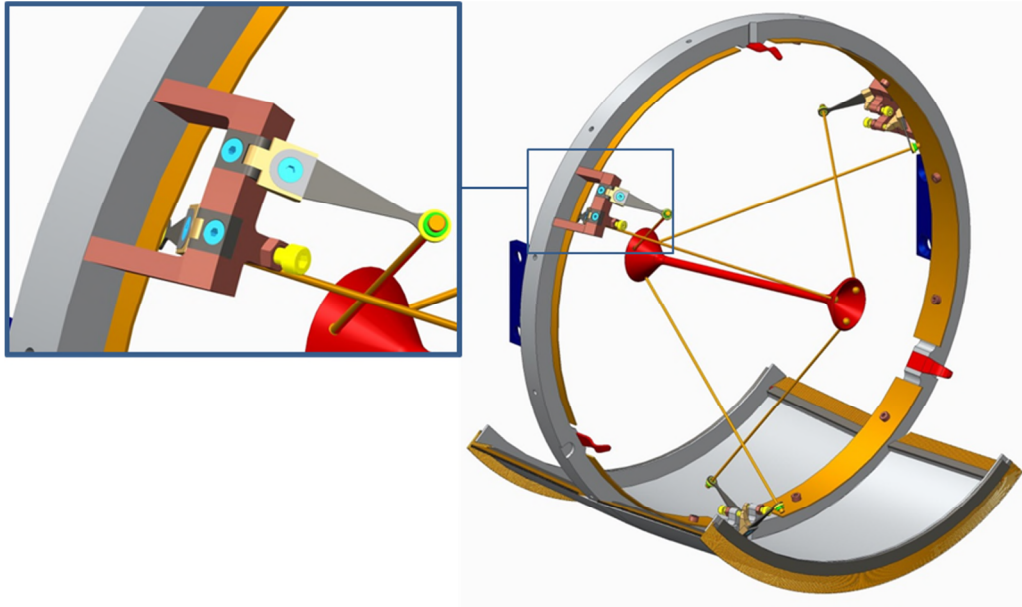


Figure 39, spoke tensioner mount brackets – 3D view

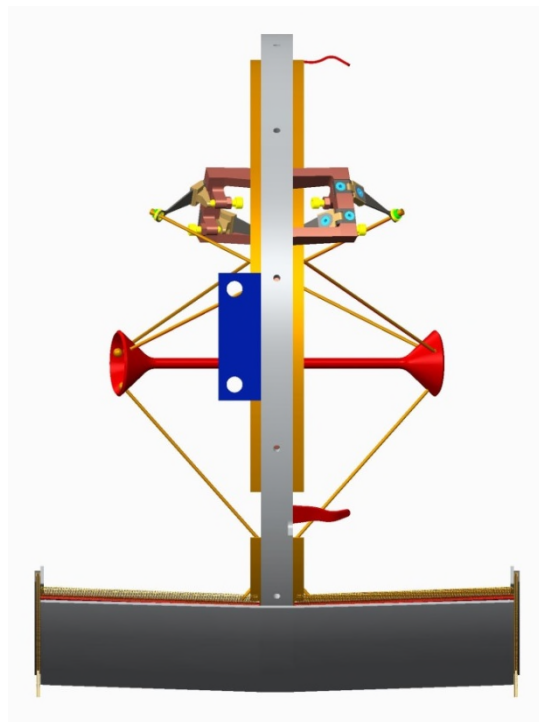


Figure 40, spoke tensioner mount brackets - side view

### 2.7.3 Spoke layout

Figure 41 shows an end-on view of the target and spokes. From this view, the layout of the spokes relative to the target can be more easily viewed. There are 3 spokes supporting each end of the target. The spokes are equally spaced,  $120^\circ$  apart. The spoke in the 6 o'clock position is offset from the vertical centreline of the target by 3 degrees. The 6 o'clock spoke is offset by the same rotation in reverse on the back side of the target, giving an angular offset of 6 degrees from front to back.

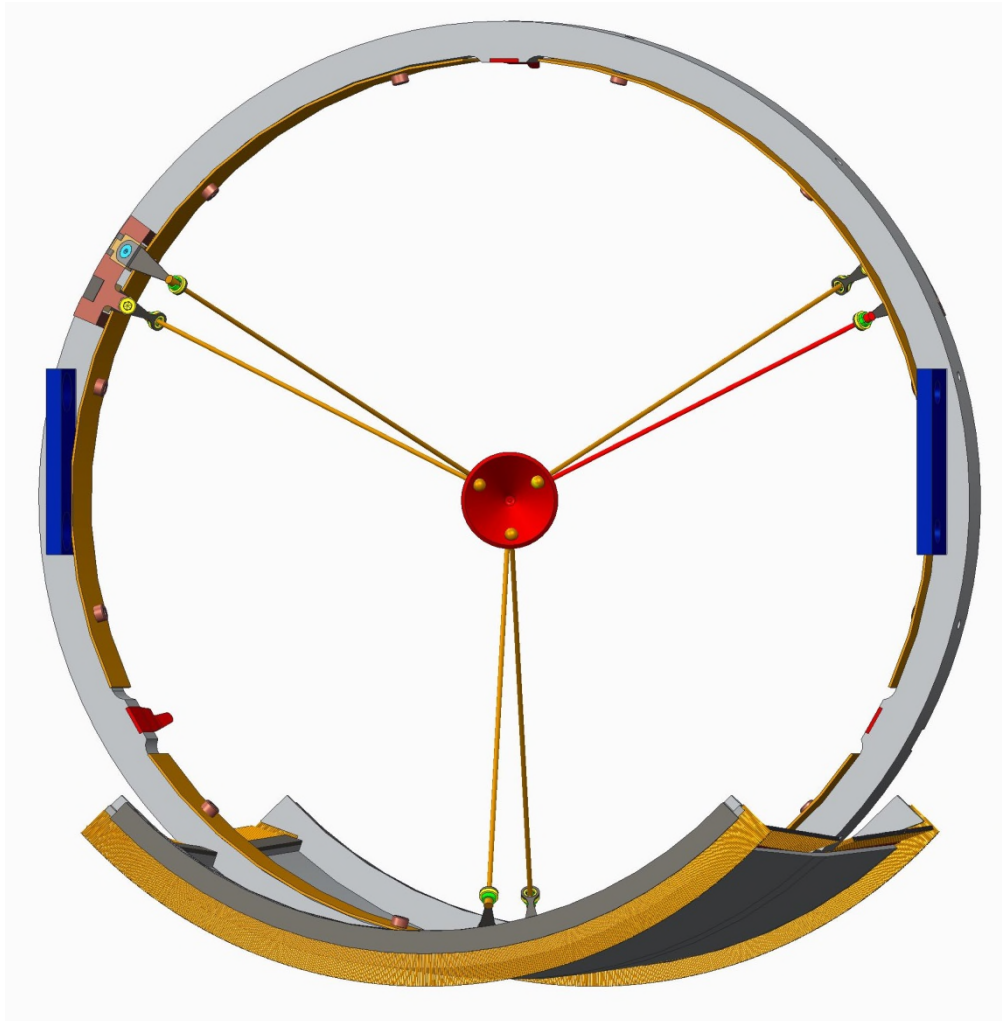


Figure 41, view on target end

## 2.8. Catch Tray

The titanium target mounting ring is viewed as a robust object. Conversely the components suspended inside the ring will be more fragile and prone to damage, particularly since tungsten is a brittle material at room temperature. In the event that a mechanical failure occurs in any of the suspension components it is thought most likely that this will induce sudden movement and perhaps failure of other parts. In an ideal handling scenario the target

structure would be housed within a vessel of its own such that any falling debris could be contained for ease of target remote replacement and disposal. However, the additional material required for such a vessel is deemed unacceptable. What we propose here instead is a “catch tray” to arrest and partially contain falling target components or debris. In this way debris may be prevented from obstructing the path of a failed target out of the bore, or obstructing the subsequent insertion of a replacement target. Potential target failure mechanisms are discussed in more detail in section 3 of this report.

Of particular concern is a failure scenario where a spoke fails, and the target dangles from the remaining spokes below the ring and impedes the exit of the target through the exchange window, or else, is retracted through the window and falls onto the floor of the hall. The catch tray is designed to prevent such a scenario, keeping the failed target parts within the original target envelope for ease of handling and disposal (for example Figure 42). An early concept of the catch tray raised concern about the possibility of parts missing the catch tray and becoming trapped underneath. Another concern raised was that the tray might cause the target to become jammed in the bore if the target is not withdrawn straight. A Failure Mode and Effect Analysis (FMEA) was carried out on the original concept, and some features added or modified as a result. The current proposal features a sheet titanium tray, with relief angles as shown in Figure 43 to allow the target to be inserted/removed from the bore without becoming wedged. The tray also features soft metallic bristles that stop large debris from falling under the catch tray and becoming wedged underneath, see for example Figure 44.

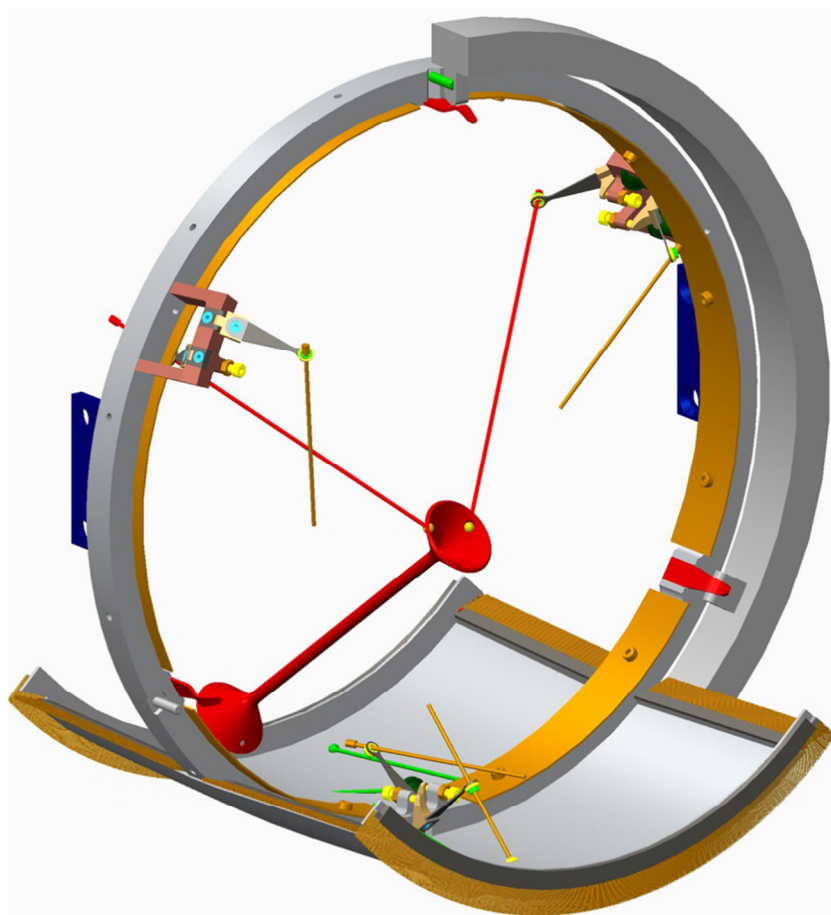


**Figure 42, A potential target failure scenario**

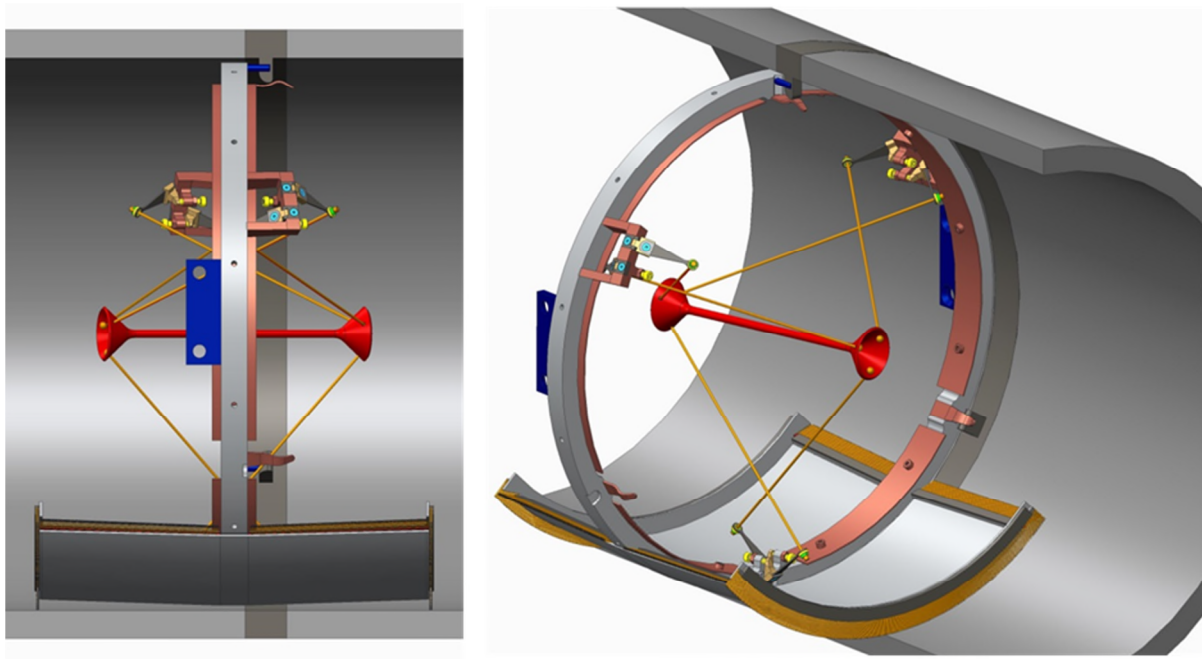


Figure 43, Target with catch tray



Figure 44, A metallic strip brush

The Failure Mode and Effect Analysis considered six drop zones in which target debris could potentially fall in the event of a failure as shown in Figure 45. With respect to the incoming proton beam zones 3 and 5 are upstream and zones 2 and 4 are downstream of the target ring. Zones 1, 2, and 3 are viewed as the most likely regions for debris to fall, hence the catch tray is designed to cover these areas. Zones 4 and 5 account for debris thrown further afield into the HRS vessel bore. Zone 6 accounts for debris that may potentially slide under the catch tray. The impact and likelihood scoring for the FMEA is shown in Table 4, and the FMEA summary is included below. The items attracting the highest impact scores are those with the potential to wedge the target structure in the HRS bore.

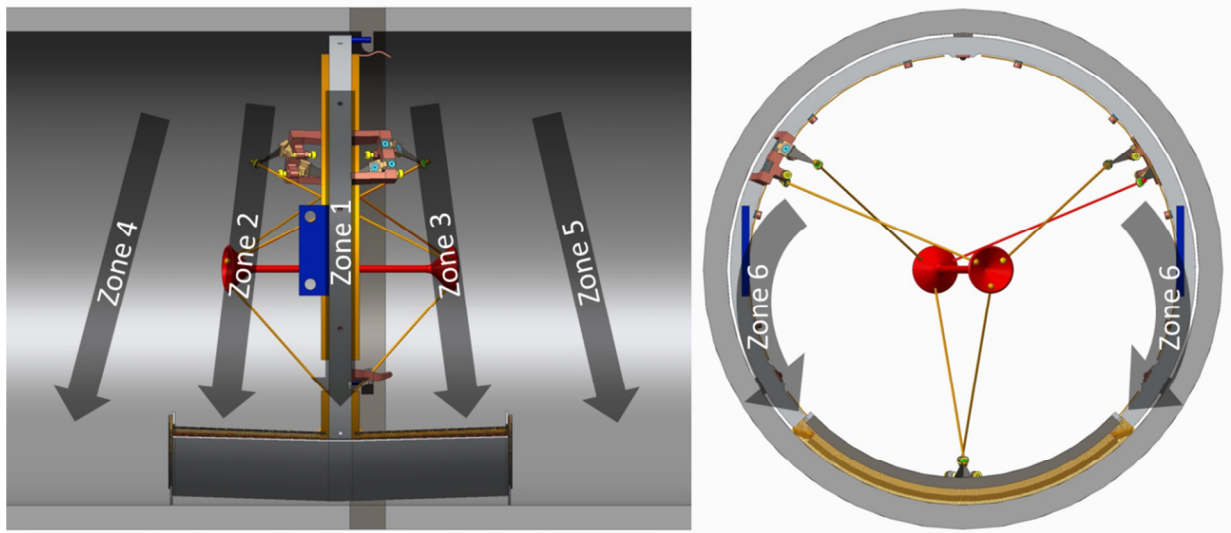


Figure 45, Debris drop zones for the FMEA

Table 4, Impact and likelihood scoring for the FMEA

Likelihood			
Very Low	Low	Medium	High
1	2	3	4

Impact			
None	Low	Medium	High
0	1	2	3

	Item number	Possible outcomes	Result	Impact on target exchanger	Other impact	Likelihood	Impact	Score	Mitigation	Residual impact on target exchange	Other residual impact	Likelihood	Impact	Residual score
Target fails in service	1	Target is in tact	No debris	None		4	0	0	NA	None		4	0	0
	2	Target structure distorted, but not become detached	No change for handling	None		4	0	0	NA	None		4	0	0
	3	Target debris falls into zone 1	Captured by tray	None		4	0	0	NA	None		4	0	0
	4	Target debris falls into zone 2	Captured by tray	None		4	0	0	NA	None		4	0	0
	5	Target debris falls into zone 3	Captured by tray	None		4	0	0	NA	None		4	0	0
	6	Target debris falls into zone 4	Target debris sits in the down-stream HRS bore	Potential for target module to become wedged in bore		2	3	6	sweeper brush on front of catch tray, or sweep in front of catch tray	Debris swept down-stream, but risk of debris missed by sweeper jamming target	Small amount of radioactive debris abandoned in the tapered section of the bore	1	3	3
	7	Target debris falls into zone 5	Target debris sits in the up-stream HRS bore	None	Debris not extracted	2	2	4	Leave debris in bore (or remove with special tool)	None	Small amount of radioactive debris abandoned in the bore	2	2	4
	8	Target debris falls into zone 6	Debris falls under catch tray	Potential for target module to become wedged in bore		2	3	6	Brushes on the side of the tray to prevent debris falling under tray	Large debris excluded, but small risk of very small debris evading brush and falling under tray		1	3	3
Target disintegrates during extraction	9	Target debris falls into zone 1	Captured by tray	None		3	0	0	NA	None		3	0	0
	10	Target debris falls into zone 2	Captured by tray	None		3	0	0	NA	None		3	0	0
	11	Target debris falls into zone 3	Captured by tray	None		3	0	0	NA	None		3	0	0
	12	Target debris falls into zone 4	Target debris sits in the downstream HRS bore	Debris in the path of target extraction		2	3	6	sweeper brush on front of catch tray, or sweep in front of catch tray as the target is removed	Large debris swept down-stream, but small risk of very small debris evading brush and snagging tray	Small amount of radioactive debris abandoned in the tapered section of the bore	1	3	3
	13	Target debris falls into zone 5	Target debris sits in the downstream HRS bore	Debris in the path of replacement target	Debris not extracted	2	3	6	sweeper brush on rear of the catch tray, (or remove with special tool)	Large debris swept up-stream, but small risk of very small debris evading brush and jamming tray	Small amount of radioactive debris abandoned in the bore	1	3	3
	14	Target debris falls into zone 6	Debris falls under catch tray	Potential for target module to become wedged in bore		2	3	6	Brushes on the side of the tray to prevent large debris obstructing target extraction	Debris is directed into the catch tray, preventing it jamming under the target module		1	3	3
	15	Trailing debris attached to target wheel	Target debris exceeds target wheel envelope	Target does not fit through HRS extraction port		1	3	3	Larger catch tray?	Target does not fit through HRS extraction port		1	3	3

## 2.9. Mounting to the HRS

The mounting of the target ring to the HRS should be as simple as possible for ease of remote handling. It should provide a stable and repeatable interface, and allow expansion of the ring relative to the HRS. It is not required to provide a good thermal link to the HRS in vacuum. In view of these requirements, a simple “push-pull” cantilever latch mechanism is proposed for mounting the target in the HRS. This could be done with cantilever springs rather like those that have been proposed for the spoke tensioning springs. The geometry would be designed such that the springs pull the target into the bore against a set of dowel stops. This mechanism is shown conceptually in Figure 46.

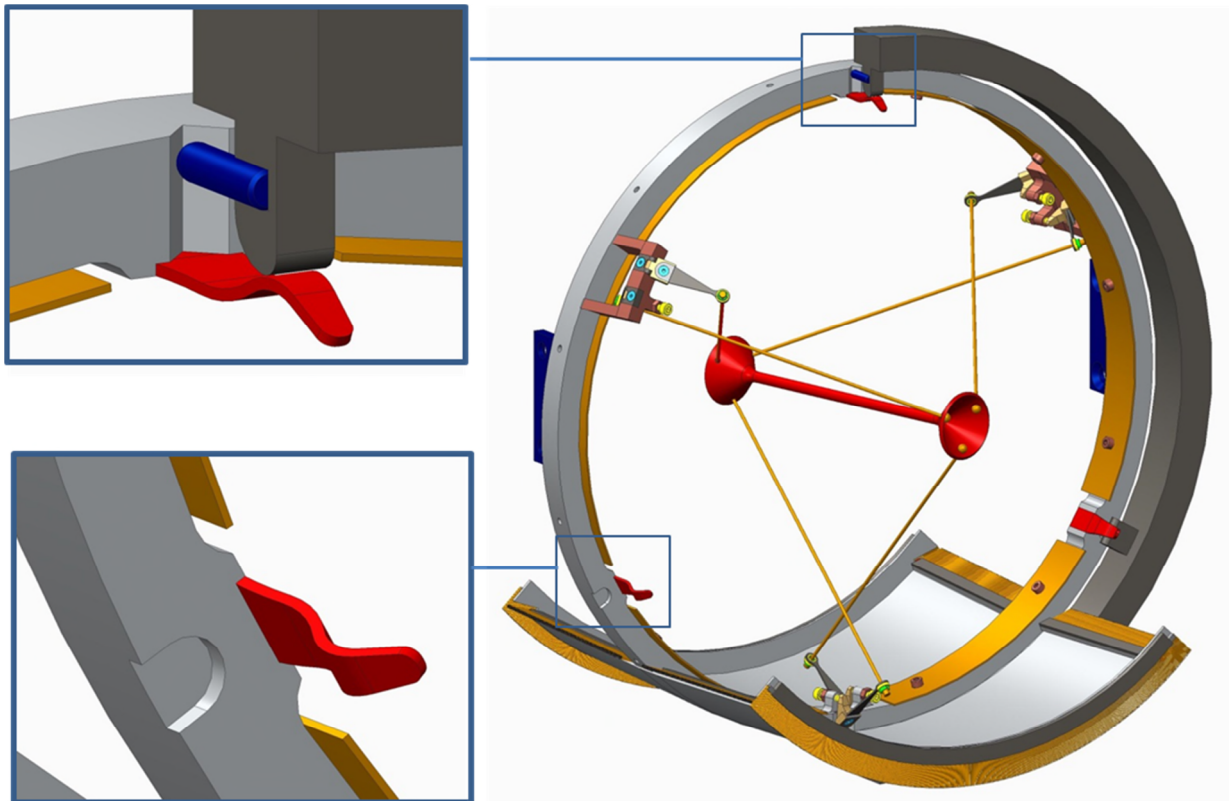


Figure 46, Spring mounting concept

In this design there are three springs, and three points of contact between the target ring and the HRS bore. Two of these points of contact consist of a spherical tipped dowel on a flat face, and the other is a spherical tipped dowel in a Vee groove. Restraint of the lateral rotation degrees of freedom can be achieved with the 3 springs and 3 face contacts. The final degree of freedom (rotation about the bore axis) is achieved by the spherical tipped dowel spring loaded into the vee groove. This is a concept and would require some development work and prototyping in order to make it a detailed and defensible design.

### 3 Failure Mechanisms Analysis for a Radiation Cooled Target

#### 3.1. Overview

The continuous high-temperature operation associated with a radiation-cooled target introduces a number of potentially lifetime limiting high-temperature damage mechanisms. These damage mechanisms, summarised in Table 5, are addressed in this section of the report.

**Table 5, Summary of damage mechanisms for a radiation-cooled target**

Item	Description	Measures Taken	Likely- hood	Impact	Score	Potential Mitigation Strategies
Cyclic Thermal Stress (section 3.2)	The cyclical nature of the primary proton beam results in time varying thermal stresses in the target that may lead to a fatigue failure.	<ul style="list-style-type: none"> <li>Target material selection.</li> <li>High temperature pulsed fatigue performance of tungsten test samples indicate &gt; 1 year lifetime.</li> <li>Encouraging data at increased pulse intensity.</li> </ul>	2	3	6	<ul style="list-style-type: none"> <li>Reduction in average beam power resulting in a reduced target equilibrium temperature.</li> <li>Similarly, fins or convective cooling.</li> <li>Increase beam duty factor (i.e. closer to continuous heating).</li> <li>More frequent target exchange.</li> </ul>
Creep (section 3.3)	Progressive permanent creep deformation of the target may adversely affect pion production and could eventually lead to a mechanical failure in the target structure.	<ul style="list-style-type: none"> <li>Target material selection.</li> <li>Optimisation of "hub" joints to limit peak temperature in the supports.</li> <li>Creep tests indicate that applied stress and operating temperature are critical parameters</li> </ul>	3	2	6	<ul style="list-style-type: none"> <li>A finned target surface to reduce the equilibrium operating temperature. Longitudinal fins would have added benefit of increasing stiffness/strength in bending.</li> <li>Reduce self-weight stress in the target: Larger target diameter or "tapered" target geometry, shorter target length or move supports inboard.</li> <li>Reduce applied support stress in the target: redesign structure for reduced longitudinal load.</li> <li>More frequent target exchange.</li> <li>Adopt a forced convection cooling scheme to ensure low temperature operation.</li> <li>Reduction in average beam power resulting in a reduced target equilibrium temperature.</li> </ul>
High Temperature Chemistry (section 3.4)	Residual gasses in the target vessel may react with hot parts of the target resulting in progressive loss of target material.	<ul style="list-style-type: none"> <li>Vacuum / leak tests indicate maximum pressure <math>1e^{-5}</math> Torr for 1 year life.</li> </ul>	2	2	4	<ul style="list-style-type: none"> <li>Improve performance of vacuum system to achieve <math>10^{-6}</math> Torr or better at the target.</li> <li>Increase target dimensions to give some "tolerance" to erosion.</li> <li>More frequent target exchange.</li> <li>Adopt a forced convection cooling scheme to ensure low temperature operation.</li> </ul>
Material Loss by Evaporation (section 3.5)	At high temperature and low pressure the target material may be "eroded" directly by evaporation.	<ul style="list-style-type: none"> <li>Target material selection.</li> <li>Calculations predict negligible evaporation rate for tungsten target.</li> <li>No evaporation apparent during long-term tests.</li> </ul>	1	2	2	<ul style="list-style-type: none"> <li>Reduction in average beam power resulting in a reduced target equilibrium temperature.</li> <li>Increase target dimensions to give some "tolerance" to erosion.</li> <li>More frequent target exchange.</li> <li>Adopt a forced convection cooling scheme to ensure low temperature operation.</li> </ul>
Radiation Damage at high temperature (section 3.6)	Damage and/or gas production in the target due to bombardment by the primary proton beam may lead to a progressive degradation in material properties.	<ul style="list-style-type: none"> <li>Peak fluence and lifetime DPA similar to ISIS targets.</li> <li>However the temperature regime is completely different and therefore damage rates are not well known.</li> </ul>	3	3	9	<ul style="list-style-type: none"> <li>Larger beam spot to reduce peak fluence.</li> <li>Reduction in average beam power to reduce peak fluence.</li> <li>More frequent target exchange.</li> </ul>
Combination of Damage Mechanisms	Some combination or coupling of the damage mechanisms listed above may result in a shorter target life. For example: - fatigue / creep - rad. damage / fatigue	<ul style="list-style-type: none"> <li>Simultaneous damage mechanisms have not been tested to date.</li> </ul>	3	3	9	<ul style="list-style-type: none"> <li>More frequent target exchange?</li> </ul>

Some of the damage mechanisms described above can be expected to lead to a gradual degradation in physics performance, for example by chemical erosion of the hot target material or progressive creep deformation of the target rod. However, the present design relies on the structural integrity of the tungsten target. Little is known about the effect on the recrystallized tungsten of radiation induced transmutation and atomic displacements due to the 8GeV focused beam. In addition the tungsten will be brittle when it cools down due to beam trips or scheduled stops and so any tungsten components will be highly sensitive to any knocks or significant vibrations. Therefore we anticipate that at some level of accumulated damage in service, or perhaps during target replacement handling operations, a catastrophic failure of the target or target suspension structure may occur resulting in target debris falling into a disorderly heap. We note that given the lack of any good online diagnostic for condition monitoring of the target it will likely not be possible to predict the timing of such a failure. The success or otherwise of a preventative maintenance schedule is therefore rather difficult to guarantee and this type of catastrophic failure must be anticipated. By way of example a target failure of this kind is illustrated in Figure 47.

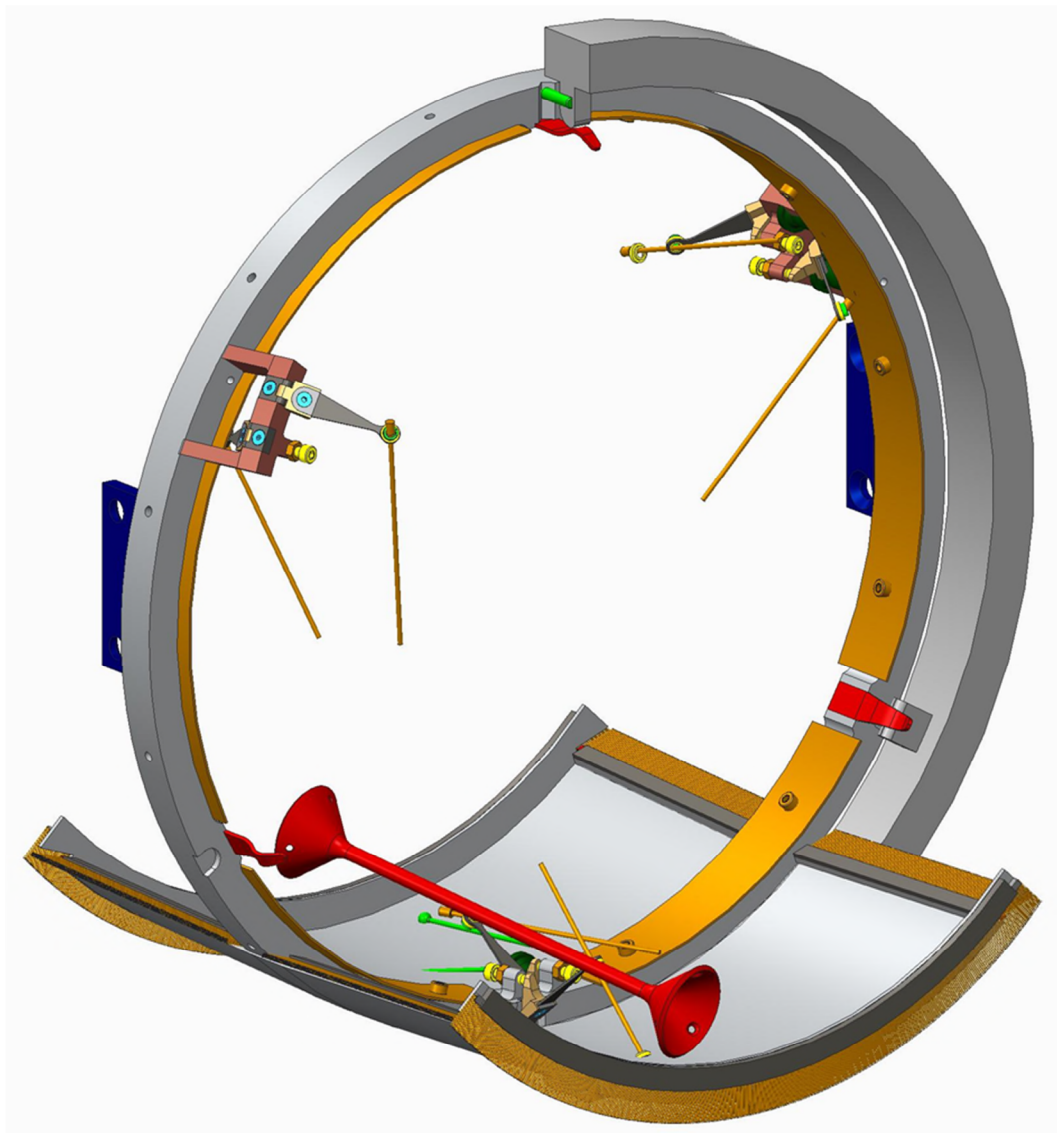


**Figure 47, A failure scenario resulting in a heap of target debris**

### 3.2. Cyclic Thermal Stresses

We have previously reported on the issue of cyclic thermal stresses and the expected high temperature thermal fatigue performance of the target [4] [5] [6]. For completeness a short summary is included here.

Heat will be generated in the target material when the primary proton beam interacts with it. The non-uniform spatial distribution of this heating combined with the conduction and radiation heat transfer mechanisms at play will result in temperature gradients within the target which in turn generate a thermal stress field. Since the beam is pulsed there will be a cyclical component to the thermal stress that may have a negative impact on the target operating life due to cyclic hardening and fatigue.

The Mu2e beam is expected to cycle on a frequency of 0.75 Hz. Within that cycle there is a “Beam on” period during which protons are spilled onto the target, followed by a “beam off” period where there are no beam/target interactions. The time structure of the beam during the “beam on” part of the cycle is shown in Figure 48. The top graph shows the Recycler Ring beam intensity as a function of time. The bottom plot shows the Delivery Ring beam intensity as a function of time. Proton batches are injected into the Recycler at the beginning of the cycle and again at the fourth tick. After each injection, the beam is bunched with 2.5 MHz RF and extracted one bunch at a time [10].

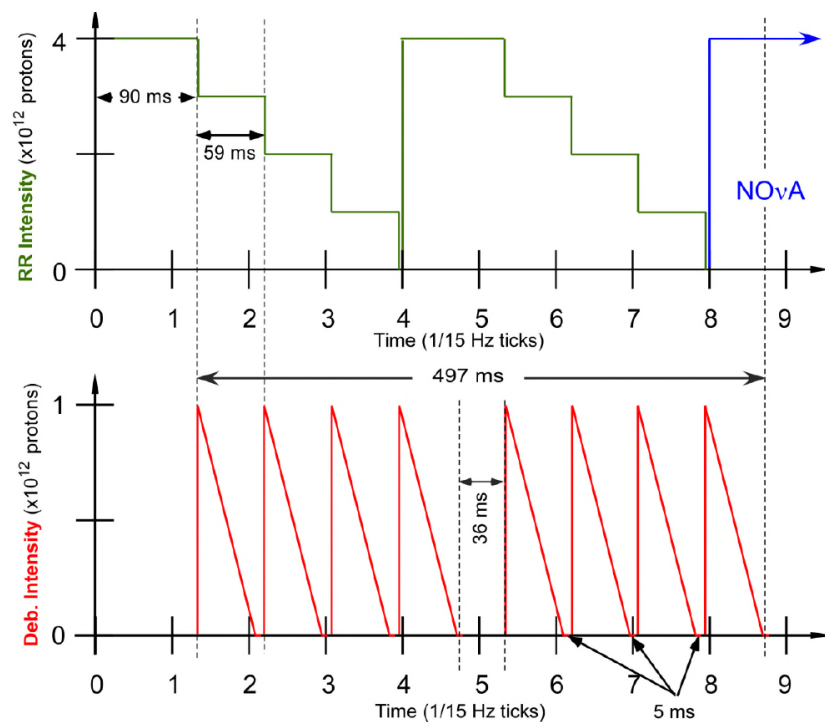
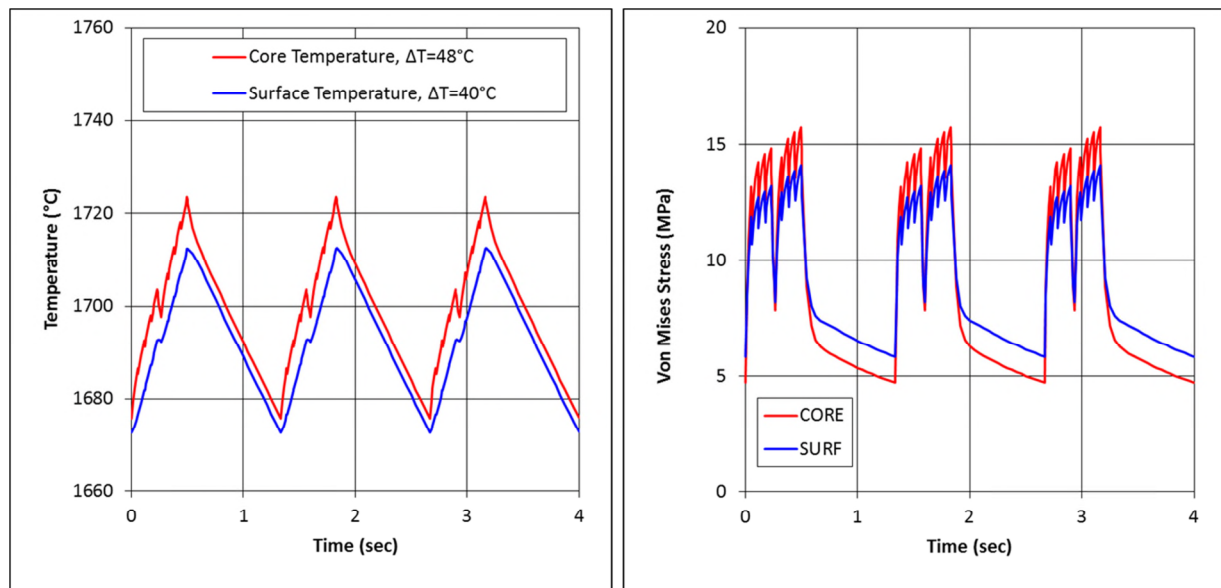


Figure 48, The Mu2e beam time structure [10]

At the target we essentially have two competing mechanisms at play. During “beam on” periods thermal stresses build up in the target rod as its centre is preferentially heated by the Gaussian beam. At the same time this is countered by thermal conduction within the target rod which tends to equalise any temperature variation, thus reducing the thermal stress. A calculation of the target temperature and stress cycle resulting from the expected beam time structure is shown in Figure 49.



**Figure 49, Temperature (left) and thermal stress cycles (right) in the target under steady-state operation**

Under steady-state operating conditions the expected peak cyclic temperature change at the target core and target surface are about 48°C and 40°C respectively. It is clear to see that the stresses increase when the beam is on, and decrease when the beam is off. The magnitude of the calculated stress is well below the stated elevated temperature strength for the tungsten target material. However, the repetitive cyclical nature of this thermal stress may still impact on the target life and a large safety margin is required to offset unknown radiation damage effects and mechanisms at the high operating temperature.

With this in mind a novel off-line (out of beam) test able to replicate the cyclical temperature and thermal stress expected in the target was used as a qualification tool. In the test, electrical current pulses are passed through a specially shaped sample that is mounted inside a vacuum vessel. The sample geometry is designed so that the current pulse will preferentially heat the centre of a little disk, generating radial temperature gradients in the disc analogous to those generated by the Gaussian beam in the target. Figure 50 shows one of these specially shaped samples under preparation. We have previously described how in the test both the equilibrium temperature and pulsed temperature rise in the sample can be approximately matched to those calculated for the target. In addition, an accelerated lifetime test is possible by running the test at an exaggerated pulse repetition rate of 10 – 20 Hz.

The experience and data obtained has been encouraging. To date two samples have been tested to over 100 Million cycles, one mounted in a vertical configuration, and the other mounted horizontally. Neither sample had failed after 100 Million cycles, roughly equivalent to 4 years of continuous operation of the Mu2e target. One of these samples was subsequently run at an increased intensity in order to induce a failure. Even under much more severe conditions than expected for the target, this sample survived for another 37 Million cycles before a failure was observed. Again this is encouraging. Figure 51 shows a vertically mounted sample under test, and the failure induced by running in a severe condition.

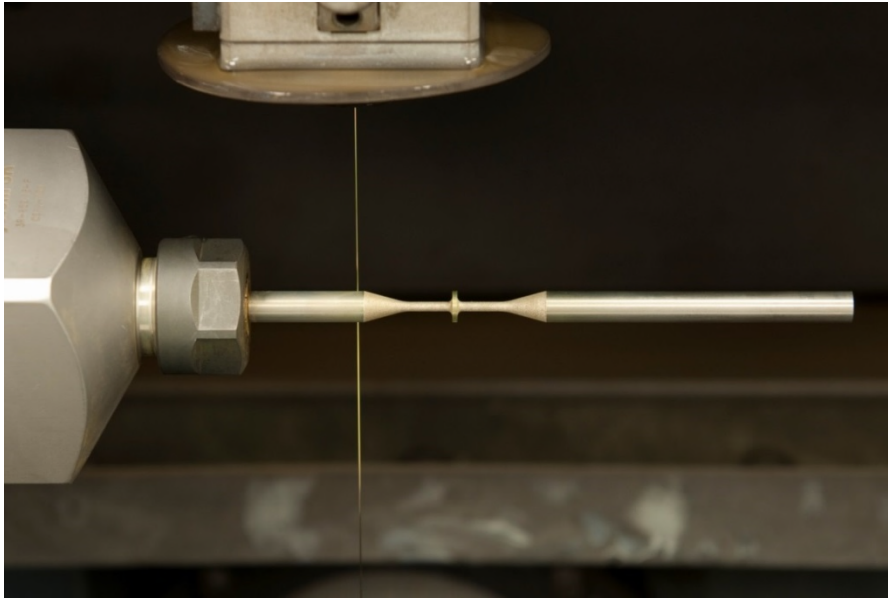


Figure 50, A specially shaped tungsten sample under preparation

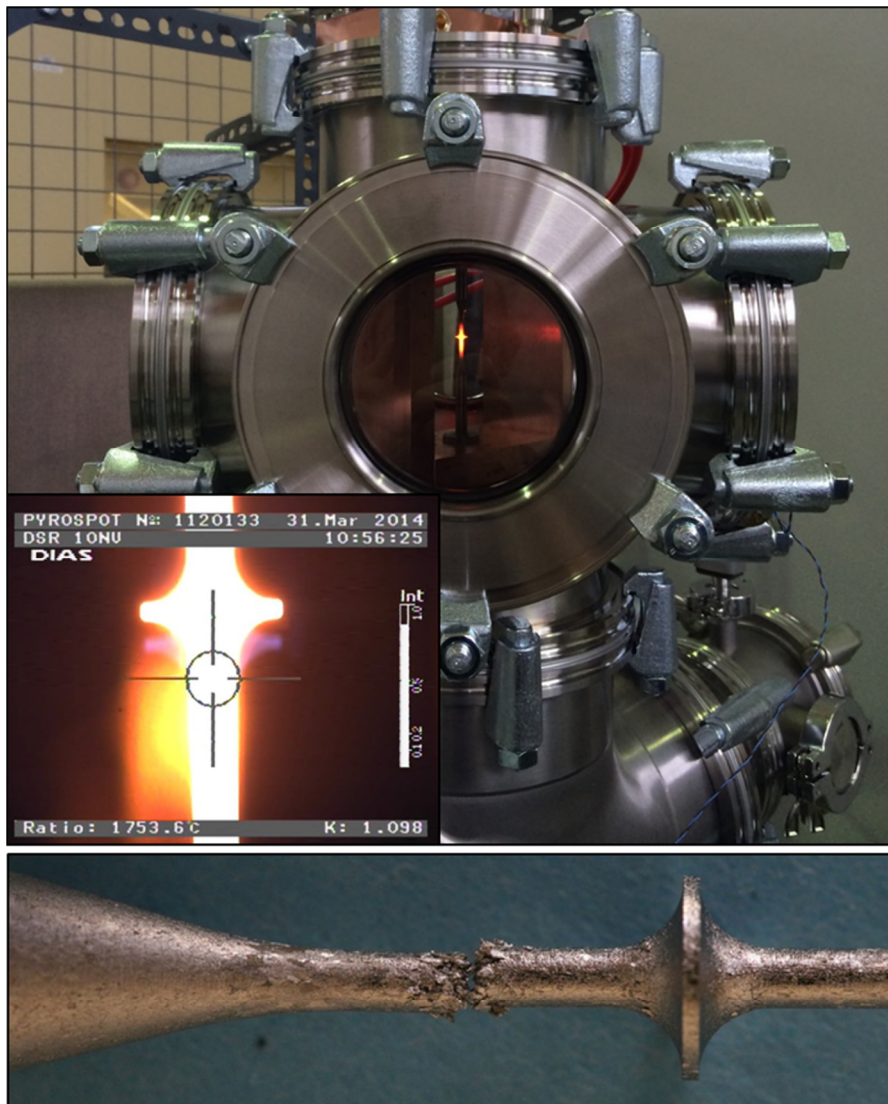


Figure 51, The test underway (top), temperature monitor output (inset), and a failed sample (bottom)

### 3.3. Creep

#### 3.3.1 Introduction

For our purposes creep may be defined as a progressive (time-dependent) permanent deformation that occurs in a material at elevated temperature and constant stress. The onset of creep is highly material dependent. Generally creep becomes of engineering significance at a service temperature that is greater than half of the melting temperature, and notably, at stresses well below the elevated temperature yield stress of the material in question. It follows that creep may limit the service life of any high temperature structural component.

In a previous report [5] we examined the potential impact of creep on the performance of the tungsten spokes in the Mu2e target structure. We concluded that creep effects could be sufficiently mitigated by limiting the peak temperature in the spokes to be less than 1000°C and we asserted that this temperature limit could be respected through proper design of the target/spoke end connections. In this report we turn our attention to the tungsten target rod which is where we expect the most extreme temperatures in the target structure will occur. Indeed, it has been calculated [5] that during beam operation the Mu2e target rod may experience temperatures up to around 1700°C. We note that at temperatures above about 1300°C tungsten will tend to recrystallise and that in this regime a limited service life should be expected. The target rod is considered a structural component in the sense that it must withstand stresses due to self-weight and any additional forces that may be applied by its supporting structure. Any significant sagging of the target rod under its own weight may adversely affect pion production rates and could even lead to a mechanical failure in the target structure. Clearly this must be avoided.

#### 3.3.2 Test method

Rather than follow a standard creep test method, the approach taken here has been to approximate the condition of the Mu2e target as closely as possible. To this end cylindrical samples were mounted horizontally in a test rig, supported at either end with the only applied mechanical load being their own self-weight. A direct current was used to heat the samples resistively and the peak sample temperature, occurring at the mid-span, was monitored using an optical pyrometer. A photograph of the apparatus with a sample under test is shown in Figure 52.

The tungsten samples were mounted in a water-cooled fixture that could be placed inside a vacuum vessel to allow heating to take place in a vacuum environment. Tests were performed at a vacuum level of  $10^{-6}$  Torr or better in order to avoid any significant oxidation of the sample. At one end the sample was clamped in a fixed collet, while at the other end it was able to slide through a graphite bush allowing for any longitudinal thermal expansion to take place. The unsupported sample length (span) was 175 mm. A tungsten fiducial post mounted on the sample support fixture was positioned directly below the sample mid-point leaving a 2-3 mm gap between the tip of the post and the sample. The gap dimension was then monitored via an alignment telescope viewing through the glass vessel window. Measurements could be taken on-line, i.e. without the need to cool the sample down. Typically one measurement would be taken each day during a test that could run for several weeks.

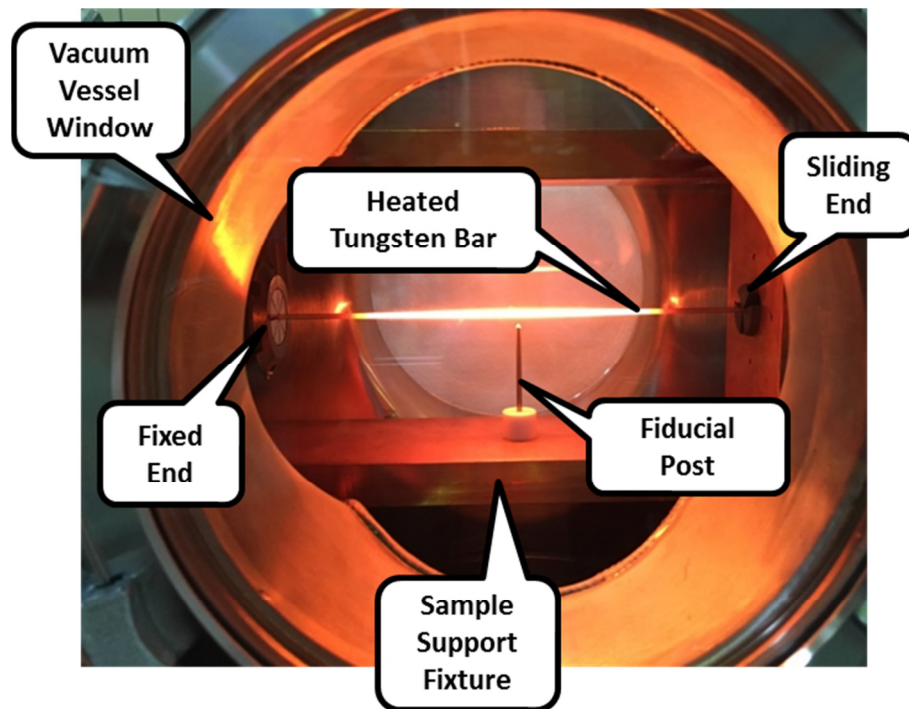
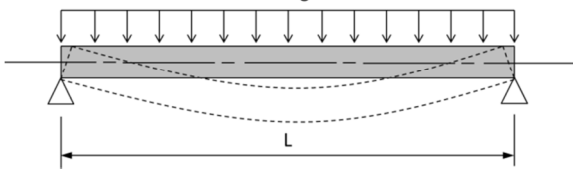
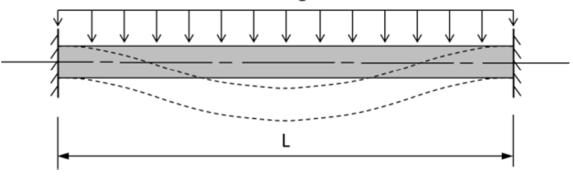
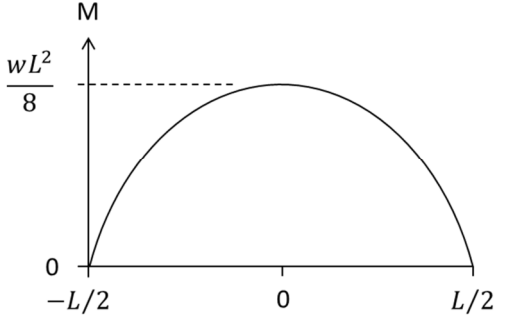
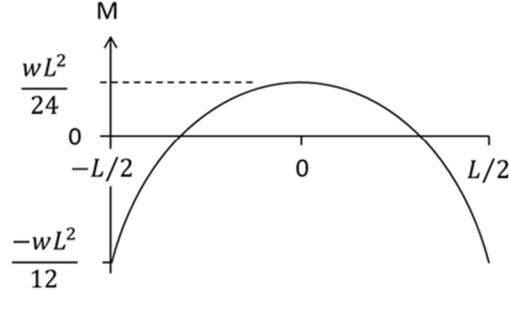
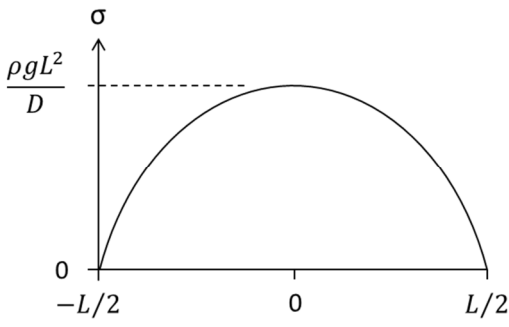
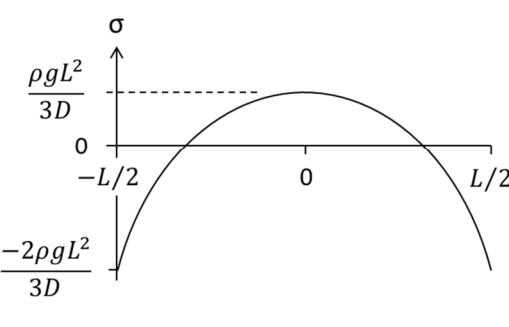


Figure 52, Sag Test Apparatus

The method of support in the sag test clearly differs from that of the proposed bicycle wheel target structure. It has been said that the target support more closely resembles the classical boundary condition where the ends of the target rod are free to rotate, whereas the sag test more closely resembles the classical boundary condition where end rotations are prevented. Table 6 sets out and compares a summary calculation of self-weight bending stress for those two boundary conditions according to classical beam theory. We can see that the maximum bending stress, which occurs at the mid-span, is proportional to the square of the unsupported length, and is inversely proportional to the diameter. The maximum bending stress is three times higher in the boundary case with free ends (i.e. the target) than it is in the boundary case with fixed ends (i.e. the test). In the sag test we can compensate for this by reducing the sample diameter by a factor of three compared to the target. This is convenient since, in any case, our test rig is not able to deliver sufficient power to heat a 6.3mm diameter “target sized” rod and only smaller samples up to a maximum diameter of 4 mm could be used.

Thermal conduction from the heated sample into the water cooled fixture meant that it was not possible to achieve a uniform temperature along the whole length of the sample. Instead the sample temperature varied from a minimum at the ends where thermal conduction was the dominant heat transfer mode, to a maximum at the mid span where thermal radiation was the dominant heat transfer mode. This is rather similar to the Mu2e Target which has cooler ends partly due to the non-uniform beam energy deposition and partly due to conduction from the target rod into the end “hubs” which act as radiator surfaces. Figure 53 shows a calculation for the temperature distributions in the samples tested (black lines) compared to a calculation of the temperature distribution along the Mu2e target from a previous report [5].

**Table 6, Classical beam theory applied to the target configuration (left) and sag test configuration (right)**

Target	Sag Test
<p>Assumed boundary condition: ends free to rotate</p> 	<p>Assumed boundary condition: end rotations prevented</p> 
<p>Distributed load</p> $w = \frac{\pi D^2 \rho g}{4}$	<p>Distributed load</p> $w = \frac{\pi D^2 \rho g}{4}$
<p>2<sup>nd</sup> moment of area</p> $I = \frac{\pi D^4}{64}$	<p>2<sup>nd</sup> moment of area</p> $I = \frac{\pi D^4}{64}$
<p>Central bending moment</p> $M_{centre} = \frac{wL^2}{8}$	<p>Central bending moment</p> $M_{centre} = \frac{wL^2}{24}$
<p>Central bending stress</p> $\sigma_{centre} = \frac{My}{I} = \frac{\rho g L^2}{D}$	<p>Central bending stress</p> $\sigma_{centre} = \frac{My}{I} = \frac{\rho g L^2}{3D}$
<p>Bending Moment plot</p> 	<p>Bending Moment plot</p> 
<p>Bending stress plot</p> 	<p>Bending stress plot</p> 

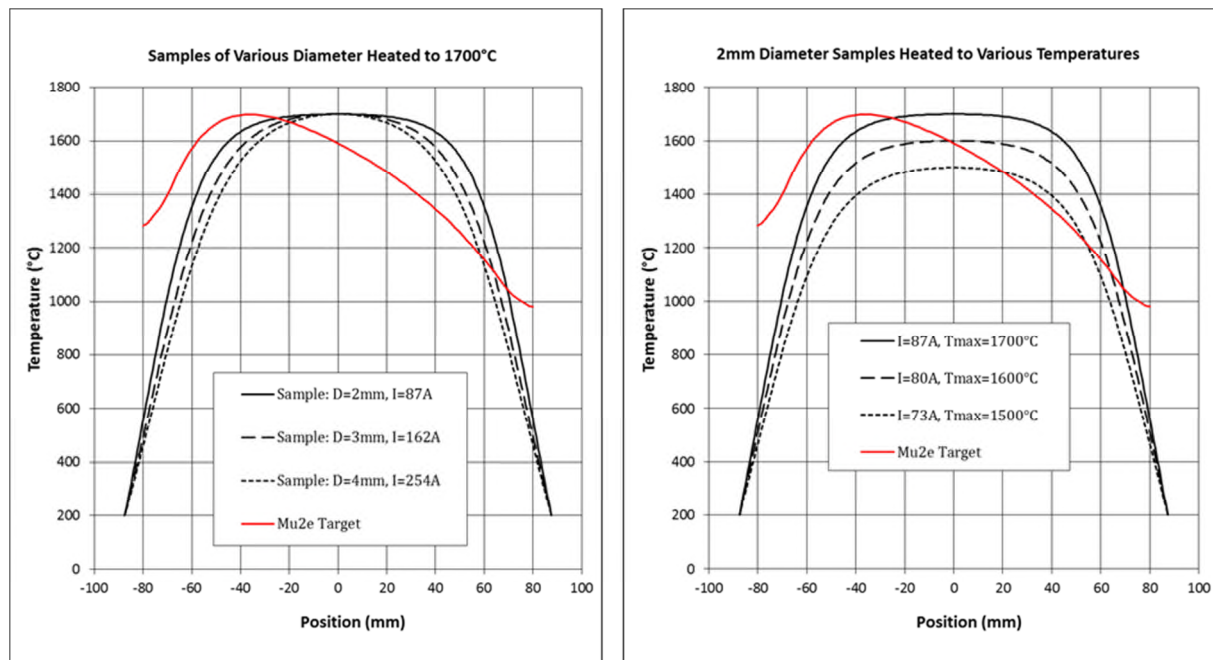


Figure 53, Longitudinal temperature distribution calculated for the sag test samples (black) compared to a calculation for a bare tungsten Mu2e Target (red)

### 3.3.3 Results

In total seven samples were tested. These ranged from two mm to four mm in diameter and 1500°C to 1700°C in peak temperature. Five of the samples were pure tungsten sourced from Goodfellow Cambridge Ltd. [11]. The other two samples were a dispersion strengthened material designated WL10 that is tungsten doped with 1% lanthanum oxide and is marketed by Plansee High Performance Materials [12] as “anti-sag” tungsten. This material is under consideration as a DEMO divertor plate [13] [14] being the only material able to meet the creep strength requirements. It is believed that this material has an elevated recrystallisation temperature compared to pure tungsten. All of the samples took the form of 230 mm long centreless ground rods.

Figure 54 shows a comparison of results for 2mm diameter samples tested at a 1500°C, 1600°C and 1700°C peak temperature (left), and for 2mm and 3mm diameter samples both tested at 1700°C (right). A power law fit of the form  $y = Ax^B$  was applied to the test data and is shown as a dashed black line. The slope of the dashed fit line at 30 days was determined and marked on the plots in red. A post-heating photograph of one of the samples is shown in Figure 55 to give an indication of the deformed shape. Figure 56 is concerned with the difference in response between pure tungsten (denoted W) and doped tungsten (denoted WL10). A test at 1500°C is shown on the left and a test at 1700°C is shown on the right. All of the samples in Figure 56 are 2 mm in diameter.

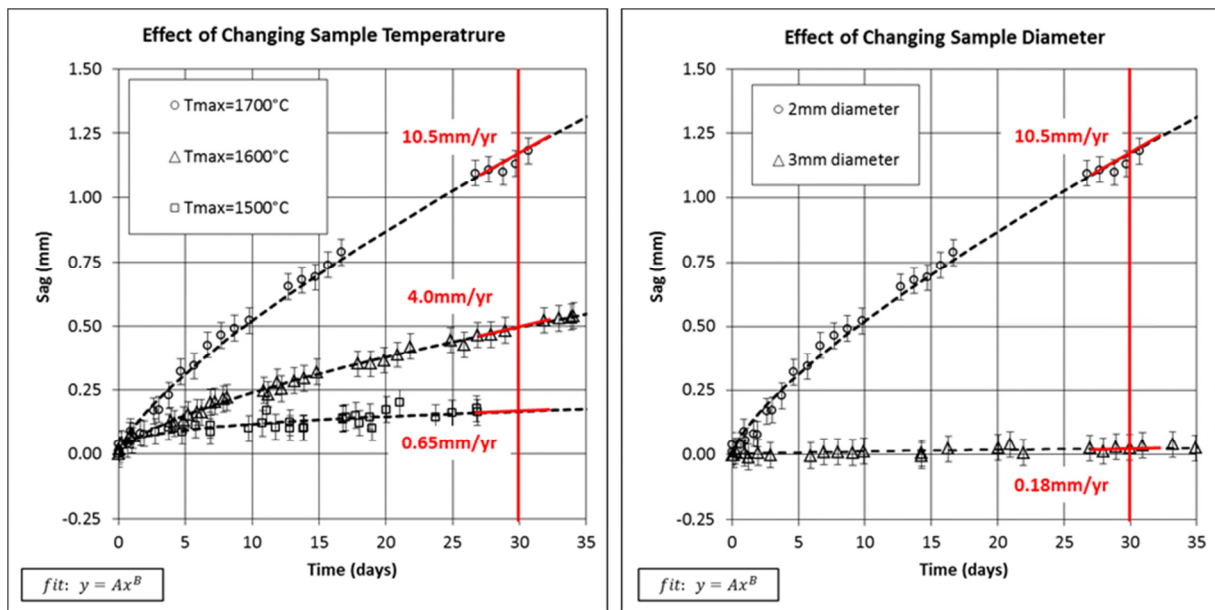


Figure 54, Sag test data for 2mm diameter samples at varying temperature (left) and for samples at Tmax=1700°C but varying diameter (right). Dashed lines indicate a power law fit.



Figure 55, Sample #1 post-heating

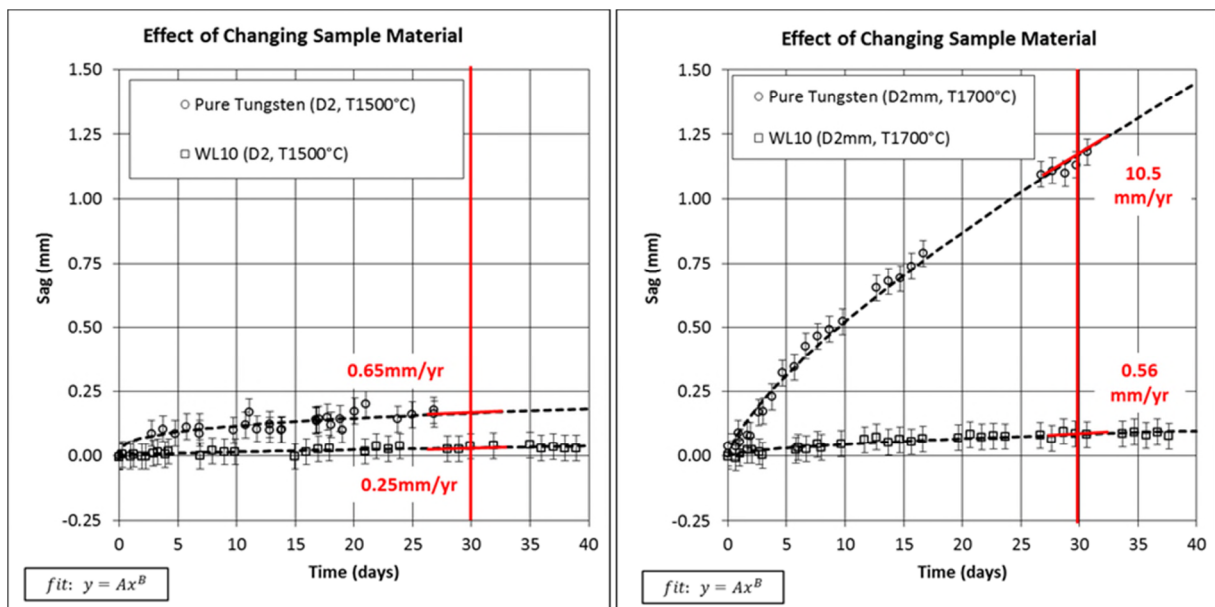


Figure 56, Sag test data comparing pure tungsten with lanthanum-oxide doped tungsten at 1500°C (left) and 1700°C (right). Dashed lines indicate a power law fit.

A summary of test cases and results, including the power law fit parameters, is included in Table 7.

Table 7, Summary of sag test results by sample

Sample #	Material	Diameter (mm)	Centre Bending Stress (MPa)	Peak Temp. (°C)	Fit Constant 'A'	Fit Constant 'B'	Sag on Day 30 (mm)	Creep Rate on Day 30 (mm/yr)
1	W	2	0.97	1700	0.0954	0.737	1.17	10.5
2	W	2	0.97	1500	0.0557	0.322	0.17	0.65
3	W	2	0.97	1600	0.0524	0.660	0.49	3.97
4	W	3	0.64	1700	0.0026	0.573	0.02	0.18
5	W	4	0.48	1700	0.0026	0.640	0.02	0.13
6	WL-10	2	0.97	1700	0.0128	0.552	0.08	0.56
7	WL-10	2	0.97	1500	0.0032	0.668	0.03	0.25
<i>Mu2e Target *</i>		6.3	0.76	1700	<i>* Values included for reference</i>			

### 3.3.4 Discussion

A diagram showing the typical staged evolution of a creep failure is shown in Figure 57. We note that our tests were generally confined to the primary creep stage where the observed creep rate was reducing with time. Our tests generally did not run for long enough to get a good measure of the steady-state secondary creep rate. For this reason the creep rate at 30 days of testing is stated in the results as this is our “best estimate” from the available data of what the ongoing creep rate might be.

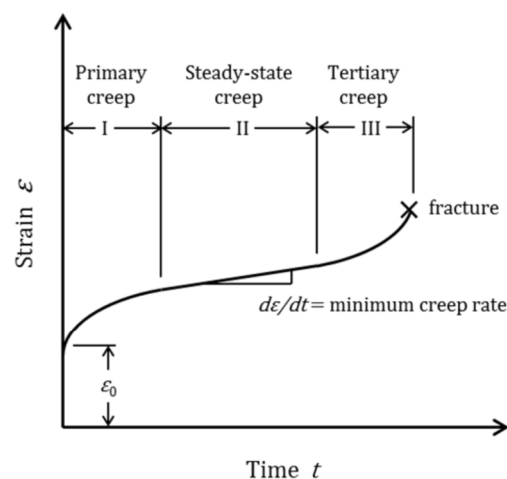


Figure 57, The phased evolution of creep

Some samples tested showed alarmingly high levels of creep, for example sample #1 which displayed a permanent deformation of more than 1mm after 30 days. However, the following are reasons to be optimistic that an acceptable solution can be found.

- i) A reduction in the test temperature from 1700°C to 1500°C (see samples #1 and #2) results in an order of magnitude reduction in the observed creep rate at 30 days. We believe that a target temperature of 1500°C or less could be achieved by adding emissivity enhancing fins to the target surface, such as those described in section 4.2 of this report.
- ii) Even at 1700°C, minimal creep was observed if the sample diameter was increased from 2mm to 3mm (see samples #1 and #4). The self-weight bending stress calculated in the 3mm sample (assuming end rotations prevented) is 0.64MPa. A Mu2e target with a self-weight bending stress of less than 0.64 MPa (assuming ends are free to rotate) could be achieved by increasing the nominal target diameter from 6.35mm to 8mm.

The lanthanum oxide doped material exhibited a much reduced rate of creep when compared to the equivalent pure tungsten samples. The thermal conductivity of 16 mm diameter WL10 rod has been measured as being c.5% lower value than pure tungsten [14], slightly reducing thermal conduction to the ends and increasing the maximum temperature, however this will be a small effect. It is believed that a doped tungsten target could be implemented with minimal impact on particle production efficiency (i.e. physics performance) or other mechanical or thermal performance. We must state here that there are some aspects of the expected Mu2e target operating condition that are not captured by the present test and may result in a greater rate of creep. These include

- i) Radiation Enhanced Diffusion (RED) leading to enhanced creep is a well known radiation damage effect. Radiation damage in the Mu2e target generated by the proton beam bombardment is expected to lead to enhanced creep rates in the target compared to the test where heating was via a DC electric current. Other relevant radiation damage effects are discussed in Section 3.6.
- ii) Creep/fatigue interaction. It is possible that the pulsed nature of the Mu2e beam heating will lead to enhanced creep deformation rates when compared to the steady DC heating used in the test.
- iii) The target bicycle wheel support. The spoke arrangement in the Mu2e target support structure will likely apply a level of longitudinal compression in the target rod that could lead to enhanced deflection. This was not captured in the test.

### 3.3.5 Recommendations

Creep is identified to be one of the factors that may limit the lifetime of the radiation cooled tungsten target for Mu2e. Due to the various ‘known unknowns’ at this stage, we would propose to take whatever opportunities exist to increase the Safety Factor in the design.

We recommend to adopt the “anti-sag” lanthanum-oxide doped tungsten as the baseline target material choice. This would appear to have minimal impact on other aspects of the target system design and is readily available.

A heating test of a full-scale prototype target with realistic support should be performed, with the option to optimise the spoke preload should issues arise, or to change the cantilever spring geometry to reduce the angle of the spokes and consequently reduce the longitudinal compressive stress.

We recommend to keep open the possibility to implement one or more of the following mitigating strategies in the event that unacceptable levels of creep deformation are encountered during offline testing or initial beam runs.

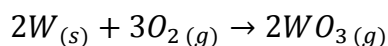
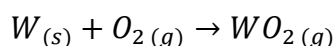
- i) Emissivity enhancing fins on the target surface to reduce the operating temperature. If the fins are orientated longitudinally then they may also offer enhanced bending strength and stiffness.
- ii) Modify the target geometry, e.g. larger diameter or tapered target rod to reduce self-weight bending stress.
- iii) A low-stress support achieved by reducing the unsupported length of the target rod or changing the target bicycle wheel structure to reduce or eliminate the longitudinal compression of the target rod.
- iv) Reduced beam power operation to lower the target temperature.
- v) Adopt helium cooling to eliminate all issues relating to high temperature operation.

### 3.4. High Temperature Chemistry

We have previously reported on the issue of high temperature chemistry and the expected implications for the target [4] [5] [6]. For completeness a short summary is included here.

Residual oxygen and water vapour in the target vacuum environment, together with gaseous contaminants from outgassing or leaks may react with the hot target material. The expected high temperature chemical reactions of tungsten with oxygen and water vapour result in the formation of oxides that have a high vapour pressure and are easily vaporised and dispersed. This vaporisation removes the oxide scale that appears on the tungsten surface as soon as it forms leaving behind a fresh metallic surface for continued oxidation and vaporisation. Since a protective oxide film is not formed, what occurs is a continual process of oxidation and vaporisation until the gas phase is starved of contaminants, the tungsten temperature is reduced below the vaporisation threshold, or the tungsten is consumed.

In the case of residual oxygen gas the following oxidising reactions may occur:



The oxide that is lost from the hot tungsten target surface will tend to plate-out on nearby cooler surfaces as a yellow-coloured film. In a perfectly sealed system this process is self-limiting as the residual molecular oxygen is progressively “burned-up” until none remains. However in any real system that is subject to leaks the residual oxygen may be continuously replenished, and thus the reaction is able to continue indefinitely.

The oxidation by water vapour is more complex. Where water vapour is present it may initiate a continuous transport of tungsten molecules from the hot tungsten surface to any nearby cooler surrounding surfaces. This process, known as the “water vapour cycle”, is described in Figure 58. To begin with the water dissociates at the hot tungsten into oxygen and hydrogen. The free oxygen then reacts with the hot tungsten to form a volatile oxide that boils off and deposits on nearby cooler walls as a film. The oxide is then reduced by the

hydrogen which was freed when the water decomposed. Effectively, the hydrogen takes the oxygen back from the tungsten, producing water again. In this way the process is able to repeat indefinitely.

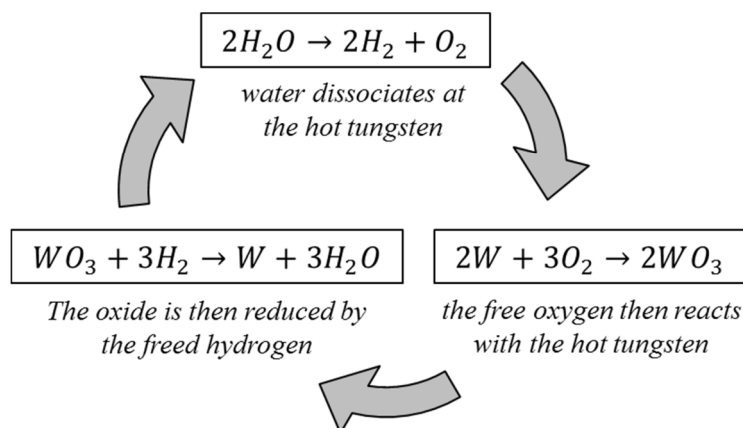


Figure 58, The water vapour cycle

As part of the Mu2e target development programme a test was performed to evaluate the chemical erosion rate of tungsten under representative Mu2e target conditions [6]. In this test 0.5mm diameter tungsten wires were heated to a specified temperature in low pressure air and the progressive reduction in diameter of the wire was monitored at intervals using a calibrated micrometer. The measurements taken on three such test wires is shown in Figure 59. The first thing we can observe is that the chemical erosion rate depends strongly on both temperature and pressure. A reduction in temperature from 1700°C to 1300°C (solid circles vs solid triangles in Figure 59) resulted in roughly a factor of two reduction in erosion rate. The pressure dependency is summarised in Table 8. At  $10^{-4}$  Torr the measured erosion rate was about 2mm/yr. At  $10^{-5}$  Torr this reduced to about 0.1mm/yr. At  $10^{-6}$  Torr the erosion rate was too small to be measured in a sensible time frame. Relating this to the Mu2e target we can say that a vacuum level of  $10^{-6}$  Torr in the target environment will be sufficient to eliminate altogether the risk posed by high temperature chemistry. Oxidation erosion can be expected to become apparent at a vacuum level of the order  $10^{-5}$  Torr, and will become very severe at  $10^{-4}$  Torr. We understand that the Mu2e vacuum group expect to achieve a minimum  $10^{-5}$  Torr vacuum in the vicinity of the target.

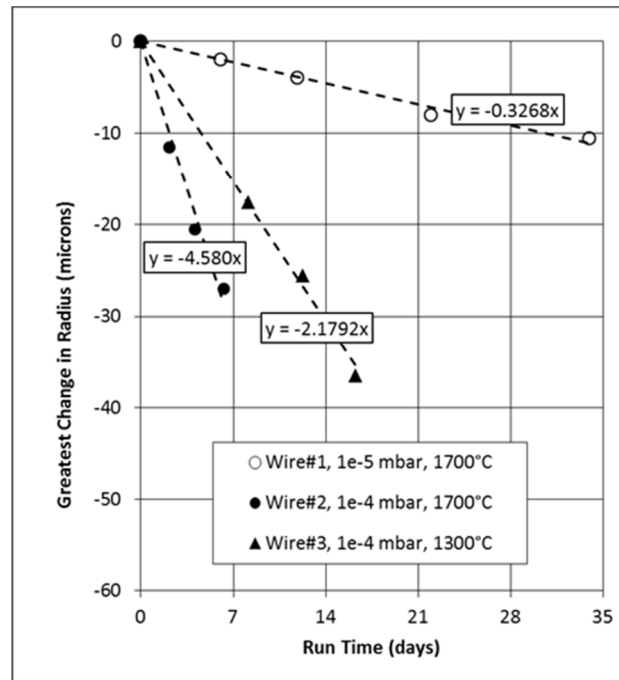


Figure 59, Oxidation test data

Table 8, Pressure and temperature dependency in the oxidation tests

Total Pressure (Torr)	Recession Rate at 1700°C (mm/yr)	Recession Rate at 1300°C (mm/yr)
$1 \times 10^{-6}$	Few microns?	
$1 \times 10^{-5}$	0.12	
$1 \times 10^{-4}$	1.8	0.9

Figure 60 is included as a comparison of the RAL oxidation measurements with data in the literature. The RAL measurements (shown in red) fall into the expected range bounded by fitting/extrapolation from the two available data sets.

When the target operates in practice the actual level of chemical erosion will be a function of the operating beam power (to which the target temperature is closely related) and vacuum pressure. We can estimate the level of erosion  $\Delta r$  by assuming an equation of the form

$$\Delta r = A \cdot B \cdot t$$

Where A is a dimensionless temperature factor, B is a rate factor with units mm/year and t is the operating time in years. To account for the factor of two reduction in erosion rate between 1700°C and 1300°C (Figure 59) and what we know about the target temperature as a function of beam power (Figure 94) we can say approximately

$$A = 0.116Q + 0.107$$

Where  $Q$  is the beam power (in kW). From a power-law fit to the rate data in Table 8 we obtain

$$B = 91100P^{1.176}$$

Where  $P$  is the pressure (in Torr). The target erosion  $\Delta r$  (in mm) for a given beam power  $Q$  (in kW) and operating time  $t$  (in hours) is then

$$\Delta r = (1.206Q + 1.113)P^{1.176} \cdot t$$

This is valid for the range, say, 3 – 8 kW and for pressures below  $10^{-4}$  Torr. Use of this formula allows the cumulative target erosion to be estimated providing that the beam power and vacuum pressure are logged at regular intervals during operation.

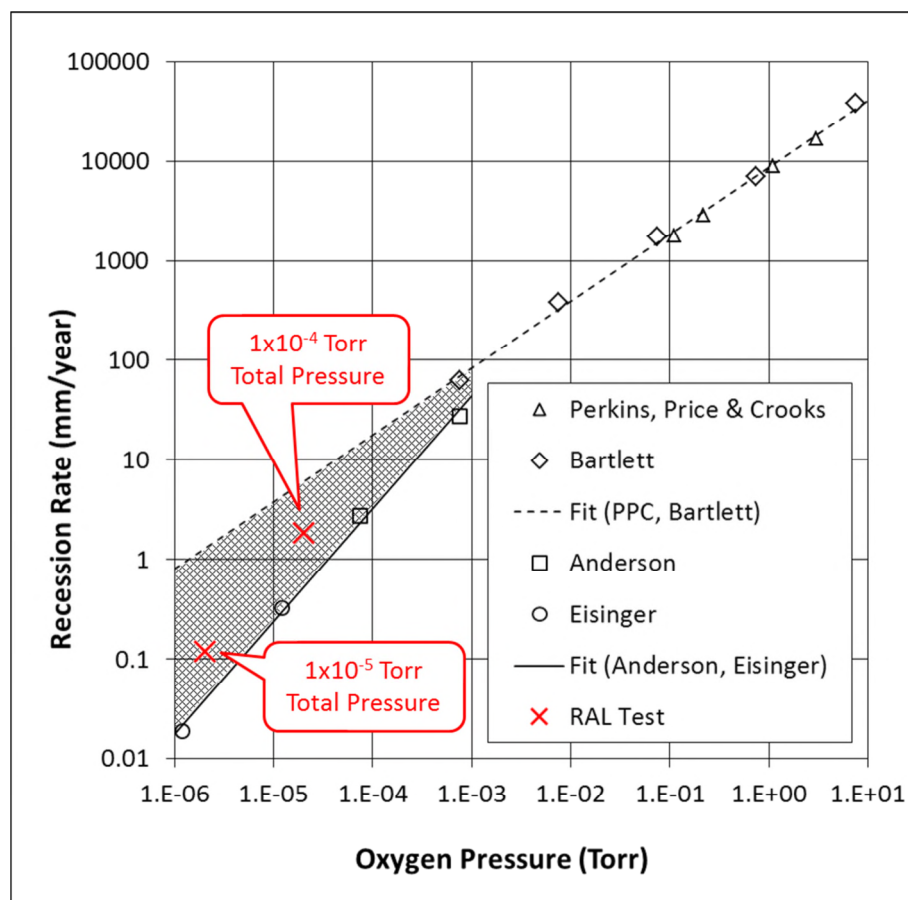


Figure 60, RAL oxidation measurements compared to literature data

### 3.5. Target Material Loss by Evaporation

At high temperature and low pressure a solid material can be “eroded” directly by evaporation. This mechanism has the potential to result in mass loss from the hot tungsten target. In a perfect vacuum the maximum molar flux of a substance from the condensed form to its gaseous form at a given temperature is expressed by the Hertz-Knudsen equation [15]

$$\dot{n}_{max} = \frac{P_v(t)}{\sqrt{2\pi MRT}} \quad [\text{mol} \cdot \text{m}^{-2} \text{s}^{-1}]$$

where  $P_v$  [Pa] is the standard vapour pressure of the substance ( $P_v$  is a function of temperature),  $M$  [kg/mol] is the molar mass of the substance,  $R = 8.31451$  [J/mol.K] is the gas constant and  $T$  [K] is the temperature. A sticking coefficient  $\alpha$  [no units] may be introduced to account for the possible reflection of vapour molecules as they impinge the condensed phase surface.  $\alpha$  is dimensionless, lies in the range  $0 < \alpha < 1$ , and must be determined experimentally.

$$\dot{n} = \frac{\alpha P_v(T)}{\sqrt{2\pi MRT}} \quad [\text{mol} \cdot \text{m}^{-2} \text{s}^{-1}]$$

However, for the purpose of this calculation we will assume the worst case evaporation rate where  $\alpha = 1$ . To get the mass flux we multiply by the molar mass of the substance

$$\dot{m} = \alpha P_v(T) \sqrt{\frac{M}{2\pi RT}} \quad [\text{kg} \cdot \text{m}^{-2} \text{s}^{-1}]$$

To get the surface recession velocity  $v$  [m/s] we divide by the density of the substance  $\rho$  [kg/m<sup>3</sup>]

$$v = \frac{\alpha P_v(T)}{\rho} \sqrt{\frac{M}{2\pi RT}} \quad [\text{m} \cdot \text{s}^{-1}]$$

Figure 61 shows the vapour pressure as a function of temperature for a number of selected elements [16] [17] [18]. Inputting this data we obtain the maximum possible evaporation recession rate as a function of temperature as shown in Figure 62. For reference the material data used in the calculation is listed in the Table 9.

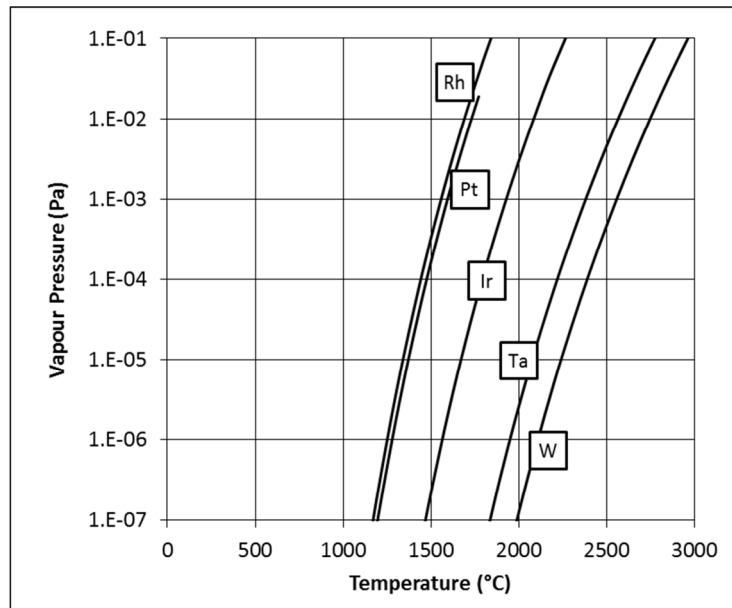


Figure 61, Vapour pressure as a function of temperature for tungsten, tantalum, iridium platinum and rhodium

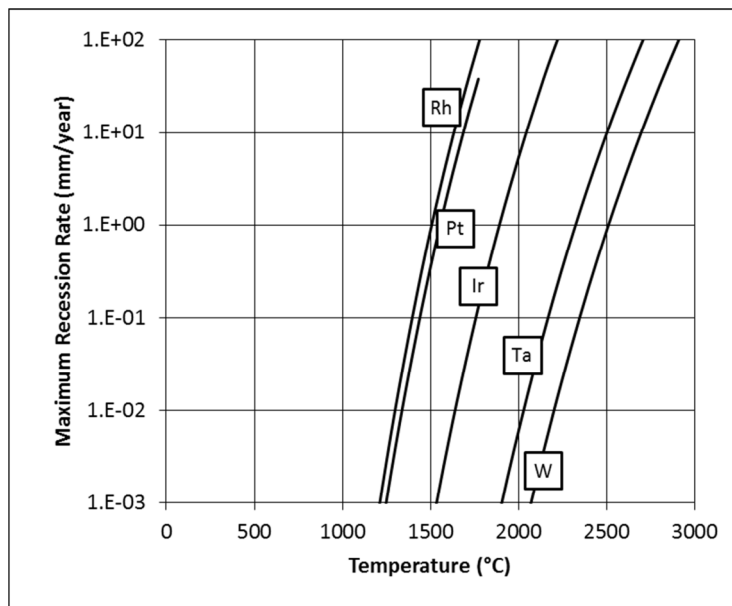


Figure 62, Maximum vaporisation recession rate as a function of temperature for tungsten, tantalum, iridium platinum and rhodium

**Table 9, Selected material data for tungsten, tantalum, iridium platinum and rhodium**

Material	Density $\rho$ [kg/m <sup>3</sup> ]	Molar Mass $M$ [kg/mol]	Vapour Pressure P in [Pa], T in [K]	Melting Temperature [°C]
Tungsten [2]	19,250	0.184	$\log_{10}P = 12.933 - 45087/T$	3410
Tantalum [3]	16,690	0.181	$\log_{10}P = 12.450 - 41000/T$	2996
Iridium [4]	22,560	0.192	$\log_{10}P = 12.1449 - 33337/T$	2410
Rhodium [4]	12,410	0.103	$\log_{10}P = 11.8996 - 27276/T$	1965
Platinum [4]	21,450	0.195	$\log_{10}P = 11.7669 - 27575/T$	1772

Interrogating Figure 62 we can clearly see that tungsten has the lowest calculated recession rate out of the materials in question. At the expected Mu2e target operating temperature of around 1700°C the maximum annual vaporisation recession rate for tungsten is less than 1 µm/year, a vanishingly small amount. However, at the same temperature the maximum recession rate for iridium is much greater, of the order 0.1mm/year. This could become an issue for any thin iridium protective coating considered (see section 4.1 of this report).

### 3.6. Radiation Damage Effects

#### 3.6.1 Overview

Tungsten and tungsten-based alloys are the main candidates for plasma-facing components in future magnetic confinement fusion reactors e.g. DEMO where they will be exposed to temperatures of up to 1200°C and a large flux of neutrons and energetic ions. Consequently there is an active materials science research programme in this area which is a valuable source of reference for the Mu2e project. Experts in the field have been consulted via the RaDIATE collaboration [19] starting with an unpublished literature review by the UK's National Nuclear Laboratory commissioned by Fermilab [20] which is available for private study and is recommended for further reading and as a source of references. A short summary of the key findings is included in the sub-sections below.

Radiation damage effects on the material microstructure that are of concern to us include matrix damage by defect clusters and loops, void swelling and the formation of a void lattice [20]. Other effects on material properties are caused by radiation enhanced diffusion and the generation by transmutation of gases and soluble and insoluble products. These effects, individually and in combination, can lead to swelling, degradation of thermal conductivity, radiation enhanced creep, grain-boundary segregation, hardening, radiation embrittlement and radiation-enhanced corrosion all of which will serve to reduce the lifetime of Mu2e targets further than that revealed in the non-irradiated material test program described in this report.

Displacements per atom (dpa) is often used as a key indicator in radiation damage studies. The calculated radiation damage level of around 260 dpa per year for the Mu2e target is around 100 times greater than that calculated for the DEMO reactor and the irradiation temperature, another key factor, is also considerably higher so the combined effects are of concern but difficult to quantify. For example, an irradiation temperature of 800°C has been found to reduce void and loop number densities but coarsen the void and loop radii [21].

Figure 63, reproduced from the work of Ullmaier and Carsughi [22], indicates the temperature range at which the expected key irradiation damage effects occur, where  $T_m$  refers to the melting temperature of the target material. For tungsten at the expected elevated Mu2e operating temperature helium embrittlement and void swelling may be the dominant damage mechanisms.

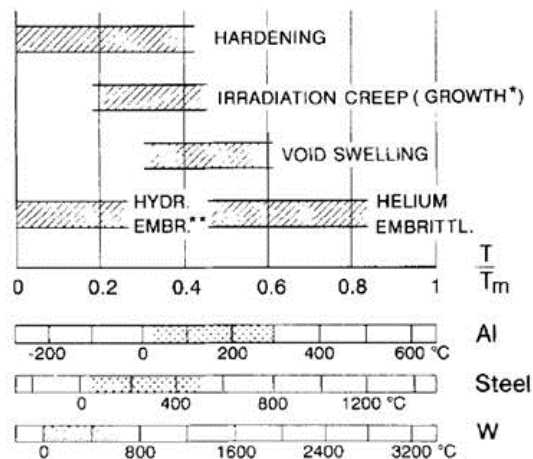


Figure 63, Approximate range of temperatures where the radiation effects occur [22]

For reference, FLUKA calculations of the generation of transmutants of interest for Mu2e are listed in Table 10.

Table 10, Generation of transmutants of interest for Mu2e

Avagadro Constant	6.02+E23	atoms/mol
Mass of tungsten target	87	grams
Number of mols of tungsten	0.473	mols
Number of tungsten atoms in target	2.85E+23	atoms
Protons/year on target at 8kW	1.97E+20	Protons/year

RESIDUAL NUCLEI	NUCLEI/PROTON	NUCLEI/YEAR	ATOMIC PPM/YEAR
protium	2.17	4.27E+20	1501
deuterium	0.6	1.18E+20	415
tritium	0.37	7.29E+19	256
helium 3	0.05	9.85E+18	34.6
helium	1.87	3.68E+20	1294
lithium 6	0.028	5.54E+18	19.4
potassium	0.000075	1.48E+16	0.0519
potassium 41	0.00055	1.08E+17	0.381
tantalum 182	0.013	2.56E+18	8.99
rhenium	0.00029	5.71E+16	0.201

### 3.6.2 Comparison with ISIS tungsten spallation neutron targets

At RAL, we have additional experience from the operation of the ISIS tungsten spallation neutron targets [23] [24]. Relative conditions can be compared in terms of the operating

temperature, stress, displacements per atom, helium, hydrogen and other transmutant impurity generation. Relative parameters for Mu2e and ISIS targets are listed in Table 11.

Although the beam spot size proposed for Mu2e is much smaller than in the beams generated at ISIS, the expected peak fluence is roughly the same magnitude due to the compensating difference in beam current, i.e, for a Gaussian beam the peak proton fluence  $f_{peak}$  (in  $\mu\text{A}/\text{cm}^2$ ) on the target front face may be calculated from

$$f_{peak} = \frac{I}{2\pi\sigma^2}$$

Where  $I$  is the beam current (in  $\mu\text{A}$ ) and  $\sigma$  is the Gaussian beam sigma (in cm).

The peak lifetime displacements per atom for the Mu2e target is roughly double that of the target installed at the ISIS 1st target station (TS1). This is despite the (longer) five year design life of the ISIS target compared to 1 year for Mu2e. The estimated peak gas production rate in the Mu2e tungsten is much greater than that experienced in the ISIS targets.

**Table 11, Comparative parameters for ISIS and Mu2e targets**

	ISIS TS1	ISIS TS2	Mu2e
Beam kinetic energy (GeV)	0.8	0.8	8
Average beam current ( $\mu\text{A}$ )	200	40	1
Average beam power (kW)	160	32	8
Target design life (years)	5	5	1
Beam shape	Gaussian	Gaussian	Gaussian
Beam sigma (cm)	1.6	0.6	0.1
Peak fluence on target front face ( $\mu\text{A}/\text{cm}^2$ )	12	18	15
Peak lifetime accumulated dpa *	135		260
Helium Gas Production (appm/dpa) *	10		20
Peak operating temperature in tungsten ( $^{\circ}\text{C}$ )	200	250	1700
Cyclic temperature rise in tungsten ( $^{\circ}\text{C}$ )	3	25	48
Peak thermal stress in tungsten (MPa)	90	160	16
Cyclic thermal stress amplitude in tungsten (MPa)	2	18	12

\* Brian Hartsell mars calculation for the RADIATE collaboration, [www.radiate.fnal.gov](http://www.radiate.fnal.gov)

A key difference making it difficult to make meaningful comparisons between the ISIS and proposed Mu2e target is the operating temperature. ISIS targets are water cooled and limited to a peak temperature in the tungsten target material of around  $250^{\circ}\text{C}$ . It is possible that the elevated temperature expected in the Mu2e target could be beneficial in annealing out radiation induced hardening effects and allowing gas products to diffuse out through the material. Conversely, it is equally possible that the density of such defects may become

concentrated, for example at grain boundaries leading to enhanced degradation of key thermomechanical properties.

### 3.6.3 Void swelling

Void swelling in tungsten is reported by Leonard [25] for around 10 dpa to be a maximum of 2% at 1100 K and to reduce to around a tenth of this value at 1800 K as shown in Figure 64. Similar results are reported in the ITER Materials Assessment Report [26]. However, since the irradiation rate for Mu2e is almost two orders of magnitude greater than in the reported experiments, the swelling/irradiation temperature curve will be shifted to higher temperatures thus increasing the prospective swelling for Mu2e.

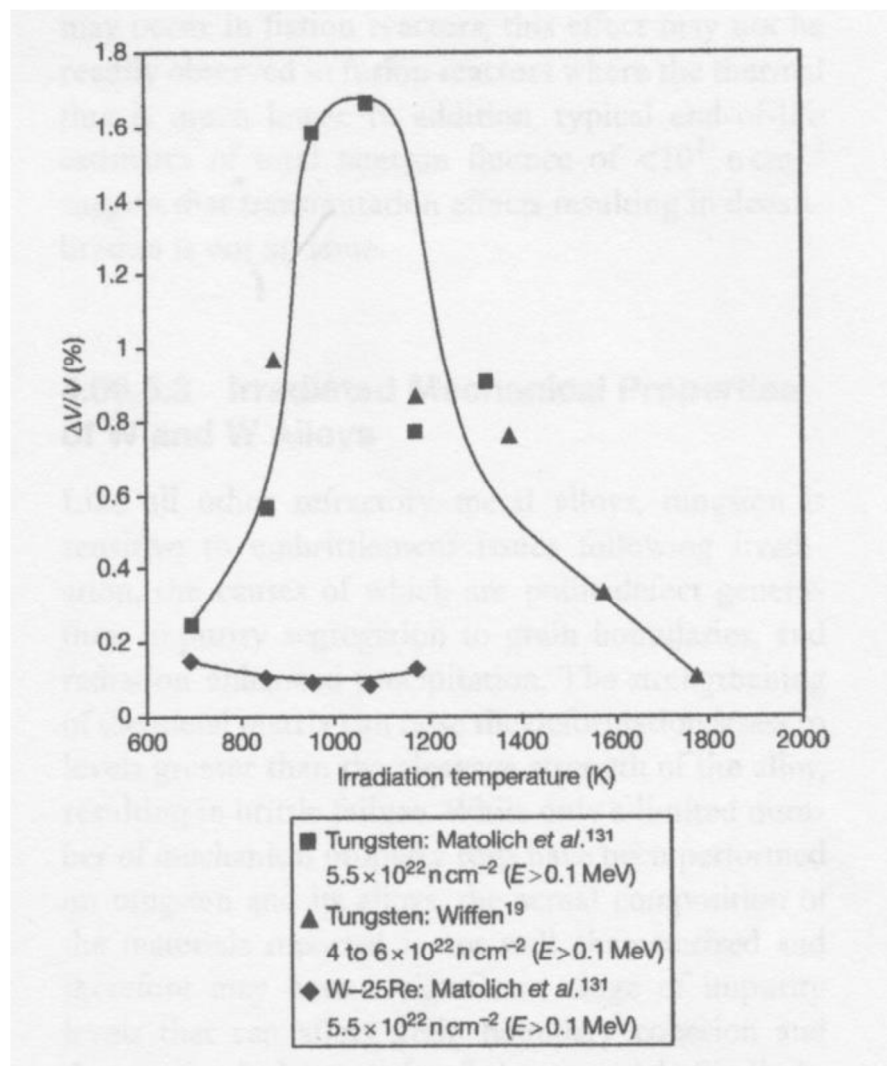


Figure 64, Immersion density measurements of the irradiation temperature dependence of void swelling in W and W-25%Re exposed to c. 10 dpa [25]

### 3.6.4 Thermal conductivity

A damage level of only 0.6 dpa has been reported to reduce the room temperature thermal conductivity in tungsten by 25% [27]. However at the high operating temperature of the Mu2e target, point defects would be expected to be highly mobile thereby recombining and recovering the thermal conductivity to some extent.

### ***3.6.5 Effects of gas generation***

A complicating issue is the high production rate of helium and hydrogen isotopes. At the high operating temperature, the hydrogen isotopes may be expected to migrate to the surface and effuse out. However, due to the high level of cascade damage, the gases could agglomerate in vacancies and be trapped, simultaneously preventing the recombination of point defects (Frenkel pairs). It is reported [28] that due to this effect there can be expected to be a vacancy (and related interstitial) for each helium atom generated. Thus, significant reductions in thermal conductivity (and fracture toughness) are still to be expected even at the high operating temperature. This effect would also go some way towards explaining the previously mentioned void swelling and helium embrittlement reported by Ullmair and Carsughi [22] as being the dominant effects to be expected at the Mu2e target operating temperature.

### ***3.6.6 Effects of solid transmutation production***

The production rate of non-gaseous transmutants is relatively low when compared with the gaseous products. A production rate of 150 appm pa for all tantalum isotopes is not expected to contribute appreciably e.g. to hardening. A production rate of c.60 appm pa for all lithium isotopes ( $Z=6,7,8$ ) is also a low number. Although the small atoms are expected to migrate quickly to grain boundaries, consultations with materials scientists have not revealed any known deleterious effects from Li impurities in tungsten. It is however possible that tightly bound complexes consisting of transmuted atoms and point defects could be formed which might either pin dislocations and/or inhibit their migration [20].

### ***3.6.7 Radiation hardening***

Radiation hardening of tungsten is reported at relatively low irradiation doses and temperatures from a number of sources [20]. Hardening appears to follow a square root of dose dependence. There has been no systematic examination of the influence of irradiation temperature on hardening and embrittlement. Although one might imagine that the high mobility of point defects at high temperatures would ‘anneal’ the effects of radiation hardening (as for thermal conductivity), in data that exists there is no clear trend with increasing irradiation temperature. Radiation induced *ductilisation* of tungsten has been reported by Kurushita [29] at around 0.5 dpa and up to temperatures of 1700°C by using 1% TiC as a defect sink at grain boundaries. He proposes TaC [30] as a more thermally stable alternative to the TiC but neither material is commercially available at present and the effectiveness at higher dose rates is unknown.

If the  $\text{La}_2\text{O}_3$  doped material is selected in order to reduce creep, Rieth et al [14] show the oxide forms in needles (WL10) or flakes (WL10opt) which are presumably formed between tungsten grain boundaries since a transgranular failure mode is reported at temperatures up to 1000°C. It seems likely that such a structure would be reasonably resilient to radiation damage but no data is known on this.

### ***3.6.8 Increases to the ductile-to-brittle transition temperature***

Dramatic increases in the DBTT are reported both for pure tungsten and alloys at relatively low levels of radiation. Krautwasser et al [31] report an increase in DBTT from c.350K to c.1150K at a dose of about 1 dpa. Consequently, notwithstanding the high operating temperature of the Mu2e target, we can expect the ends of the target to be brittle even while the beam is running, and any material that may retain some ductility while running will be

cycled across the ductile-to-brittle transition every beam trip, and every beam spill for some material.

### ***3.6.9 Fracture toughness***

For unirradiated material, below 600°C various grades of tungsten exhibit low toughness (4 - 20 MPa m<sup>1/2</sup>) but above this becomes more ductile. Over the range of 600 – 800°C pure W and W-1%La<sub>2</sub>O<sub>3</sub> exhibit fracture toughness values over 60 MPa m<sup>1/2</sup>. No toughness information is available at higher temperatures, nor is there any known information on radiation effects on fracture toughness. However, since we know that irradiation causes a dramatic increase in DBTT, it seems likely that there will be a related reduction in the fracture toughness at elevated temperatures compared with the non-irradiated material.

### ***3.6.10 Irradiation creep and stress relaxation***

Creep is a critical design constraint for the Mu2e target as described above. The only known measurements of irradiation creep are attributed to Hesketh [32] in 1967 for a loaded tungsten spring at 43°C exposed to a total of only c.0.01 dpa of fission neutrons. After the 30 days of irradiation, steady-state creep was observed with a total strain of around 3×10<sup>-4</sup>. This is approximately the same rate as is acceptable for the Mu2e target to have a useful lifetime of 1 year. Unfortunately the stress level in the spring is not known at this stage and requires access to the original source.

Related to irradiation creep, a measurement of stress relaxation in a thin tungsten film at room temperature has been reported [33] by exposure to 400 keV P ions at up to around 0.6 dpa. A stress relaxation of 90% was reported from the original value of 260 MPa.

We cannot usefully extrapolate these single results for irradiation creep and stress relaxation at low temperatures and low dose levels to the high dose rate and high temperatures pertaining to Mu2e. However, when one also considers the additional creep fatigue resulting from the pulsed beam, one might expect the creep rate in the Mu2e target to be greater, and possibly considerably greater, than that predicted by the DC non-irradiated materials tests described above.

### ***3.6.11 Radiation enhanced corrosion***

Tungsten targets at LANSCE in contact with water have been reported to undergo accelerated corrosion under exposure to a proton beam [34]. Since any trace air or water vapour remaining in the Mu2e target station vacuum will be heavily ionised, it seems likely that, for a given vacuum level, the corrosion rate for the Mu2e target will be greater than that observed in the off-line experiments carried out for the project so far.

### ***3.6.12 Implications for target integrity***

The Mu2e target rod is required to have a minimum lifetime of 1 year while operating significantly above the recrystallization temperature (considered a design limit for the plasma facing components in fusion applications). It is required to maintain physical integrity without significant deformation while being subjected to a pulsed proton beam loading at a dpa rate and integrated dose that are typically 2 orders of magnitude greater than that for which data exists in the literature, and for the most part at higher temperatures. In general the

absence of high dose data covering the high irradiation level and high operating temperature of 1500-1700°C must be of concern for the Mu2e target.

The NNL report [20] summarised the major issues and desirable future work relating to radiation damage in the Mu2e target to be:

- i) 'The potential for high levels of displacement doses to raise the ductile to brittle transition temperature above the operating temperature, which will result in the irradiated regions of the target being 'brittle' at all temperatures.
- ii) 'To fully evaluate the potential embrittlement shifts of the regions adjacent to any internal defects or surface cracks quantitative fracture toughness data is required as well as an analysis of the stresses generated in the target.
- iii) 'In addition, the increases in yield stress and reduction in tensile ductility require investigation to higher doses and temperatures than those found in the literature. These data would be an important input to any stress analysis.
- iv) 'The resistance to thermal shock cannot be properly evaluated in irradiated W because of a lack of data on the effect of irradiation on thermal conductivity and thermal expansion. By analogy with the observed effect of the irradiation-produced microstructure on Be, the possible influence of the irradiated microstructure on the thermal properties of W cannot be ruled out at similar values of  $T_m$ , i.e. below  $\sim 0.4T_m$  ( $\sim 1400^\circ\text{C}$ ).
- v) 'Dimensional changes due to irradiation growth can be discounted, whereas changes due to irradiation induced bubble or void formation need further investigation at the high doses and high gas content of the application. The effect of high dose rates, typical of Mu2e, on raising the peak swelling temperature also needs to be investigated.
- vi) 'Stress relaxation and irradiation creep will tend to relax stresses set up in the irradiated region during operation. The extent of these cannot be evaluated from existing data and further data are required, particularly as these processes are commonly found to be athermal.
- vii) 'Conventional high temperature creep is of lesser importance since the highest application temperature does not exceed  $0.5T_m$  ( $\sim 1700^\circ\text{C}$ ), above this temperature such processes become important.

'Overall, in the temperature and dose regime of interest (500-1500°C at doses of up to 260 dpa/yr) the review demonstrates that there are likely to be significant effects of irradiation on the properties of W. It is considered that these are sufficient to modify the ductility, toughness and dimensions of the material along the proton beam track in the target. The irradiation-induced changes are potentially severe, for example the material along the track may become brittle at all temperatures the component experiences, or high levels of void swelling at high doses causing large compressive stresses. However, the fact that we are dealing with a region of highly irradiated material within a relatively unaffected matrix necessitates the use of modelling methods to predict integrity. To be effective these models require improved irradiation data [...]'.

Clearly, the recommended further research into degradation in thermal conductivity, irradiation hardening, fracture toughness, dimensional changes etc are far beyond the scope of the Mu2e project and it will be necessary to rely upon operating experience to guide future development if required. Nevertheless it would seem prudent to include extra safety margin where realistic, for example by increasing the target diameter to reduce bending stresses or incorporate longitudinal fins to reduce the temperature and increase stiffness.

## 4 Technical Risk Mitigation Strategies

### 4.1. Coatings

The use of a suitable oxidation resistant or high emissivity coating has the potential to extend the target service life. An extensive series of tests has been performed on two candidate coating systems, CVD silicon carbide and Sputter-coated iridium, as part of the Mu2e target development programme [6]. However, the tests reveal serious issues in both cases and as a result neither system can be recommended. A short summary is provided below.

50 micron thick silicon-carbide coatings were successfully deposited on a range of tungsten samples using a commercial chemical vapour deposition process. Our tests demonstrate that silicon carbide coatings are strong, have a high emissivity (potentially reducing the target operating temperature) and perform well in high vacuum of  $10^{-6}$  Torr or better. However, the coatings rapidly degrade when heated in a vacuum at  $10^{-4}$  Torr, and thus cannot be recommended for the Mu2e application. The issue stems from the fact that in the presence of oxygen, silicon carbide may react in one of two modes. At high temperature and low pressure a passive oxidation mode prevails where a protective oxide layer is formed limiting further attack of the underlying SiC. At low pressure and high temperature an active oxidation mode prevails where a volatile oxide is formed leading to recession of the SiC layer. The Passive/Active transition is shown in Figure 65. It happens that the expected Mu2e operating condition, indicated by the red cross, lies in the active oxidation regime. Some SEM images and chemical analysis of our coated samples post heating are shown in Figure 66.

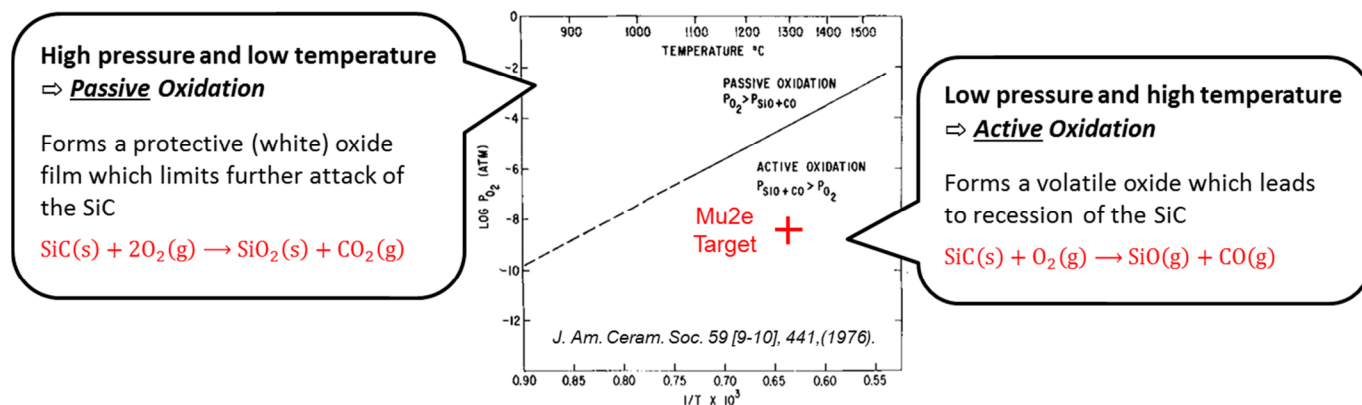
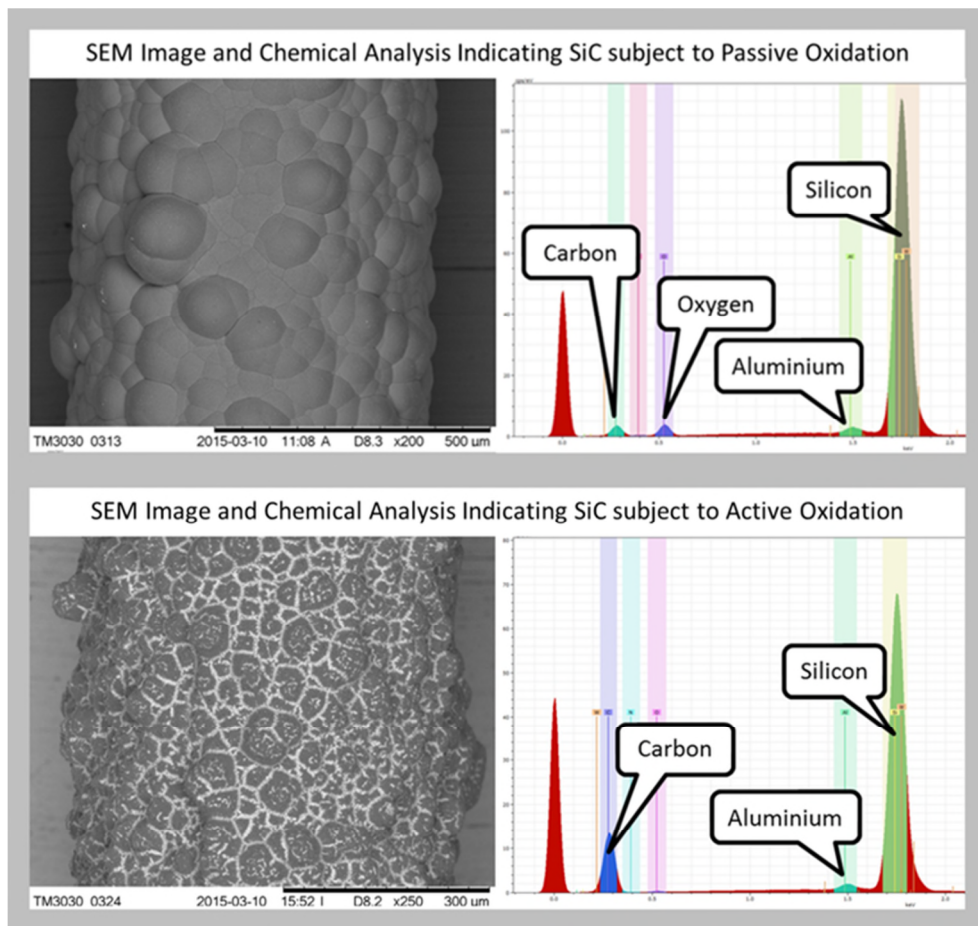


Figure 65, Passive/Active transition for oxidation of SiC



**Figure 66, SEM images of CVD Silicon carbide coatings that have undergone passive oxidation (above) and active oxidation (below) during heating tests in low pressure air**

Iridium coatings were also trialled as part of the test programme. Iridium is much less reactive than tungsten at high temperatures and has good oxidation protection potential. Iridium layers up to five microns thick were generated by sputter coating onto a rotating 0.5mm diameter tungsten substrate wire. SEM images of the resulting iridium coated tungsten wire are shown in Figure 67. The black spots in the image could be holes in the coating but this could not be confirmed.

Unfortunately, during thermal cycling tests in good vacuum (better than  $10^{-6}$  Torr) the coating was observed to peel away from the tungsten substrate indicating that the iridium layer was not well adhered to the underlying tungsten (Figure 68). This meant that follow-up oxidation resistance tests could not be performed. This failure may be in part due to a significant mismatch in thermal expansion coefficient between tungsten ( $4 \times 10^{-6}/^{\circ}\text{C}$ ) and iridium ( $7 \times 10^{-6}/^{\circ}\text{C}$ ), leading to large thermal stresses in the thin coating when the composite body is heated.

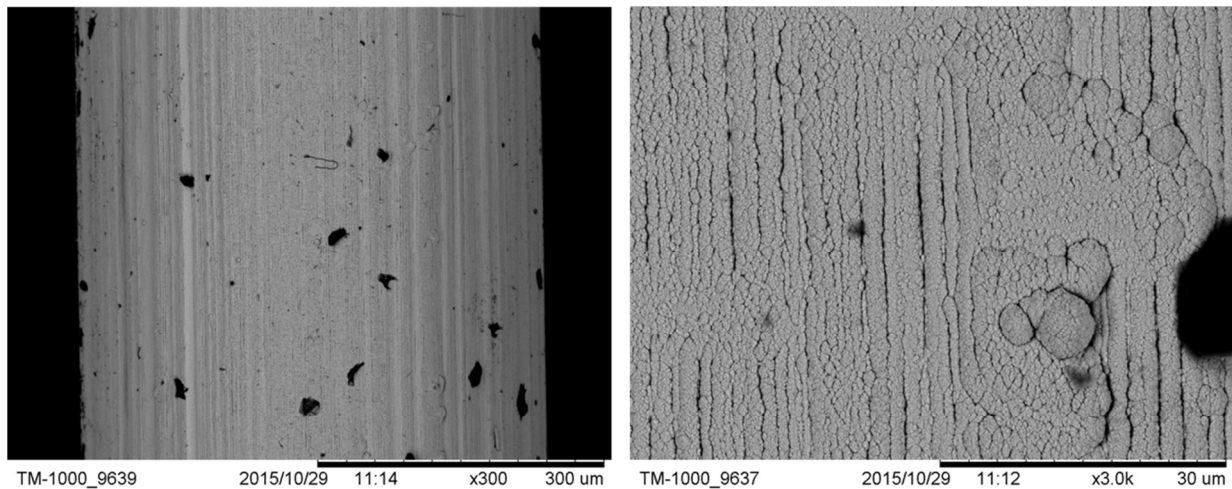


**Figure 67, SEM images of the 5 micron thick iridium coating**



**Figure 68, Failure of the iridium coating**

It is thought that much thicker iridium coatings of 100 microns or so would be needed for the Mu2e application to give some margin against the possible effects of evaporation. A chemical vapour deposition route for producing thick iridium coatings is known to be under development by the same commercial company that supplied our silicon-carbide coatings. This remains a potential route going forward and could be investigated further in the event that high-temperature chemistry is revealed as a lifetime limiting factor during prototype target heating tests or initial beam operations.

## **4.2. Fins**

There remains a possibility to reduce the equilibrium operating temperature of the target by adding a geometric surface profile that artificially enhances its emissivity.

Previously reported simulations using the FLUKA code [5] indicate that an average heating power of around 580W will be deposited in the Mu2e target rod when operating with an average beam power of 7.7 kW. ANSYS finite element heat transfer analyses presented in the same report indicate that a peak steady-state operating temperature of around 1700°C will be reached and maintained in the target rod after a few minutes of operation. These analyses assumed representative literature data for the total emissivity of smooth bare tungsten [35], reproduced in Figure 69 below. That is, a bare, smooth, tungsten target.

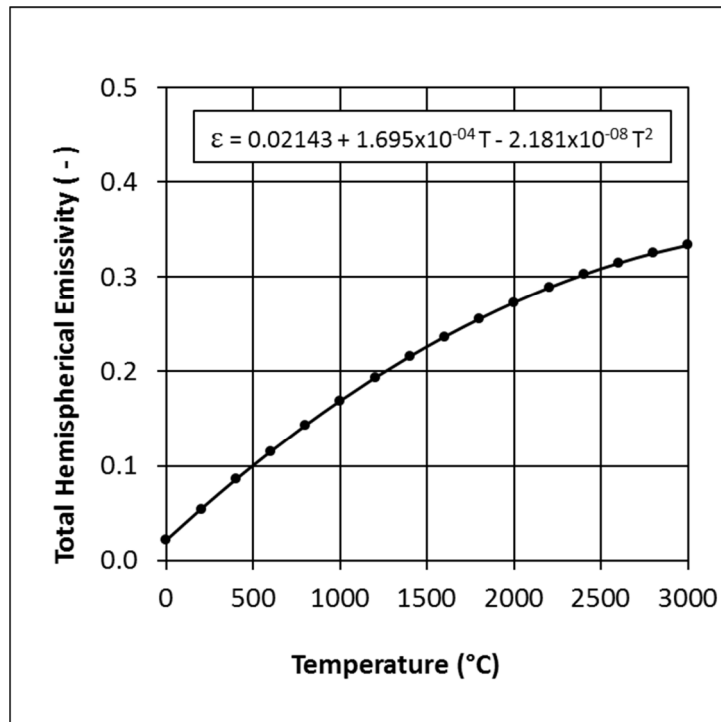
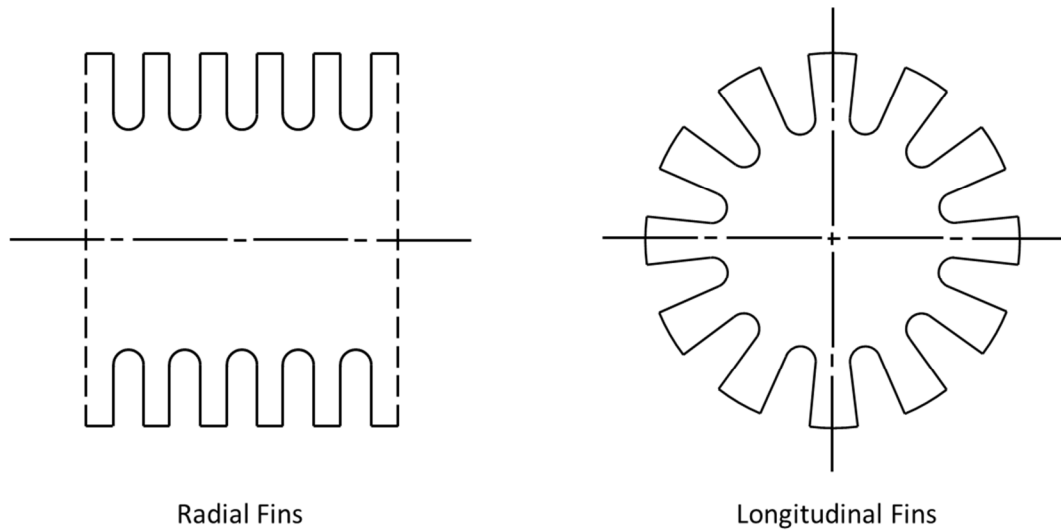


Figure 69, Literature data for total hemispherical emissivity of smooth bare tungsten as a function of temperature

The available published emissivity data for tungsten is predominantly quoted for smooth, polished surfaces as samples treated in this way permit reproducible test results to be obtained. However, it is well known that the surface roughness of a sample will effect it's emissivity, with rougher surfaces providing a geometric “emissivity enhancement” [36]. Indeed, measurements made as part of the present test and development programme confirm that rougher “engineering” surfaces lead to higher emissivity values [5] [6]. The natural extension from this finding is to devise an artificial emissivity enhancing surface profile that could be applied to the tungsten target. A fin structure is the obvious solution as the spaces between fins can be made to approximate black-body cavities that contribute to an enhanced overall average emissivity. Figure 70 indicates in concept that fins on a cylindrical target could be formed either radially or longitudinally. In either case, if the ratio depth:width of the cavity formed between fins is large then that space appears as a black body. In practice a ratio of three or more is sufficient.

Longitudinal fins have the added benefit of improving the bending stiffness of the target, potentially making it more resistant to self weight creep deformations during high temperature operation. For example, longitudinal fins of the type shown in Figure 70 will double the second moment of area of the cross-section if 1mm tall fins are added to a solid 6.3mm diameter core cylinder. This means that the bending stiffness “EI” of the resulting longitudinally finned rod is double that of a simple 6.3mm diameter cylinder. At the same time the cross-section area, and thus the self weight load, increases by only a factor 1.4.

Providing the bending stiffness increases by more than the target weight we have a net gain. We therefore suggest to investigate potential manufacturing routes to produce a suitable longitudinal finned structure as part of the next phase of target prototyping.



**Figure 70, Potential radial (left) and longitudinal (right) fin orientations**

An ANSYS finite element model (Figure 71) was used to investigate the radiation heat transfer performance of a radially finned target surface. The model represents an infinitely long cylinder with a fixed applied heating power per unit length, adjusted such that in the case of a plain tungsten cylinder the equilibrium surface temperature is 1700°C. Radial fins are then added at the surface of the cylinder and keeping the same applied heat load a new lower equilibrium temperature may be calculated. We define the effective emissivity of the surface as

$$\varepsilon_{surf} = \frac{Q}{2\pi r \sigma T^4}$$

Where Q is the applied heat per unit length [W/m], r is the outer radius [m] and T is the temperature [K]. The resulting emissivity enhancement of a ribbed surface compared to a smooth one is thus

$$Emissivity\ Enhancement\ Factor = \frac{\varepsilon_{finned}}{\varepsilon_{smooth}} = \left( \frac{T_{smooth}}{T_{finned}} \right)^4$$

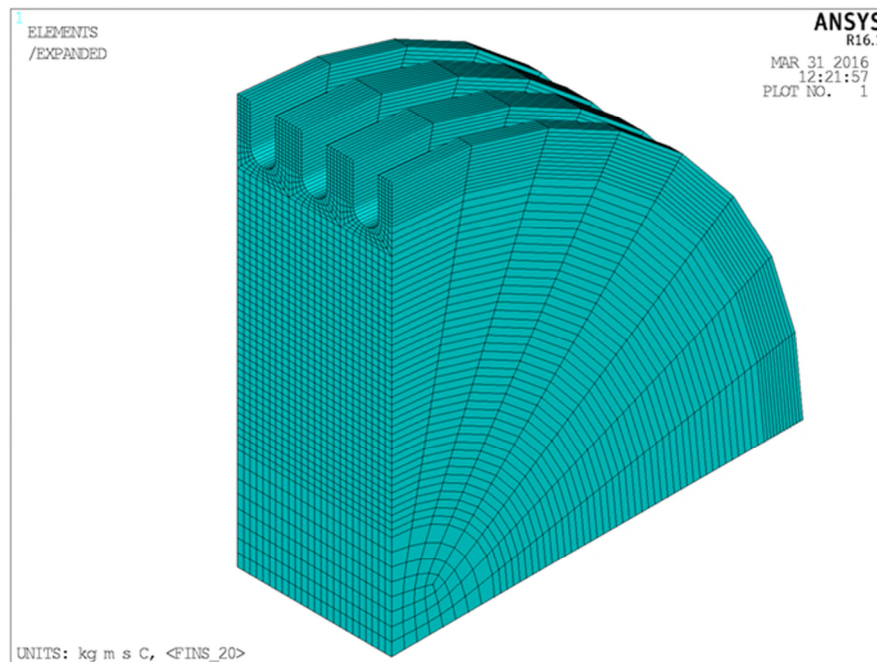


Figure 71, ANSYS finite element model of a finned surface

The results indicate that an optimum structure will have thin fins spaced apart to produce deep inter-fin cavities. By way of example Figure 72 shows the result for 0.25mm thick fins with an 8mm outside diameter on a 0.5mm pitch. It can be seen that even grooves with a modest aspect ratio of 2 are sufficient to achieve a reduction in equilibrium temperature from 1700°C to 1500°C.

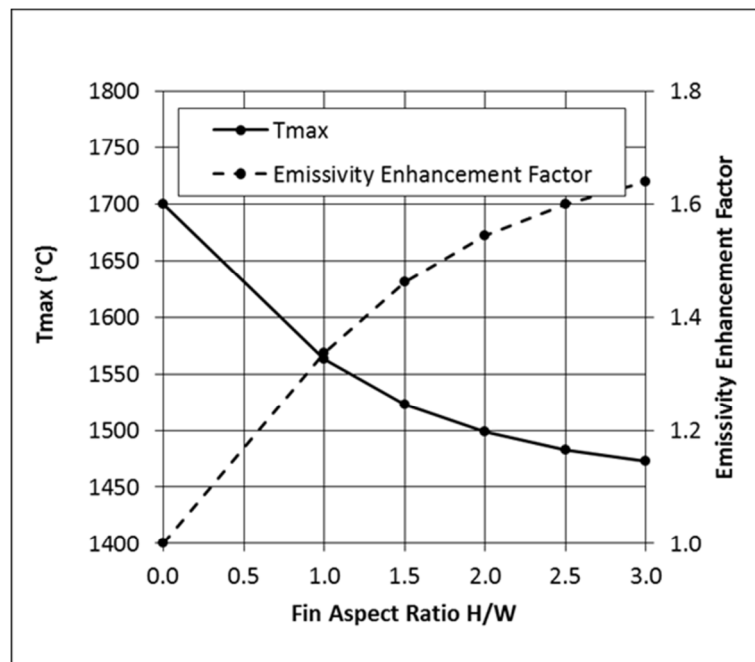
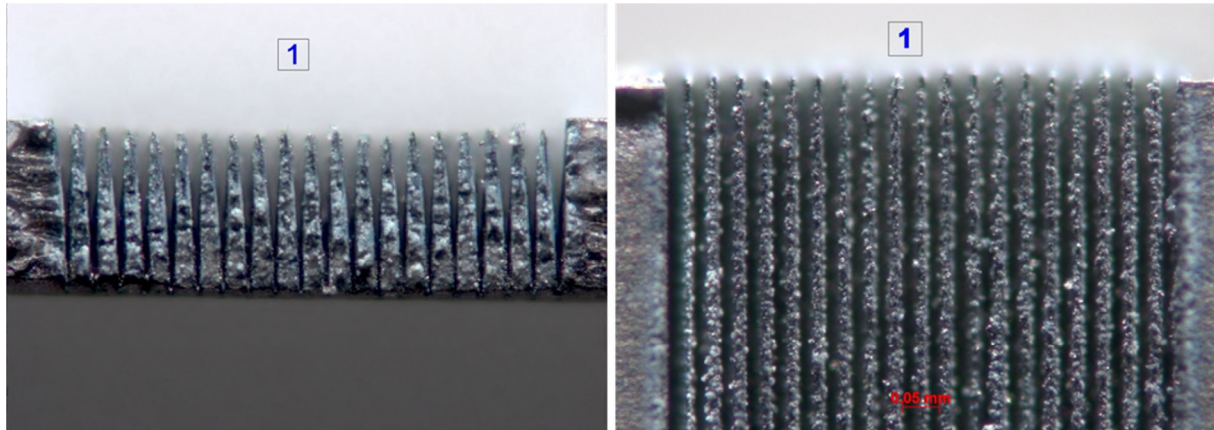


Figure 72, Results for 8mm OD radial fins on a 0.5mm pitch

As part of the present target development programme we have successfully trialled two methods for producing finned tungsten surfaces. In the 1<sup>st</sup> trial a laser machining process was used to produce high aspect ratio tapered grooves spaced apart on a pitch of about 25 microns

(Figure 73). Under thermal testing these “micro-finned” surfaces were shown to have excellent heat transfer characteristics (raised emissivity and reduced operating temperature) [9]. However, concerns over a potential negative impact on fatigue life due to the sharp crack-like geometry of the grooves meant that this surface treatment was not adopted in the target design.



**Figure 73, Section view (left) and normal view (right) of laser-machined finning on a tungsten surface**

An additional concern for fin-like surfaces is their resilience to chemical erosion (see section 3.4 of this report). That is, the fins must not be too thin. With this in mind a 2<sup>nd</sup> manufacturing trial was performed, creating larger radial fins using a wire EDM technique. Figure 74 shows a short sample where radial 1mm deep grooves have been machined into a 6mm diameter tungsten rod. The fins are 0.3mm thick and are repeated on a longitudinal pitch of 0.7mm. It is believed that fins at this larger scale may have a useful life in the expected Mu2e vacuum environment and that the smooth radius at the groove root may somewhat mitigate the fatigue life issue outlined above.

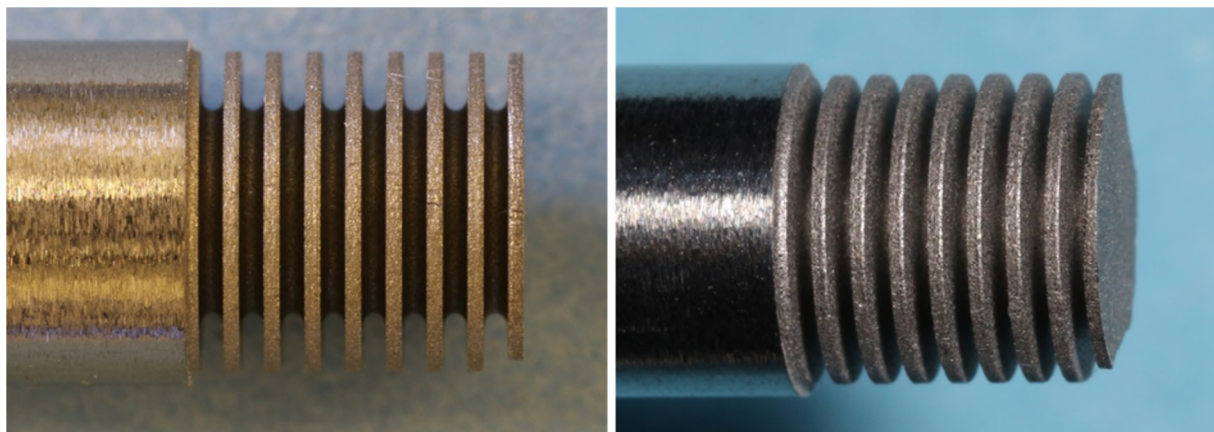


**Figure 74, 0.3mm thick fins formed in an 8mm diameter tungsten rod by Electro-Discharge-Machining (EDM)**

The physics impact of adding a layer of surface fins to the cylindrical tungsten target rod has been studied using the G4beamline code [37]. The results (Figure 75) suggest that a loss of around 4% in stopped muons might be expected due to the addition of such a fin structure. And so a trade-off exists, where a reduction in the equilibrium operating temperature of the target can be achieved if this modest loss of performance is tolerated.

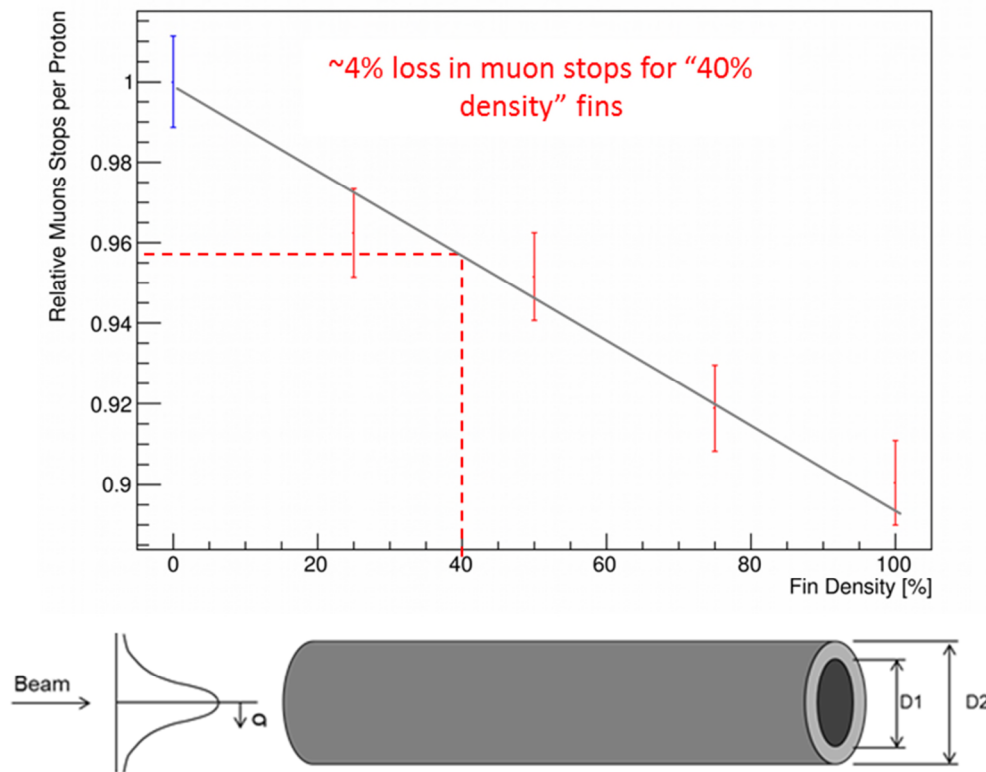


Figure 75, Relative muon stops vs fin density (credit: Kevin Lynch)

### 4.3. Target Geometry

The form and dimensions of the target together with the design of its supporting structure give rise to self-weight and pre-load stresses that may drive creep deformation of the target over time during high temperature operation (see section 3.3 of this report). Certain modifications to the target geometry could be implemented to reduce these stresses in order to mitigate any creep issues that may become apparent.

The self-weight bending stress in a simply supported rod is proportional to its length squared and to the inverse of its diameter (recall Table 6). It follows that the shorter the length and larger the diameter of the target rod, the less prone to self-weight creep it will be. However, potential losses in physics performance must be taken into account when considering such geometric alterations.

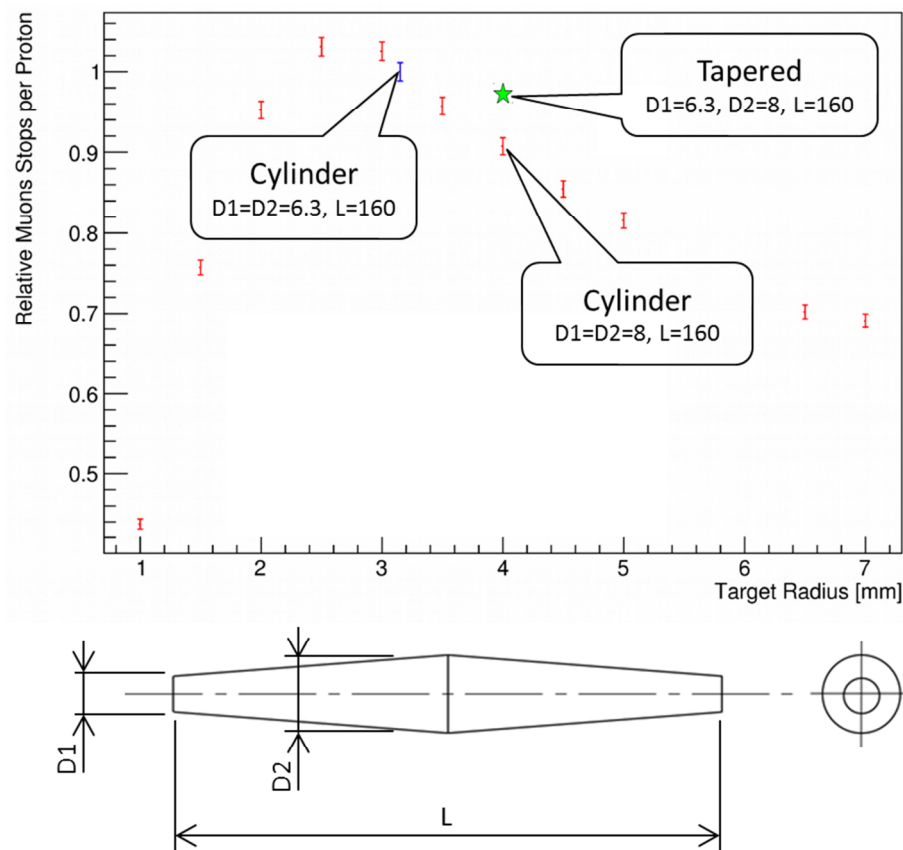
The target diameter could perhaps be increased uniformly along its length. However, given that the peak bending stress occurs at the mid-span it may be more efficient to have a tapered geometry with “standard” 6.3mm diameter ends increasing to a larger diameter at the mid-span (see for example the sketch below Figure 76). Table 12 lists the self-weight bending stress calculated for a number of potential cylindrical and tapered target shapes. It can be seen that the parallel 6.3mm diameter target has a bending stress of 0.77 MPa. This is reduced to 0.58MPa for the tapered option. Interestingly, our creep tests (see for example Figure 54 above) indicate that even a modest reduction in bending stress of this kind may lead to a significant reduction in creep rate.

**Table 12, Self-weight bending stress in a simply-supported tungsten target**

Geometry Type	End diameter “D1” (mm)	Mid-span diameter “D2” (mm)	Length “L” (mm)	Max. Bending Stress (MPa)
Cylinder	6.3	6.3	160	0.77
Cylinder	8.0	8.0	160	0.61
Tapered	6.3	8.0	160	0.58

Figure 76 shows the potential effect of a larger target diameter on physics performance calculated using G4beamline [38]. The blue marker represents the baseline 6.3mm diameter cylindrical target. With respect to this the calculated loss in physics performance for an 8mm diameter cylindrical target is about 10%. However, the calculated loss for a tapered target is much reduced, about 3%.

At a cost of only about 3% loss in physics performance this kind of shape modification could yet be a very effective way of limiting self-weight creep deformations in the event that these become apparent during prototype target heating tests or indeed during in-beam operations.

**Figure 76, Relative muon stops as a function of target radius (credit: Kevin Lynch)**

Another handle on self-weight bending stress is the target length. Figure 77 shows the potential effect of a change in target length on physics performance calculated using G4beamline [39]. The plot indicates that any reduction in target length below the baseline 160mm long rod is expected to result in a loss in physics performance. It is thought that the

self-weight bending stress in the target rod could be reduced by moving the supports inboard to give a lower unsupported length rather than shortening the rod itself. In this way it might be possible to achieve a reduction in bending stress without degrading the physics performance.

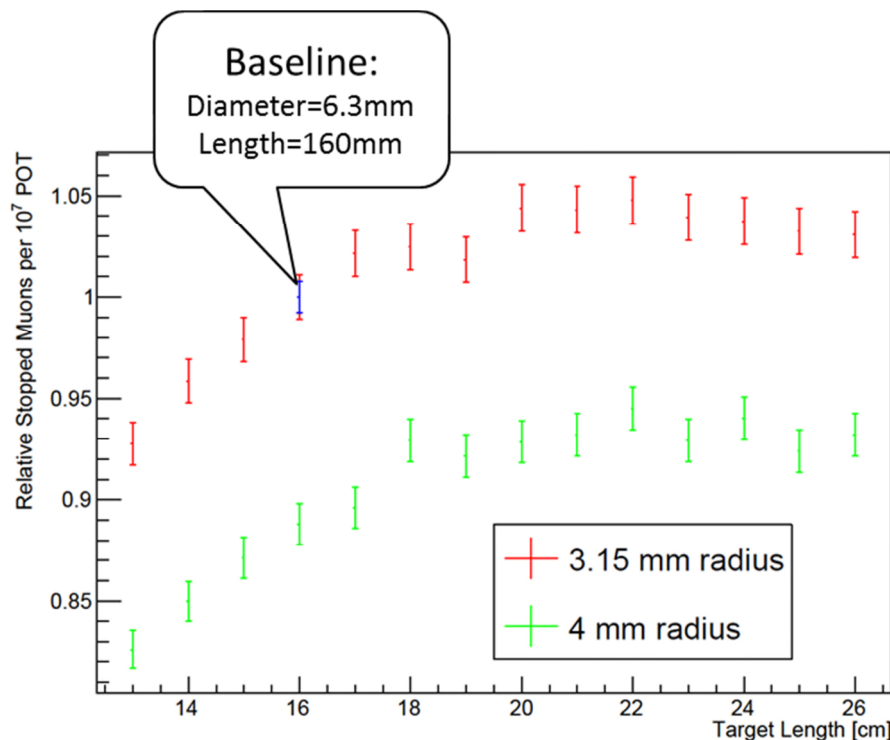


Figure 77, Relative stopped muons as a function of target length (credit: Kevin Lynch)

Due to the geometry of the bicycle wheel support structure a compressive longitudinal load will be applied to the target rod when the support spokes are tensioned. This compressive load, in combination with any self-weight induced bending, may result in accelerated creep/sagging in the target rod. Note that no longitudinal force was applied in the creep tests described in section 3.3 of this report. This effect can be addressed by careful monitoring of the prototype target form and dimensions during prototype target heating tests where a realistic representation of the proposed bicycle wheel structure will be in place. In the event that problems arise this effect could in the first instance be mitigated by reducing the applied spoke tension by reducing the stiffness of the spoke mount springs. That is, some combination of longer and/or thinner blade springs. If this is not sufficient then the support structure could be redesigned to have a spoke angle that is closer to normal to the target rod. This could only be achieved through fairly radical changes in the geometry of the target structure.

#### 4.4. Forced Convection Cooling

Forced convection cooling of the target with either liquid water or helium gas has been considered as an alternative to the baseline radiation cooling scheme. A design for a water cooled target has been described previously [1] [2]. In this section we outline the helium cooled target technology option.

#### ***4.4.1 Helium cooled Mu2e target***

A helium cooled target design has been long considered as an alternative to the current baseline of a radiation cooled tungsten target. While it would clearly require additional helium plant it has the potential to mitigate some of the key risk areas that have been identified by the research and development work on the radiation cooled target such as:

- i) Maintaining the peak surface temperature of the tungsten rod below about 400°C means that oxidation and chemical erosion of tungsten is not an issue.
- ii) High temperature creep associated with exceeding the recrystallization temperature of the tungsten is eliminated.
- iii) Forced convection cooling with helium gas provides a potential upgrade path to higher beam powers that is not feasible with a radiation cooled scheme.
- iv) A helium containment duct is required around the target rod. This vessel provides significant additional structural rigidity to the target rod and can support and contain any fragments in the event of a failure in the pion producing target material.

#### ***4.4.2 Requirements***

Mu2e requires a high atomic number material for the target such as tungsten. The preferred target shape is a small cylinder of diameter 6mm and length 160mm. The target should be suspended within the capture solenoid with as little extra material around the tungsten core as possible. Solid objects near the target will affect the physics performance by absorbing pions. Consequently the design follows the same principle as the current baseline radiation cooled target and the previous water cooled target design, namely a ‘bicycle wheel’ arrangement with hollow spokes for inlet and outlet pipes. The channels to pipe helium in and out of the target should be made of low atomic number materials and be as small as possible. The helium mass flow rate should be high enough such that the tungsten temperature is maintained below the level where oxidation can occur. This is because it may be difficult to guarantee the purity of the helium. Thermo-gravimetric tests in air indicate that the threshold temperature for oxidation is below 500°C. This temperature is also the maximum design value being used by the engineers who are developing the helium cooled tungsten target for the European spallation source. Radiation of the tungsten target with high energy protons will result in some production of hydrogen, tritium and other gases. A purification system may be needed in the helium circuit to control the levels of contaminant gases.

#### ***4.4.3 Feasibility study***

The thermal power deposited in the tungsten target core has been calculated using FLUKA assuming a proton beam kinetic energy of 8GeV, a 1mm beam sigma and a beam power of 8kW. This gave an integrated power deposition in the tungsten of 580W.

A steady state ANSYS CFX model of the tungsten target with an annular helium flow has been setup to predict tungsten operating temperature and helium pressure drop. A helium mass flow of 1gram/s was set as this maintains the bulk helium outlet temperature at 113K above the inlet temperature. Various annular duct widths have been modelled to highlight the effect this design parameter has on tungsten temperature and helium pressure drop. The model treats the helium as a perfect gas with temperature dependant viscosity and conductivity. A shear stress transport turbulence model is used to simulate the turbulence in

the helium channel. The thermal conductivity of the tungsten is also temperature dependant. There is no heat transfer from the two ends of the target in the simulation. As a result of the relatively high thermal conductivity of tungsten and small target radius the steady state simulation shows a fairly small radial variation in temperature. There is a more notable variation in temperature along the length of the target with the peak occurring near the area of where the highest thermal power density is deposited. With a helium annular gap of 1.2mm the peak tungsten temperature is 368°C (Figure 78) and the pressure drop is 0.21bar. As the annular gap is increased for the same 1 gram/s of helium the flow velocity and pressure drop can be reduced but the heat transfer coefficient also reduces resulting in higher temperature tungsten (Figure 79).

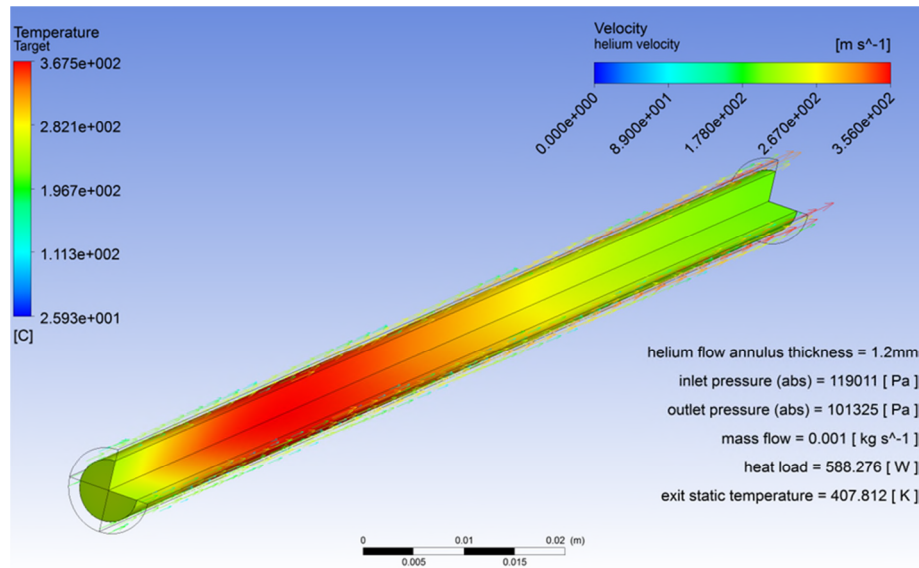


Figure 78, Helium cooled tungsten target – predicted steady state operating temperature

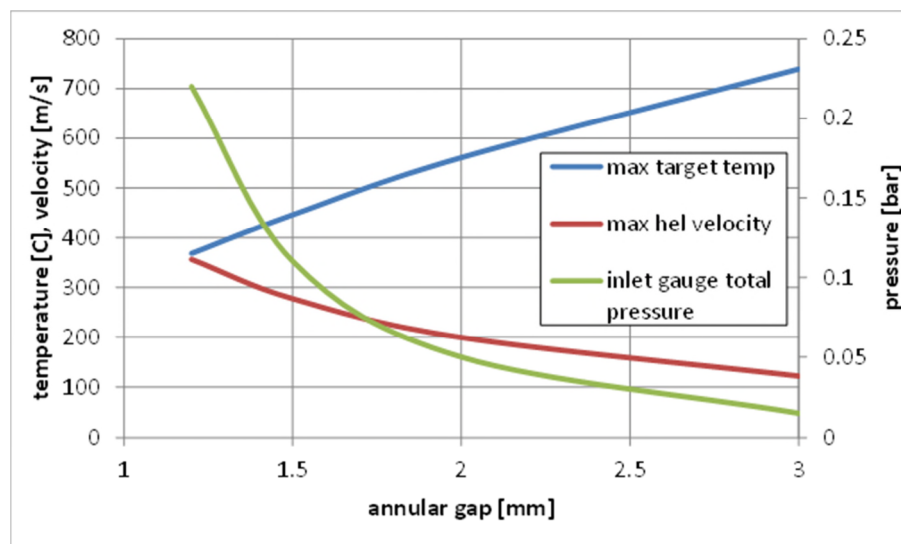


Figure 79, Influence of Helium annular channel gap width on pressure drop and operating temperature

The Reynolds number for the flow in the 1.2mm wide annular duct is 6200 and reduces as the duct size increases. If the duct size was increased too much for a given flow it may have a tendency towards laminar behaviour resulting in a step reduction in heat transfer and marked increase in tungsten temperature. Also considering the requirement to minimise material around the target it would seem sensible to keep towards the 1.2mm annular duct gap. The steady state model allows us to evaluate the effectiveness of the cooling however we know that there will be a fluctuation in temperature around this steady state value due to the pulsed beam. A transient model has been carried out which predicts that the target will take around 20seconds to heat up to its stable operating condition and the pulse to pulse temperature variation will be of the order of 58C (Figure 80). This temperature variation will result in a predicted Von-mises stress fluctuation of between 3.7MPa and 9.6MPa (Figure 81). The highest stress occurring just after a beam pulse and then dropping to a minimum after the cooling period. This level of cyclic stress is not a major concern in tungsten. It is also worth noting that with the helium cooling some parts of the tungsten may operate below the ductile transition temperature and so may remain brittle during operation.

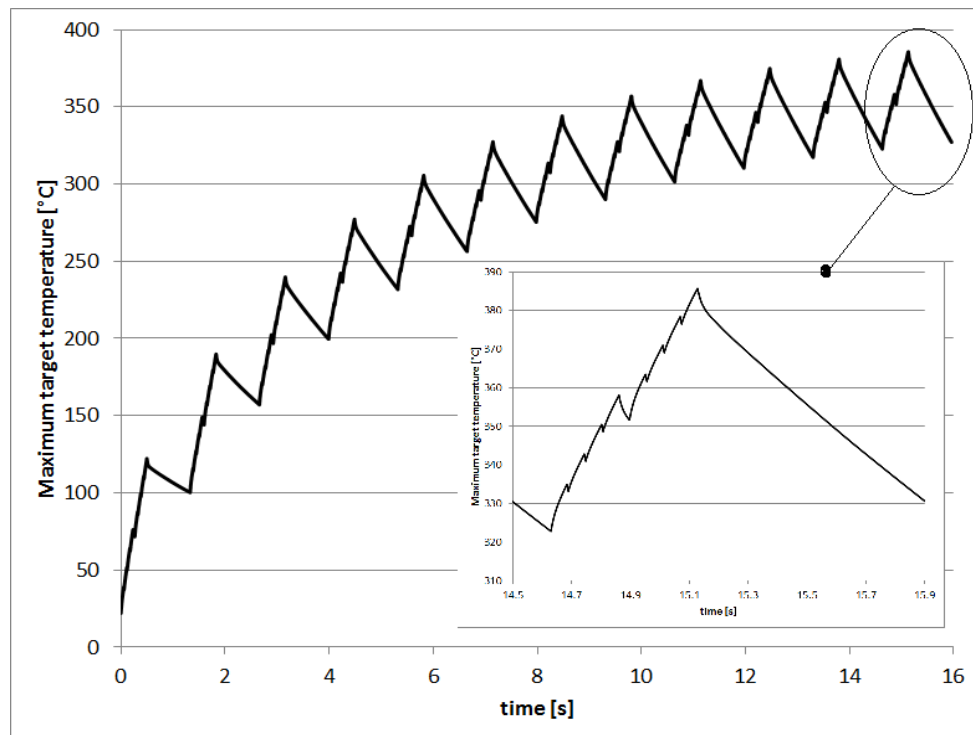


Figure 80, Result of transient simulation of the helium cooled target

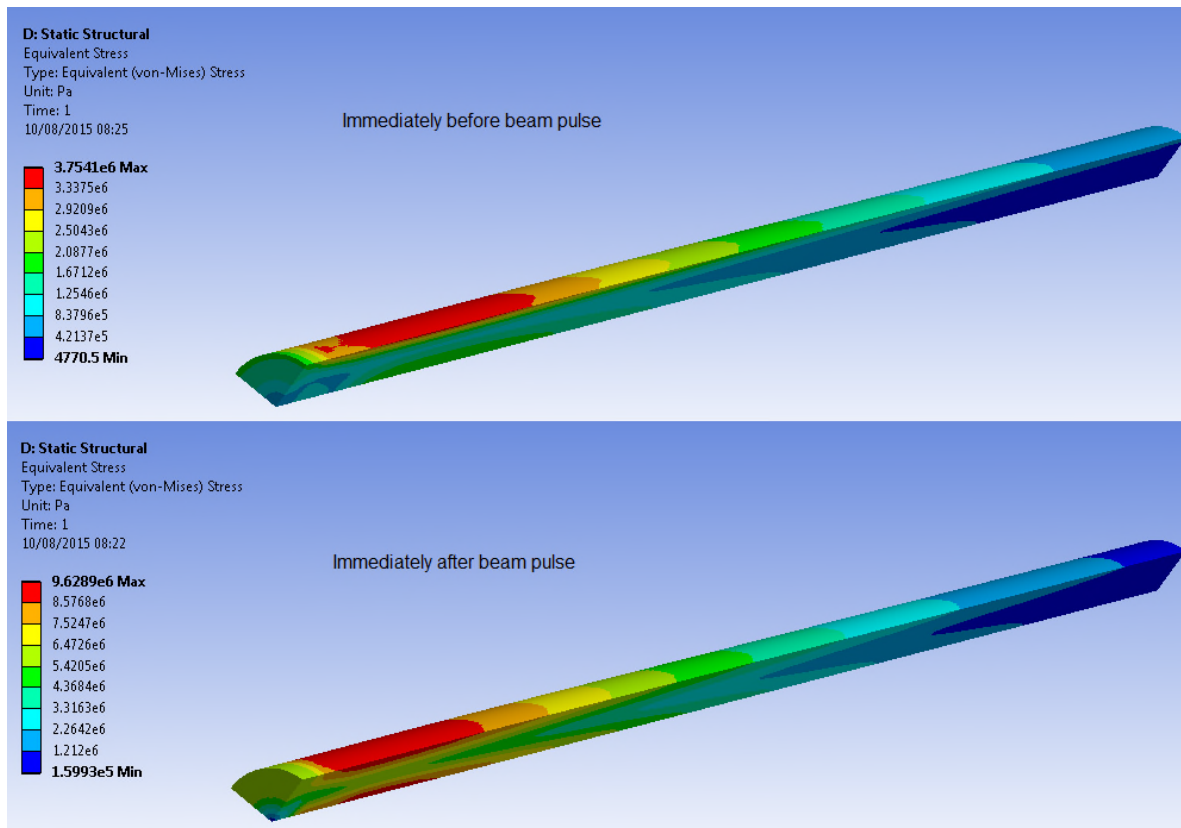


Figure 81, Von-Mises stress before and after a beam pulse

#### 4.4.4 Helium cooling circuit

So far we have just considered the feasibility of the target itself, it will clearly require a system to circulate and cool the helium so as to deliver fresh cold helium to the target. The basic components of such a circuit are shown in Figure 82.

The circuit will require a helium compressor or circulator to drive the gas through the circuit. Ideally the compressor would have a dry mechanism so that there is no chance of mechanism oil contaminating the helium. The compressor will need to be hermetically sealed so that the coolant gas cannot escape from the circuit through rotating shaft seals. Off the shelf dry mechanism compressors are all designed to operate with air, although they will work with helium performance is often not published and tends to be significantly lower due to their mechanisms relying on dynamic shaft seals and helium being much harder to seal than air. An oversized scroll compressor built in to a hermetically sealed container is probably the most economical approach. Two compressors would be desirable with one on standby so that operation could continue in the event of a compressor failure or scheduled maintenance being required. We have identified the P25 scroll compressor made by AirSquared (Figure 83) as an ideal pump for 8kW beam operation. It has a dry mechanism, is hermetically sealed and can provide the predicted flow requirements of the target (Figure 84).

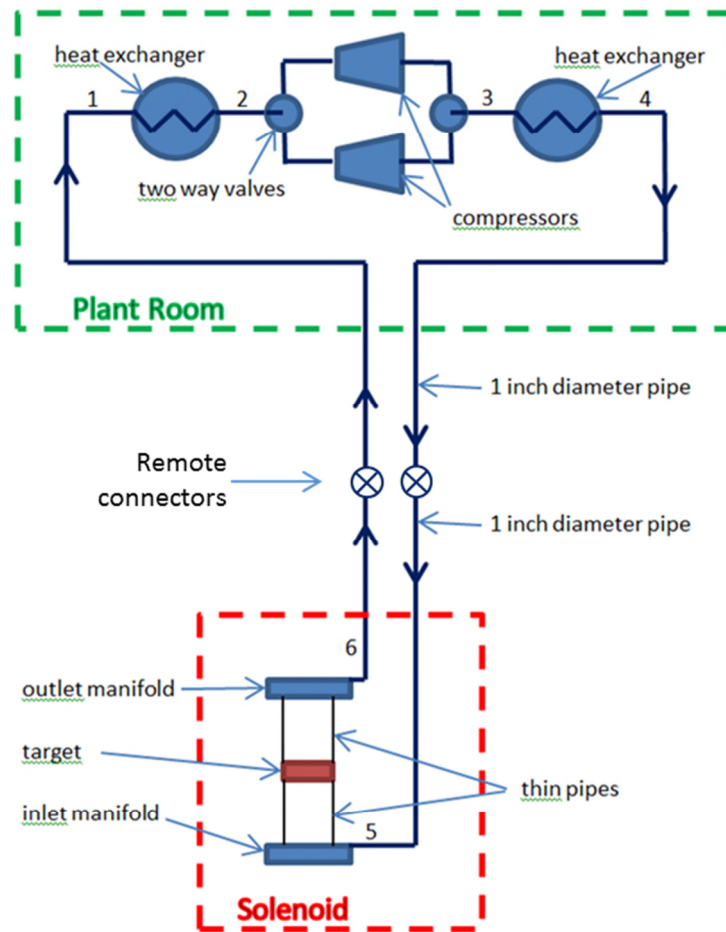


Figure 82, Principal elements of a helium cooling circuit (see figure 4 for more details on purification system)

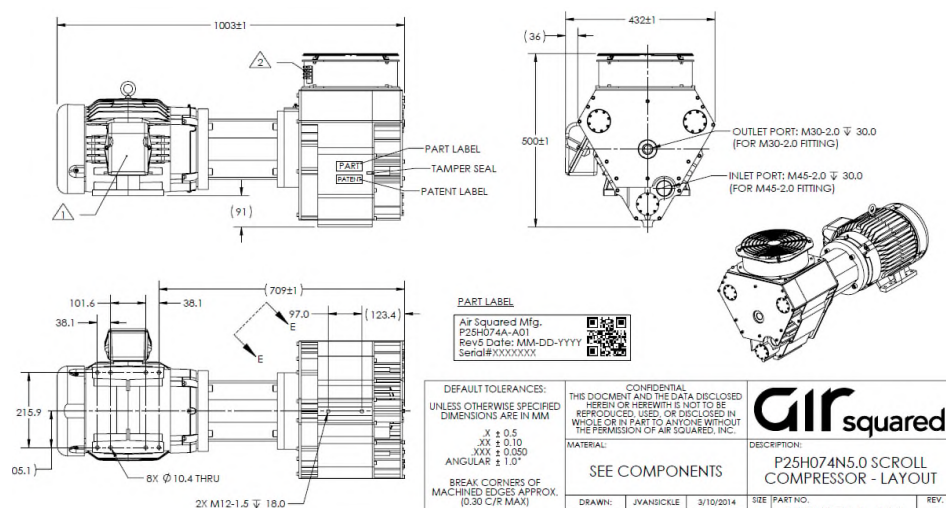
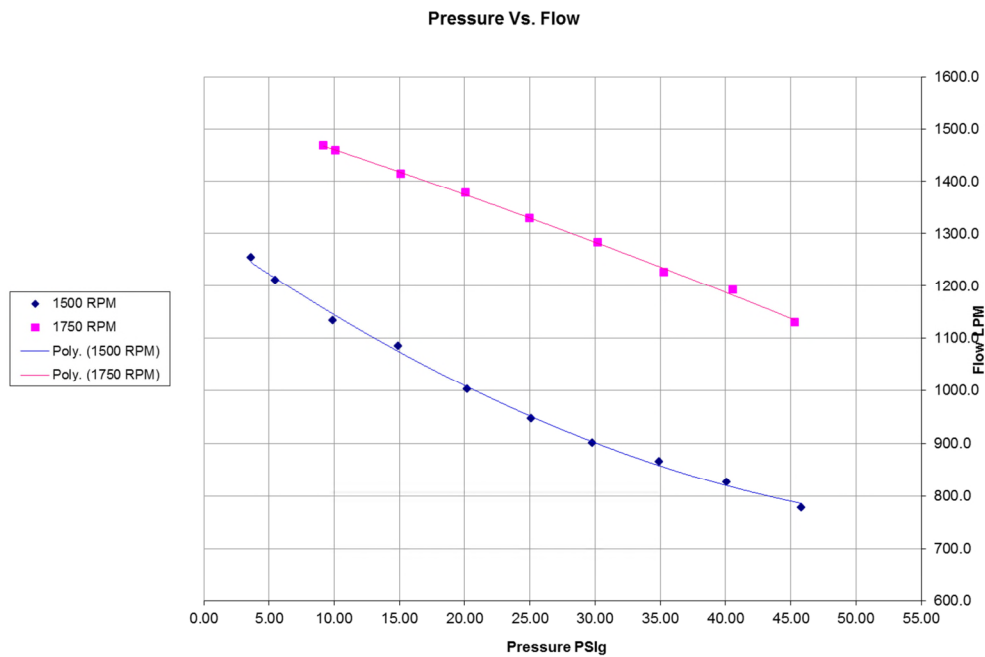


Figure 83, Air squared scroll compressor



**Figure 84, Performance of Airsquared scroll pump.**

The heat load on the circuit from the target is less than 1kW (i.e. less than a domestic electric element heater). As such the heat could be removed via natural convection to the target station air via a finned heat exchanger (Figure 85). Connecting pipes between the plant room and the solenoid should be large enough to minimise pressure requirements of the compressor. For the 8kW beam the 1gram/s of helium that is required flowing down 25mm diameter pipe results in a pressure drop of 0.0001bar/m or 0.01 bar for 100m of pipe (Figure 86).



**Figure 85, finned heat exchanger**

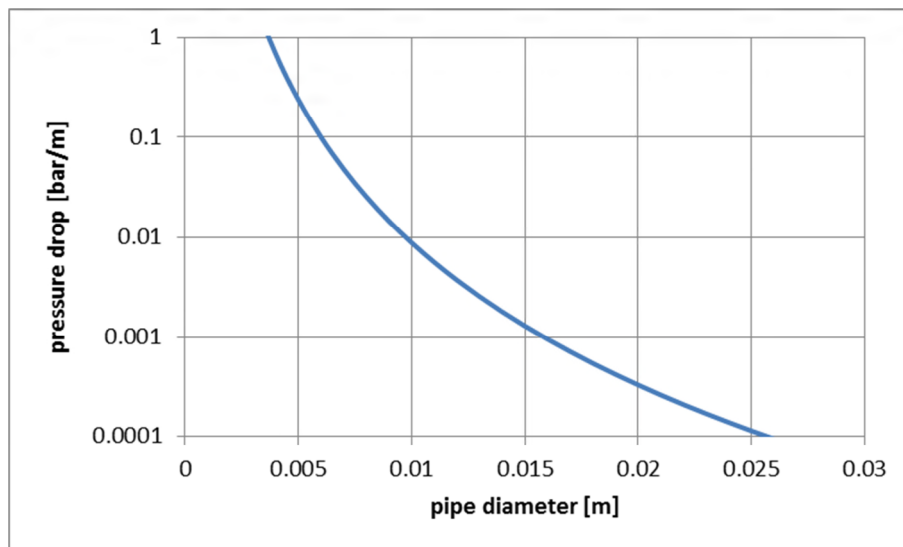


Figure 86, pressure drop for 1gram/s of helium flow at standard conditions

Fluka was employed to predict the quantity of residual nuclei produced by the beam interacting with tungsten. Figure 87 shows all of the nuclei produced. Hydrogen production is of concern for radiation damage reasons but also because of its flammability. For the 8kW beam a hydrogen nuclei production rate of  $2 \times 10^{13}$  hydrogen nuclei/s is predicted. Table 13 shows which isotopes of hydrogen are produced including the amount of tritium. In engineering units the total hydrogen generation is 11cc of hydrogen gas at standard atmospheric conditions, which has a calorific value of 140J. It is thought that this could be dealt with by occasional helium replacement during long service intervals? If however this was not deemed a sufficient mitigation method then purification of the helium may be necessary to avoid a build-up of unwanted elements in the closed circuit. Hydrogen (Tritium), carbon monoxide, carbon dioxide, water, oxygen, nitrogen, methane (hydrocarbons) & noble gases may all be produced.

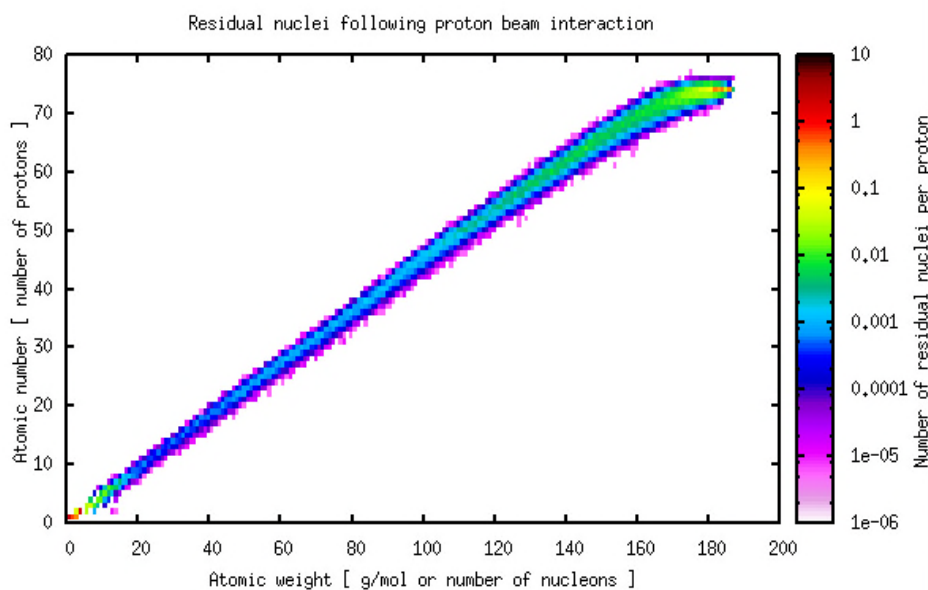


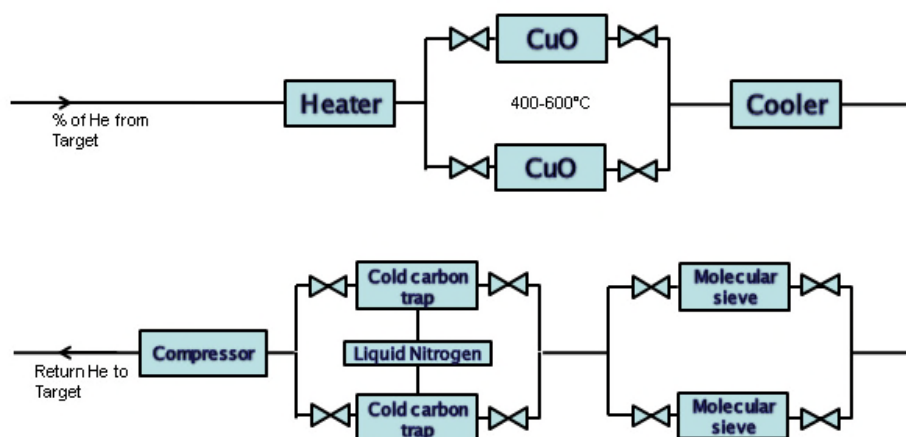
Figure 87, residual nuclei created in tungsten

**Table 13, hydrogen production in tungsten target**

Hydrogen isotope	Protium (1 proton )	Deuterium (1 proton & 1 neutron)	Tritium (1 proton & 2 neutrons)
Residual nuclei per incident proton	2.17	0.60	0.37

The European Spallation Source baseline target design is a helium cooled tungsten target (note ESS has a 5MW beam with a 3kg/s helium flow where as Mu2e has an 8kW beam and would only need a 1g/s helium flow) and the engineers of the helium loop plan to employ a helium purification system that can remove all of the above mentioned components. The typical purification process can be simply split into two parts oxidation and absorption. Oxidation is achieved using a catalyst, if the helium temperature is below 400°C at entry to the catalyst which is likely to be the case for the mu2e target design then a heater will be required to ensure the catalyst activation temperature is reached. A Copper oxide bed will oxidise hydrogen, carbon monoxide and hydrocarbons to give water and carbon dioxide at an operating temperatures between 400°C and 600°C. Water and carbon dioxide can be removed by a molecular sieve trap while nitrogen, oxygen, methane and noble gases can be removed by a liquid nitrogen cooled carbon cold trap. A cooler is required after the copper oxide bed to bring the temperature back to a level that can be tolerated by the molecular sieve. Tritium which will oxidise in the same way as hydrogen will become tritiated water and can then be absorbed in the molecular sieves. It is desirable to keep the tritium concentration in the circuit down in case there is a helium leak in to the atmosphere. Figure 88 shows a schematic of the purification system that may be necessary.

A control system will be required to maintain the correct helium flow through the target and the amount of helium going through the purification loop.

**Figure 88, Purification system proposed for helium cooled nuclear reactors and European Spallation Source**

#### 4.4.5 Upgrade potential

There is potential for upgrading a helium cooled target to a higher power than the current 8kW baseline. However there are certain challenges that would have to be assessed to determine how far the current type of design could go. In order to highlight some of these challenges we now consider a 100kW beam incident on the same cylindrical tungsten target. The model input parameters were now a proton beam kinetic energy of 8GeV, a beam sigma of 1mm and an average beam power of 100kW. This results in an integrated power deposition in the tungsten of 7.4kW.

It was found that by increasing the annular duct width to 2.2mm, the operating pressure to 14bar and the helium mass flow to 48g/s the peak target temperature in the steady state model could be kept below 600°C (Figure 89).

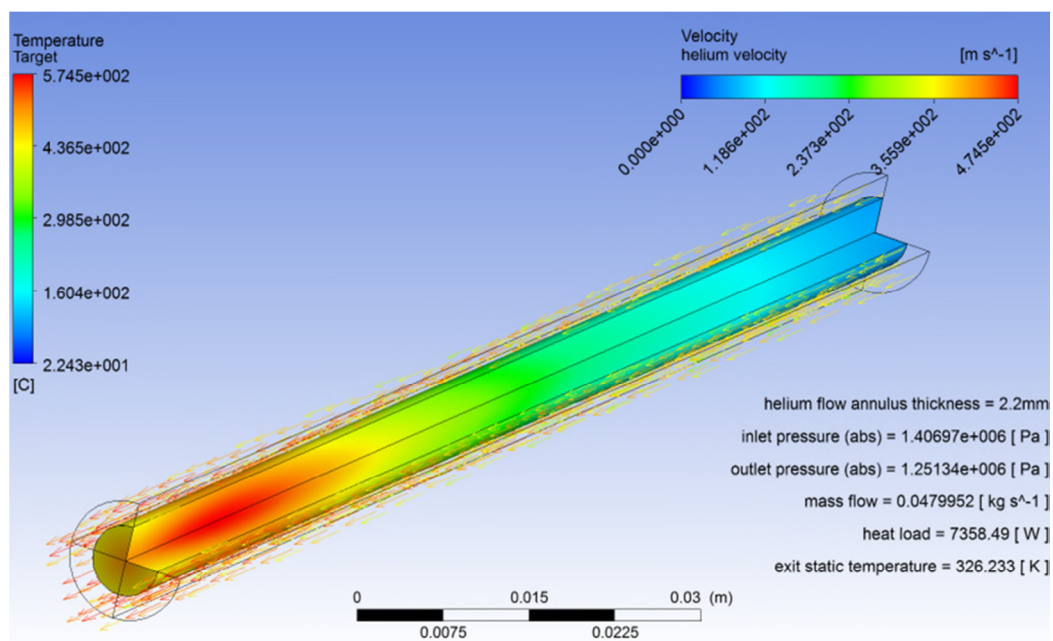


**Figure 89, steady state thermal performance with 100kW beam**

None of these parameters seem to be show stoppers however if the current beam time structure was maintained then the transient temperature would become a concern reaching a peak around 1000°C (Figure 90).

A large cyclic stress results from the temperature fluctuation and is up to the order of 200MPa as a result of more significant radial temperature gradients (Figure 91). This level of stress may be lower than the yield stress of some forms of tungsten but with the cyclic nature of the stress this magnitude would be a concern. The proton flux on target at 100kW would be around  $1.6 \times 10^{15}$  protons/cm<sup>2</sup>/s. This is more than ten times higher than what the ISIS target 1 experiences and 7.5 times higher than what target 2 experiences. Considering the higher beam energy too (Mu2e 8GeV, ISIS 800MeV), the level of radiation damage would be significantly higher than is experienced by the tungsten in ISIS.

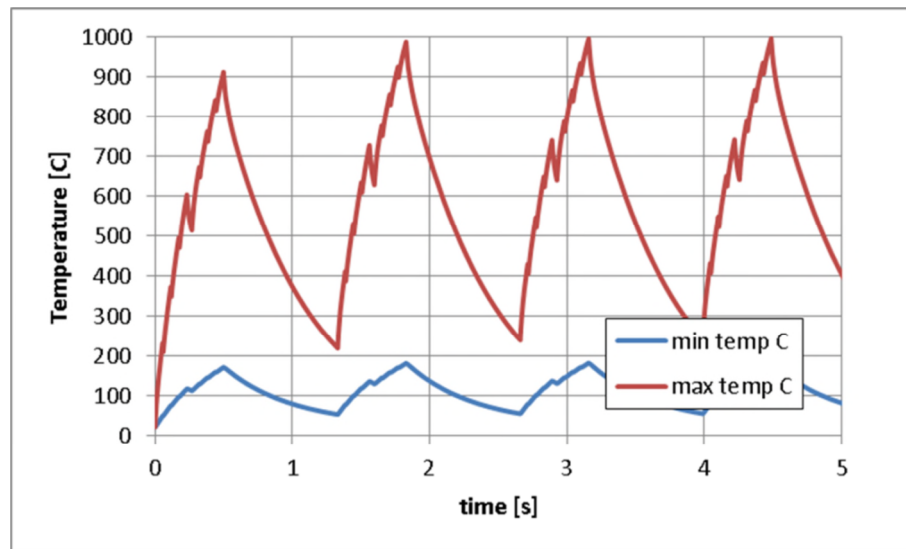


Figure 90, transient target temperature profile for 100kW helium cooled mu2e

A helium cooled target could facilitate the removal of the time averaged heat load from a 100kW beam. However to avoid significant cyclic stress amplitudes the beam structure would have to be changed to a closer approximation of a CW beam. Radiation damage would also be of concern.

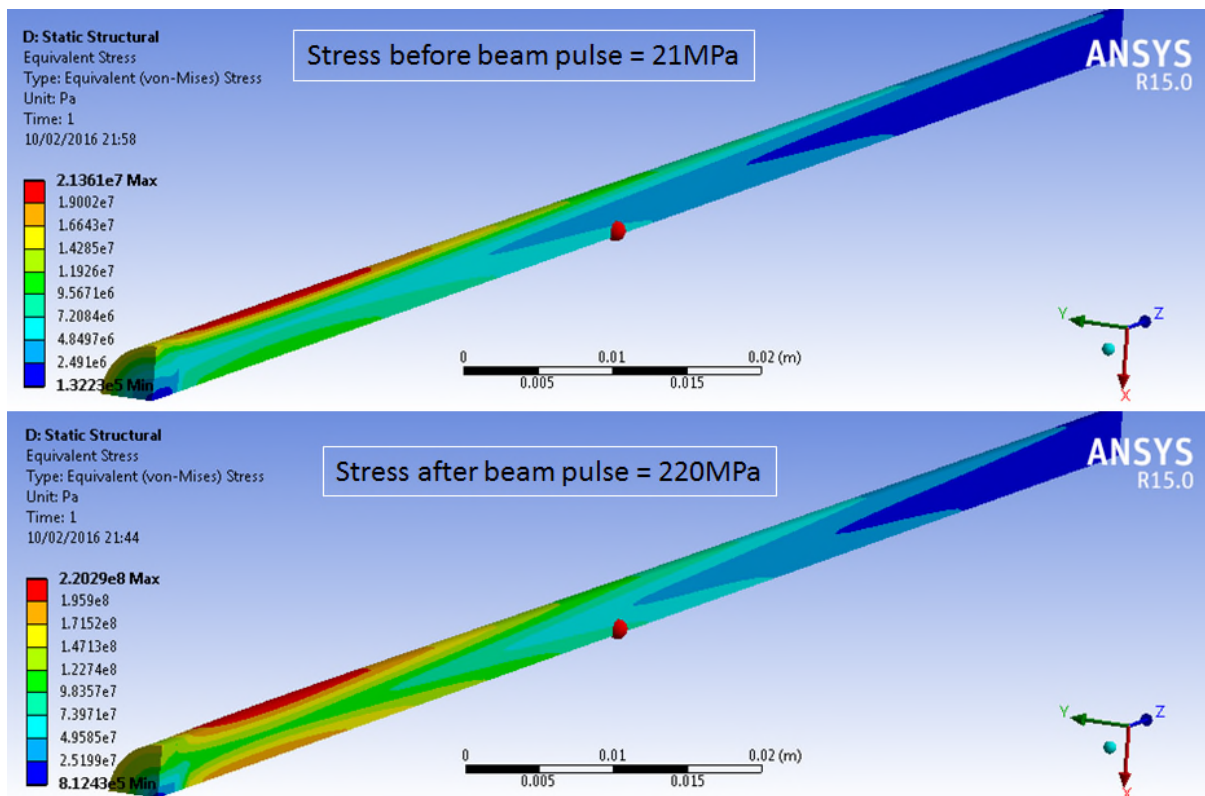


Figure 91, stress fluctuation for 100kW beam with same time structure

#### 4.4.6 Cost estimate for developing a helium cooled target for an 8kW beam

Table 14 contains a list of the components required for a helium cooled target for an 8kW beam along with an estimation of their size and cost and also an estimation of the effort that would be required to deliver the target.

**Table 14, Estimated cost of Helium cooled target including helium loop and required effort**

ITEM	DESCRIPTION	NOMINAL SIZE	ESTIMATED COST IN DOLLARS
1	Helium cooled tungsten target with outer can to form helium cooling annular channel	1cm diameter x 18cm long	35k
2	Thin helium lines to deliver helium into the capture solenoid		0.75k
3	Large diameter helium lines to transport helium from target to helium plant area with minimum pressure drop	1inch diameter x 10s of meters long	2k
4	Helium to Air heat exchanger, heat to be dissipated to hall air by convection from a finned radiator	0.125m <sup>3</sup>	10k
5	Helium compressor and buffer tank if necessary	0.125m <sup>3</sup>	75k for two off the shelf machines modified for helium use 350k for two purpose-built machines
6	Control Valve and control system		25k
7	Purification system including CuO catalyst and molecular sieve, liquid nitrogen cold trap, heater, cooler, titanium bed for tritium conversion		200k
8	Vacuum pump and tank to provide helium circuit fill and emptying capability		10k
9	Design and Development Effort		2 man years 300k
10	Integration, manufacturing and installation effort		2 man years 300k
<b>TOTAL</b>			<b>\$1232.75k</b>

#### 4.5. Beam Power

The target design calculations performed to date have been based on the beam parameters listed in Table 15 [10]. FLUKA simulations indicate that for a beam power of 7.7 kW, 580W is deposited as heat in the target [5]. The expected distribution of that heating in the case of a well-centred beam is shown in Figure 92. The peak energy density is on the target centre-line, towards the upstream end with respect to the incoming proton beam. The equilibrium temperature in the case of a bare tungsten target is shown in Figure 93. The expected peak temperature in the target rod is about 1700°C [5]. This is well above the recrystallisation temperature for tungsten which is around 1200°C - 1300°C [40] and as such a limited component life should be expected.

**Table 15, Mu2e Beam Parameters**

Beam kinetic energy	8 GeV
Beam spot shape	Gaussian
Beam spot size	$\sigma_x = \sigma_y = 1 \text{ mm}$
Main Injector cycle time	1.333 sec
Number of spills per MI cycle	8
Duration of Spill	54 msec
Number of protons per spill	1 Tp
Duty Factor	32 %
Average Beam Power	7.7 kW
Average Beam Current	1 $\mu\text{A}$

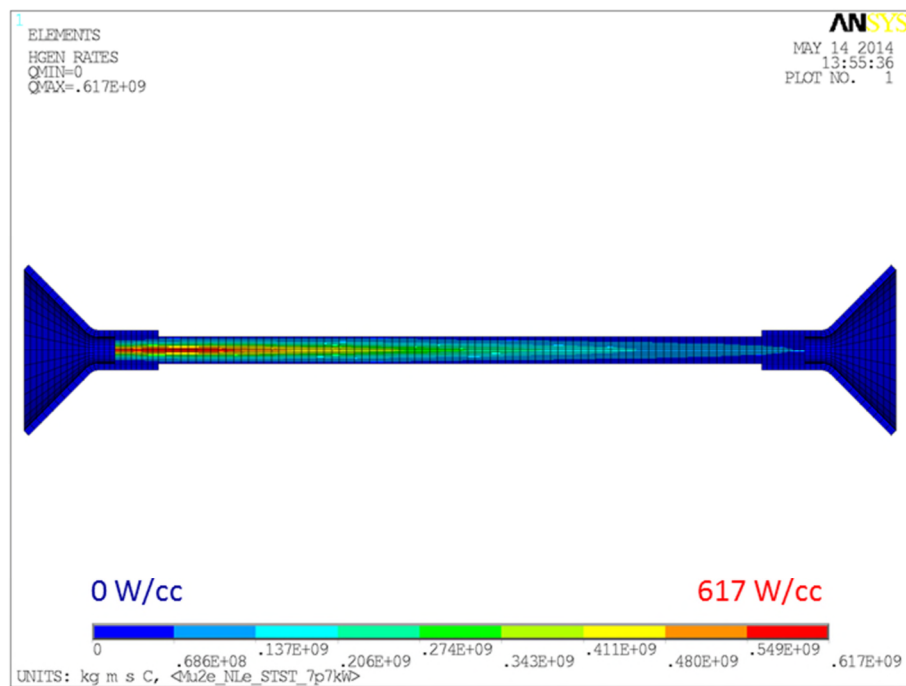


**Figure 92, Beam heating distribution in the target (FLUKA). For a beam power of 7.7 kW, 580W is deposited as heat in the target.**

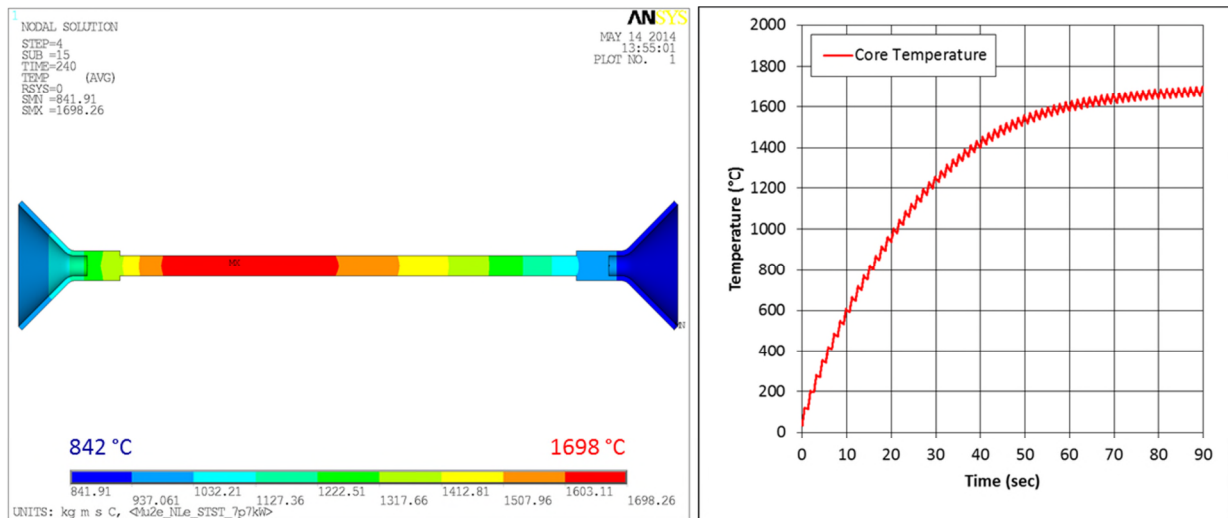


Figure 93, Equilibrium temperature distribution assuming 580W and  $\epsilon(T)$  from the literature (left), and the calculated temperature rise in the target following beam-on (right)

The calculated maximum equilibrium target temperature as a function of the average beam power is shown in Figure 94, where the solid line represents a bare tungsten target, and the dashed line represents a target with a high emissivity coating (such as silicon carbide SiC). Many of the target failure mechanisms discussed in section 3 of this report can be mitigated through a reduction in operating temperature. In the event that the expected target life is not achieved during initial operation a reduction in beam power may be an appropriate interim measure while longer term solutions are sought. It is thought that the nominal ~8kW beam power is somewhere close to the limit for a feasible radiation cooled target. For any beam power upgrade forced convective cooling schemes should be considered as discussed in section 4.4 of this report.

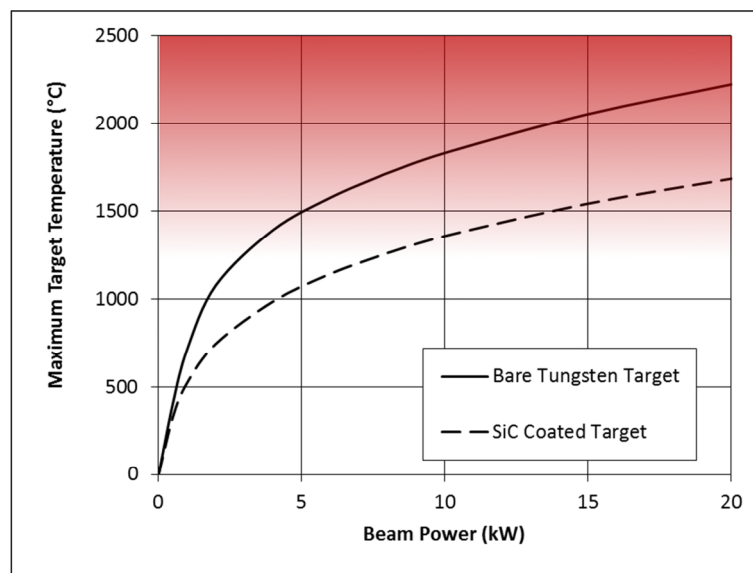


Figure 94, Target equilibrium temperature as a function of beam power

## 5 References

- [1] CJ Densham et. al., “Conceptual Design Study of Mu2e Experiment Pion Production Target Components and Systems, First Intermediate Design Study Report,” Mu2e doc-db #1477, 13 April 2011.
- [2] CJ Densham et. al., “Conceptual Design Study of Mu2e Experiment Pion Production Target Components and Systems, Second Intermediate Design Study Report,” Mu2e doc-db #1746, 4th July 2011.
- [3] CJ Densham et. al., “Design Study Report on a Radiation Cooled Target,” Mu2e doc-db#2406, 24 August 2012.
- [4] CJ Densham et. al., “Design, Testing and Prototyping work relating to Mu2e Experiment Pion Production Target, Interim Status Report,” Mu2e doc-db #3508, 02 September 2013.
- [5] CJ Densham et. al., “Design Testing and Prototyping work relating to the Mu2e Experiment Pion Production Target,” Mu2e doc-db #4305, 25 June 2014.
- [6] CJ Densham et. al., “Mu2e Production Target Development Towards CD-3, Interim Report,” Mu2e doc-db #5937, 10 August 2015.
- [7] JRJ Bennett, GP Skoro et. al., “Lifetime and strength tests of tantalum and tungsten under thermal shock for a Neutrino Factory target,” *Nuclear Instruments and Methods in Physics Research A*, vol. 646, no. 1, pp. 1-6, August 2011.
- [8] K Lynch and J Popp, “Target Support Rod Variations,” Mu2e doc-db #8259, November 11, 2016.
- [9] J Anderson, Jr. (Chair), “Presentations at the Mu2e Target, remote handling, and heat & radiation shield review,” Fermilab, November 16-18, 2015.
- [10] RE Ray et. al., “Mu2e Technical Design Report,” Mu2e doc-db #4299, October 2014.
- [11] Goodfellow Cambridge Limited, Ermine Business Park, Huntingdon, England, PE29 6WR, Email: info@goodfellow.com, Telephone: +44 (0)1480 424800, web:

www.goodfellow.com.

- [12] Plansee High Performance Materials, 3 Lidstone Court, George Green, Slough, SL3 6AG, UK. Tel: +44 (0)1753 576959, email: uk@plansee.com, web: www.plansee.com.
- [13] M Rieth and B Dafferner, "Limitations of W and W-1%La<sub>2</sub>O<sub>3</sub> for use as structural materials," *Journal of Nuclear Materials*, vol. 342, pp. 20-25, 2005.
- [14] M Rieth et. al., "Tungsten as a Structural Divertor Material," *Advances in Science and Technology*, vol. 73 CIMTECH2010 5th Forum on New Materials, pp. 11-21, 2010.
- [15] J Safarian and TA Engh, "Vacuum Evaporation of Pure Metals," *Metallurgical and Materials Transactions A*, vol. 44A, pp. 747-753, 2013.
- [16] R Szwarc, ER Plante, JJ Diamond, "Vapor Pressure and Heat of Sublimation of Tungsten," *Journal of Research of the National Bureau of Standards - Physics and Chemistry*, vol. 69A, no. 5, pp. 417-421, 1965.
- [17] IL Shabalin, *Ultra-High Temperature Materials*, Vol 1, Springer, 2014.
- [18] AS Darling, "The Vapour Pressures of the Platinum Metals," *Platinum Metals Review*, vol. 8, no. 4, pp. 134-140, 1964.
- [19] "Radiate Collaboration Homepage," [Online]. Available: [www.radiate.fnal.gov](http://www.radiate.fnal.gov).
- [20] RB Jones, G Hall, B Marsden and CA English, "Literature Review on the Irradiation Response of Be, W and Graphite for Proton Accelerator Applications," NNL (13) 12703, November 2013.
- [21] JC He, GY Tang, A Hasegawa and K Abe, "Microstructural development and irradiation hardening of W and W-(3-26) wt%Re alloys after high-temperature neutron irradiation to 0.15 dpa," *Nuclear Fusion*, vol. 46, pp. 877-883, November 2006.
- [22] H Ullmaier and F Carsughi, "Radiation damage problems in high power spallation neutron sources," *Nuclear Instruments and Methods in Physics Research B*, vol. 101, pp. 406-421, 1995.
- [23] DJS Findlay, "High Power Operational Experience at ISIS," in *proceedings of HB2010*,

Morschach, 2010.

- [24] DJS Findlay, “ISIS - Pulsed Neutron and Muon Source,” in *proceedings of PAC07*, Albuquerque, 2007.
- [25] KJ Loenard, “Radiation Effects in Refractory Metals and Alloys,” in *Comprehensive Nuclear Materials*, Elsevier Ltd, 2012, pp. 181-213.
- [26] “ITER Materials Assessment Report,” 2001.
- [27] AT Peacock et.al., “Overview of recent European materials R&D activities related to ITER,” *Journal of Nuclear Materials*, Vols. 329-333, Part A, pp. 173-177, 2004.
- [28] F Hofmann et. al., “Non-Contact Measurement of Thermal Diffusivity in Ion-Implanted Nuclear Materials,” *Scientific Reports*, vol. 5, Article number: 16042, 2015.
- [29] H Kurishita et. al., “Development of ultra-fine grained W-(0.25–0.8)wt%TiC and its superior resistance to neutron and 3 MeV He-ion irradiations,” *Journal of Nuclear Materials*, vol. 377, no. 1, pp. 24-40, 2008.
- [30] H Kuridhita and S Makimura, *Status and prospect of ductile, radiation-resistant tungsten (W) materials*, presentation at the international workshop on future potential of high intensity accelerators for particle and nuclear physics (HINT2016), Tokai, 2016.
- [31] P Krautwasser, H Derz and E Kny, “Influence of fast neutron fluence on the ductile–brittle transition temperature of tungsten, W–10Re, and W–3.4Ni–1.6Fe,” *High Temperatures High Pressures*, vol. 22, no. 1, pp. 25-32, 1990.
- [32] RV Hesketh, “Collapse of vacancy cascades to dislocation loops,” in *Proceedings of the International Conference on Solid State Physics and Research with Accelerators*, BNL-500883 (C-52) (Physics-TID-4500), Brookhaven National Laboratory, September 1967.
- [33] E Snoeks, KS Boutros and J Barone, “Stress relaxation in tungsten films by ion irradiation,” *Applied Physics Letters*, vol. 71, no. 2, pp. 267-269, 1997.
- [34] SA Maloy et. al., “Water corrosion measurements on tungsten irradiated with high energy protons and spallation neutrons,” *Journal of Nuclear Materials*, vol. 431, pp. 140-146, 2012.

- [35] Yih and Wang, Tungsten: Sources, Metallurgy, Properties, and Applications, New York: Plenum Press, 2nd Edition, 1981.
- [36] A Sala, Radiant Properties of Materials, New York: Elsevier, 1985.
- [37] K Lynch, “Stopped muon yield for a simplified target fin model,” Mu2e doc-db #7403, 10 May, 2016.
- [38] K Lynch, “Some beam and target shape explorations,” Mu2e doc-db #7946, 24 August, 2016.
- [39] K Lynch and J Popp, “Radiation cooled tungsten production target: Stopped muon yield vs target length,” Mu2e doc-db #3752, 15 January 2014.
- [40] TE Teitz and JW Wilson, “Behaviour and Properties of Refractory Metals,” Edward Arnold (Publishers) Ltd., London, 1965.